

UNIVERSITY OF RIJEKA

FACULTY OF PHYSICS

Daria Jardas Babić

**TOWARDS EFFICIENT  
PHOTODEGRADATION OF  
MICROPLASTICS: APPLICATION OF  
ZINC OXIDE THIN FILMS DEPOSITED  
WITH PLASMA-ENHANCED ATOMIC  
LAYER DEPOSITION**

DOCTORAL DISSERTATION

Rijeka, 2025



UNIVERSITY OF RIJEKA

FACULTY OF PHYSICS

Daria Jardas Babić

**TOWARDS EFFICIENT  
PHOTODEGRADATION OF  
MICROPLASTICS: APPLICATION OF ZINC  
OXIDE THIN FILMS DEPOSITED WITH  
PLASMA-ENHANCED ATOMIC LAYER  
DEPOSITION**

DOCTORAL DISSERTATION

Supervisors:

Assoc. Prof. Robert Peter

Assoc. Prof. Aleš Omerzu

Rijeka, 2025



Mentor doktorskoga rada: izv. prof. dr. sc. Robert Peter

Komentor doktorskoga rada: izv. prof. dr. sc. Aleš Omerzu

Doktorski rad obranjen je dana \_\_\_\_\_ u/na \_\_\_\_\_ , pred  
povjerenstvom u sastavu:

1. \_\_\_\_\_

2. \_\_\_\_\_

3. \_\_\_\_\_

4. \_\_\_\_\_

5. \_\_\_\_\_







# Abstract

This thesis presents a systematic study of zinc oxide (ZnO) thin films synthesised by plasma-enhanced atomic layer deposition (PEALD). The focus is on their structural, optical and photocatalytic properties as a function of the deposition conditions and their potential application in the degradation of microplastics. A comprehensive set of characterisation experimental techniques was used to analyse the films: grazing incidence X-ray diffraction (GIXRD), scanning and transmission electron microscopy (SEM, TEM), X-ray photoelectron spectroscopy (XPS), UV-Vis spectroscopy, secondary ion mass spectroscopy (SIMS) and photoluminescence spectroscopy (PL).

Firstly, the influence of deposition temperature was investigated and it was found that films grown at lower temperatures, particularly at 60 °C, exhibited higher photocatalytic activity. This improvement was attributed to a polycrystalline microstructure consisting of nanometre-sized grains ( $\sim 5$  nm) with a high surface-to-volume ratio and a dense network of grain boundaries. These features promote the trapping of charge carriers at the surface and suppress recombination, thereby increasing the availability of active species for photocatalytic reactions.

To enable deposition on thermally sensitive substrates, PEALD was also performed at room temperature with different radio frequency (RF) plasma powers. A strong dependence on the plasma power was observed. Films deposited with powers below 200 W are amorphous and showed a weak photocatalytic response, while those deposited at or above 200 W formed nanocrystalline structures with significantly improved photocatalytic activity. This shows that both the deposition temperature and the plasma power are crucial parameters for tuning the photoactive properties of ZnO films.

Based on these findings, ZnO thin films were applied to poly(ethylene terephthalate) (PET) microfibres for its photocatalytic degradation. Two sets of parameters (80 °C with 50 W and room temperature at 250 W) were found to be particularly effective in yielding thin ZnO films which initiate polymer degradation. A range of experimental conditions were investigated, including different water media (ultrapure water, tap water, water solutions), film thicknesses,

light sources (UV and sun-simulated) and illumination durations. The best photocatalytic degradation was achieved in tap water and simulated seawater under 48 hours of UV exposure.

Overall, this work demonstrates how fine-tuning of PEALD parameters can lead to ZnO thin films with tailored photocatalytic performance and opens new directions for their use in addressing critical challenges in microplastic pollution and water treatment technologies.





## Sažetak

U ovom radu predstavljeno je sustavno istraživanje tankih filmova cinkovog oksida (ZnO) dobivenih metodom plazmom potpomognute depozicije atomskih slojeva (PEALD). Poseban naglasak stavljen je na ispitivanje njihovih strukturnih, optičkih i fotokatalitičkih svojstava u ovisnosti o uvjetima depozicije, s ciljem njihove primjene u razgradnji mikroplastike. Za karakterizaciju filmova korištene su sljedeće eksperimentalne tehnike: rendgenska difrakcijska analiza pri okružujućem upadnom kutu (GIXRD), pretražna i transmisijska elektronska mikroskopija (SEM, TEM), spektroskopija fotoelektrona rendgenskim zrakama (XPS), UV-Vis spektroskopija, masena spektrometrija sekundarnih iona (SIMS) i fotoluminiscentna spektroskopija (PL).

U prvom dijelu istraživanja analiziran je utjecaj temperature tijekom procesa depozicije. Utvrđeno je da filmovi dobiveni pri nižim temperaturama, osobito na 60 °C, pokazuju veću fotokatalitičku aktivnost. Taj se učinak pripisuje njihovoj polikristaliničnoj mikrostrukтури, sastavljenoj od nanometarskih zrna (~ 5 nm), koja imaju velik omjer površine i volumena te gustu mrežu granica među zrnima. Ovakva struktura pogoduje zarobljavanju nositelja naboja na površini i smanjuje njihovu rekombinaciju, čime se povećava učinkovitost fotokatalitičkih reakcija.

Kako bi se omogućila primjena ZnO filmova na termalno osjetljivim podlogama, tanki ZnO filmovi su narastani i na sobnoj temperaturi uz primjenu različitih snaga plazme. Pokazalo se da snaga plazme značajno utječe na svojstva filmova. Filmovi sintetizirani sa snagama ispod 200 W su amorfni i pokazuju slabu fotokatalitičku aktivnost, dok su oni narastani sa snagama od 200 W i više razvili nanokristaliničnu strukturu uz znatno bolju fotokatalitičku učinkovitost. Ovi rezultati pokazuju da su temperatura i snaga plazme ključni parametri za dobivanje funkcionalnih svojstava tankih filmova cinkova oksida.

Na temelju dobivenih rezultata, tanki ZnO filmovi nanoseni su na mikrovlakana poli(etilentereftalata) (PET) radi ispitivanja njihove učinkovitosti u fotokatalitičkoj razgradnji mikroplastike. Dvije kombinacije parametara, 80 °C uz snagu od 50 W te sobna temperatura uz 250 W, pokazala su se posebno učinkovitima za dobivanje filmova koji ubrzavaju razgradnju polimera.

Istraženi su različiti eksperimentalni uvjeti, uključujući vrste vodenih medija, debljina filmova, izvori svjetlosti i trajanje razgradnje. Najveći stupanj razgradnje postignut je u vodi iz slavine i u simuliranoj morskoj vodi nakon 48 sati izlaganja UV svjetlosti.

Zaključno, ovaj rad pokazuje kako se preciznim podešavanjem PEALD parametara mogu dobiti tanki filmovi cinkova oksida s povećanom fotokatalitičkom učinkovitošću te otvara mogućnosti za njihovu primjenu u razgradnji mikroplastike i u suvremenim tehnologijama pročišćavanja vode.

## Acknowledgements

I would like to express my deepest gratitude to all those who have supported and contributed to my PhD journey.

I am especially grateful to Assoc. Prof. Aleš Omerzu for his invaluable supervision during my studies. His expertise, attentive insights and critical feedback were essential in shaping my research and guiding my entire process. I would also like to thank Assoc. Prof. Robert Peter for his generous guidance and support on many aspects of my work, especially his expertise in XPS, which was fundamental to the development of this thesis.

My sincere thanks go to Dr. Matejka Podlogar for mentoring me during my six-month stay at the Jožef Stefan Institute, where I had the opportunity to expand my knowledge and collaborate with her talented team.

I am also very grateful to Assoc. Prof. Ivna Kavre Piltaver and Assoc. Prof. Ivana Jelovica Badovinac for training me in SEM. Their expertise provided me with the necessary skills to perform high quality imaging for my research.

Special thanks go to Tina Radošević, whose guidance on eSEM and TEM preparation was invaluable. Her careful guidance ensured reliable sample preparation and successful imaging throughout my project.

I am particularly grateful to Damjan Vengust for his training in Raman spectroscopy and his contributions to TEM. His expertise greatly enriched the scope and depth of my work.

I would also like to thank Karlo Veličan for his instruction in ALD at the beginning of this doctoral journey.

My thanks also go to Dr. Krešimir Salamon for his assistance with XRD analysis and interpretation and to Assist. Prof. Marko Perčić for his help with AFM analysis and visualization.

I am grateful for the financial support from the MOBDOK project (2023-9307) and the POMERI project (NPOO.C3.2.R2-I1.06.0083), both funded by the European Union, that made this research possible. I would also like to thank the POMERI members for the wonderful time we spent working together in the final years of this journey.

I owe my deepest thanks to my family for their invaluable support, not only during my PhD, but throughout all the steps that led me here. Their patience and faith in me were a constant source of strength.



# Contents

<b>Abstract</b>	<b>v</b>
<b>Sažetak</b>	<b>ix</b>
<b>1 Introduction</b>	<b>1</b>
<b>2 Fundamentals of Plasma-Enhanced Atomic Layer Deposition</b>	<b>5</b>
2.1 Principles of Atomic Layer Deposition . . . . .	5
2.1.1 Thin ZnO Films Deposited by ALD . . . . .	8
2.2 Overview of Plasma-Enhanced ALD . . . . .	10
2.2.1 Plasma Generation in Remote Capacitive-Coupled PEALD . . . . .	12
2.2.2 Thin ZnO Films Deposited Using PEALD . . . . .	13
<b>3 Photocatalytic Degradation of Organic Pollutants</b>	<b>17</b>
3.1 Overview of Heterogeneous Photocatalysis . . . . .	17
3.2 Zinc Oxide as a Photocatalyst . . . . .	20
3.3 Motivation for the use of thin ZnO films in Photocatalysis . . . . .	21
3.4 Model Pollutants . . . . .	22
3.4.1 Photocatalytic Degradation of Organic Dyes . . . . .	22
Methylene blue . . . . .	23
3.4.2 Photocatalytic Degradation of Microplastic Fibers . . . . .	23
Polyethylene terephthalate . . . . .	24
<b>4 Materials and Methods</b>	<b>27</b>
4.1 Synthesis of thin ZnO films with ALD and PEALD . . . . .	27
4.2 Thin Film Characterization Techniques . . . . .	28
4.2.1 X-ray Diffraction . . . . .	28
4.2.2 High-Resolution Transmission Electron Microscopy . . . . .	31

4.2.3	Scanning Electron Microscopy . . . . .	33
4.2.4	X-ray Photoelectron Spectroscopy . . . . .	35
4.2.5	UV-Vis Spectroscopy . . . . .	37
4.2.6	Secondary Ion Mass Spectrometry . . . . .	40
4.2.7	Photoluminescence Spectroscopy . . . . .	41
4.3	Photocatalytic Activity Testing . . . . .	41
4.3.1	Testing on Methylene Blue . . . . .	41
4.3.2	Testing on Microplastic Fibers . . . . .	44
<b>5</b>	<b>Results</b>	<b>47</b>
5.1	Comparative Photocatalytic Activity of ZnO Films: ALD vs PEALD . . . . .	47
5.2	Impact of Deposition Temperature on Photocatalytic Activity . . . . .	53
5.2.1	Role of Film Thickness . . . . .	53
5.2.2	Impact of Initial Methylene Blue Concentration . . . . .	54
5.2.3	Influence of Deposition Temperature . . . . .	55
5.3	Photocatalytic Performance under Different Light Sources . . . . .	64
5.4	Impact of Plasma Process Parameters . . . . .	66
5.5	Photodegradation of PET Microfibers . . . . .	71
5.5.1	Photocatalytic Performance of Thin ZnO Films Deposited at 80 ° C . . . . .	72
5.5.2	Photocatalytic Performance of Room-Temperature ZnO Films . . . . .	76
<b>6</b>	<b>Conclusion and Future Directions</b>	<b>83</b>
6.1	Summary of Findings . . . . .	83
6.2	Future directions . . . . .	84
	<b>Bibliography</b>	<b>87</b>

# List of Figures

2.1	Demonstration of good and poor uniformity and conformality. Thin films produced with ALD are uniform in thickness across the substrate. Adapted from [15]. . . . .	6
2.2	Four main steps of ALD cycle. . . . .	6
2.3	(a) The film thickness depends linearly on the number of ALD cycles; (b) the growth per cycle is constant in the temperature range called ALD window, and outside it can be increased or decreased due to A: condensation, B: decomposition of precursors, C: incomplete reactions, D: desorption of precursors. Adapted from [18]. . . . .	7
2.4	Four steps of a cycle in the deposition of thin ZnO films using ALD. . . . .	8
2.5	Most common PEALD configurations: (a) ICP configuration, (b) direct CCP configuration and (c) remote CCP configuration. Adapted from [55]. . . . .	12
2.6	Four steps of a cycle in the deposition of thin ZnO films using PEALD. . . . .	14
3.1	Mechanism of the heterogeneous photocatalytic process. . . . .	19
3.2	Positions of VB and CB of various semiconductors relative to the oxidation and reduction potentials of water. Adopted from [73]. . . . .	19
3.3	Structural formula of methylene blue. . . . .	23
3.4	Chemical structure of polyethylene terephthalate. . . . .	24
3.5	a) Schematic representation of the degradation process of PET microfibres under UV exposure. b) Fibre after degradation. . . . .	25
4.1	Schematic illustration of X-ray diffraction. . . . .	29
4.2	The orientation of the (002), (101) and (100) planes in ZnO films grown on a glass substrate. Adapted from [116]. . . . .	30
4.3	Preparation of thin films for cross-sectional TEM analysis. . . . .	32

4.4	In the SEM, the incident electron beam interacts with the sample surface and causes the emission of secondary electrons, backscattered electrons, characteristic X-rays and, if sufficiently thin, transmitted electrons. Adopted from [118]. . . . .	33
4.5	a) Schematic representation of the XPS process. Adopted from [118]. b) Photoemission process. Adopted from [119]. . . . .	35
4.6	a) Schematic representation of UV-Vis spectrofotometer. Adopted from [118]. b) Reflection, absorption and transmission of the incident beam. . . . .	38
4.7	Positions of the valence band and the conduction band as a function of momentum ( $k$ ) for (a) direct and (b) indirect bandgap semiconductors. . . . .	39
4.8	Schematic representation of SIMS spectrometer. Adopted from [118]. . . . .	40
4.9	Schematic illustration (left) and measured PL spectrum (right) of ZnO. . . . .	42
4.10	Time-dependent UV-Vis absorption spectra of MB during photocatalytic degradation under illumination in the range of 200–800 nm. . . . .	43
4.11	Semilogarithmic plot of $\ln(C(t)/C(0))$ against illumination time. The linear trend confirms the pseudo-first-order kinetics of the MB photodegradation, with the slope corresponding to the photodegradation constant $k$ as given by the equation 4.19. . . . .	43
5.1	SEM images of (a) ALD grown thin ZnO film and (b) PEALD grown thin ZnO film with grain size distribution. Deposition temperature for both films is 80 °C. . . . .	48
5.2	HR-TEM cross-sectional images of thin ZnO films deposited by (a) thermal ALD and (b) PEALD, together with the corresponding FFT analyses. . . . .	49
5.3	GIXRD analysis of thin ZnO films deposited with ALD and PEALD at same temperature of 80 °C. . . . .	49
5.4	XPS spectra around Zn 2 $p_{3/2}$ (a) and O 1s core-levels (b). . . . .	50
5.5	Optical absorption spectra (a) and corresponding Tauc plots (b) for thALD and PEALD grown thin ZnO films. . . . .	51
5.6	Photoluminescence spectra of ZnO films: (a) emission spectra for $\lambda_{\text{ex}} = 254$ nm; (b) excitation spectra $\lambda_{\text{em}} = 390$ nm . . . . .	51
5.7	(a) Photodegradation of MB during 7 hours of UV irradiation for thin ZnO films deposited with thermal ALD (red) and PEALD (blue). (b) A semi-logarithmic diagram was used to evaluate the photodegradation rate. . . . .	52
5.8	Stability of thin ZnO films deposited with thALD (a) and PEALD (b). . . . .	52

5.9	Photocatalytic performance of PEALD-grown thin ZnO films as a function of film thickness at a deposition temperature of 80 °C: photodegradation curves (a), corresponding first-order rate constants (b). . . . .	53
5.10	Photodegradation kinetics of MB at two initial concentrations (a). Comparison of our results at 5 mg/L with data from Rogé et al. [126], which show excellent agreement (b). . . . .	54
5.11	GPC of ZnO films deposited by PEALD at varying substrate temperatures with a fixed RF power of 50 W. . . . .	55
5.12	GIXRD diffractograms of ZnO films deposited with PEALD at different temperatures. . . . .	56
5.13	SEM images of thin ZnO films deposited with PEALD at different temperatures: 60 °C (a), 80 °C (b), 100 °C (c), 200 °C (d). . . . .	56
5.14	HRTEM analysis of ZnO thin films deposited at different temperatures: 60 °C (a), 80 °C (b), 100 °C (c), 200 °C (d). . . . .	57
5.15	XPS O 1s spectra of thin ZnO films deposited with PEALD at different temperatures (a). Corresponding Zn/O atomic ratio trends derived from XPS (b). . . .	58
5.16	Optical absorption spectra of ZnO films deposited at different temperatures. . .	59
5.17	Tauc plots for ZnO films deposited at 60 °C (a), 80 °C (b), 100 °C (c) and 200 °C (d), used to evaluate the optical band gap energies from the absorption spectra. . . . .	60
5.18	Photoluminescence spectra of PEALD-ZnO films excited for excitation wavelength of 320 nm. . . . .	61
5.19	Band gap energy and fluorescence energy of PEALD-grown ZnO films as a function of deposition temperature (a). Difference between band gap energy and fluorescence energy as a function of deposition temperature (b). . . . .	62
5.20	Photodegradation curves of MB in aqueous solution under UV irradiation for PEALD-ZnO films deposited at different temperatures (a). Corresponding photocatalytic rate constants ( <i>k</i> ) in comparison between thermal ALD and PEALD processes (b). . . . .	63
5.21	UV-Vis absorption spectra of ZnO thin films prepared by ALD and PEALD (a). Tauc plots used to evaluate the optical band gap of the ZnO thin films (b). . . .	65
5.22	SEM images of ZnO films deposited by ALD (a) and PEALD (b). . . . .	65
5.24	GIXRD patterns of ZnO films deposited at room temperature with different plasma RF powers. . . . .	67

5.25	High-resolution TEM images of PEALD-ZnO films deposited at different RF powers: 250 W (a) and 100 W (c), with corresponding electron diffraction (SAED) patterns (b) and (d). . . . .	68
5.26	XPS spectra around the O 1s core-levels for the ZnO thin films deposited at room temperature. . . . .	69
5.27	UV-Vis absorption spectra (a) and Tauc plot (b) of ZnO films deposited with PEALD at room temperature. . . . .	69
5.28	Photodegradation curve of MB under UV light irradiation for ZnO films deposited at room temperature with different plasma RF powers (a). Variation of the photodegradation constant as a function of the PEALD plasma RF power (b). . . . .	70
5.29	Photodegradation curves of MB under UV illumination in the presence of different scavengers: isopropyl alcohol (IPA), EDTA-2Na and silver nitrate ( $\text{AgNO}_3$ ) (a). Corresponding histograms showing the photodegradation efficiency of MB after 120 minutes of exposure (b). . . . .	71
5.30	No significant photodegradation observed with ultra-thin ZnO@80 °C films after 6 h of UV exposure: a) 0 cycles (control sample), b) 80 cycles; c) 100 cycles; d) 120 cycles. . . . .	72
5.31	Surface of an untreated PET microfibre (a), PET microfibre with 360 PEALD cycles of ZnO@80 °C (c). Cross-section of an untreated PET microfibre (b) and a PET microfibre with a 360 PEALD cycles of thin ZnO@80 °C film. . . . .	73
5.33	Photodegradation of PET microfibres after 48 hours of exposure to UV light: without catalyst in Milli-Q water (a), with ZnO@80 °C in Milli-Q water (b), and with ZnO@80 °C in tap water (c). Photodegradation of PET microfibres after 48 hours of exposure to simulated sunlight (SS), microfibres without catalyst (d), with ZnO@80 °C in Milli-Q water (e), and with ZnO@80 °C in tap water (f). . . . .	74
5.34	Photodegradation of PET microfibres in 38‰ NaCl solution after 48 hours of exposure to UV light without catalyst (a) and with ZnO@80 °C (b); and after exposure to simulated sunlight (SS) without catalyst (c) and with ZnO@80 °C (d). . . . .	75
5.35	eSEM images of PET fibres: pristine surface (a); after 40 cycles of ZnO@RT (b); after 40 cycles of ZnO@RT and 1 h UV irradiation (c); after 40 cycles of ZnO@RT, 1 h UV and another 40 cycles of ZnO@RT (d); after two sequential ZnO@RT (40 cycles) and 1 h UV steps (e). . . . .	76

5.36	Photodegradation of PET microfibres: untreated PET (a); PET coated with 200 cycles of ZnO@RT (b); PET coated with 200 cycles of ZnO@RT after 16 hours of UV exposure (c); and after 48 hours of UV exposure (d). . . . .	77
5.37	Photodegradation of PET microfibres in Milli-Q water with and without ZnO@RT after 48 hours of exposure to UV light without ZnO (a) and with ZnO (b); and after exposure to simulated sunlight without ZnO (c) and with ZnO (d). . . . .	78
5.38	Cross-sectional analysis of PET fibres. Untreated PET (a,same as 5.31b); after 48 h UV exposure with ZnO@RT (b); after 48 h simulated sunlight exposure with ZnO@RT (c). . . . .	79
5.39	Photodegradation of PET microfibres in 38 ‰ NaCl solution after 48 hours of exposure to UV light without ZnO@RT (a) and with ZnO@RT (b); and after exposure to simulated sunlight without ZnO@RT (c) and with ZnO@RT (d). . . . .	80
5.40	Histogram presenting the highest photodegradation efficiencies of PET under various experimental conditions. Each bar represents the photodegradation performance achieved for a specific set of parameters: catalyst type, medium, light source and irradiation time. . . . .	80



## List of Tables

4.1	Measured pH values and electrical conductivities ( $\kappa$ ) of aqueous media used as a medium for PET degradation. The media tested included ultrapure water (Milli-Q), tap water and a 0.65 M NaCl solution. . . . .	45
5.1	Average peak areas for O1s and Zn 2p <sub>3/2</sub> at different deposition temperatures and the corresponding Zn/O ratios. . . . .	59
5.2	Band gap ( $E_g$ ) and florescence energy ( $E_f$ ) values for different deposition temperatures. . . . .	62
5.3	Results of photodegradation for various catalysts in different media and under different lighting conditions. . . . .	82



# List of Abbreviations

<b>ALD</b>	Atomic Layer Deposition
<b>BED</b>	Backscattered Electron Detector
<b>CB</b>	Conduction Band
<b>CBS</b>	Concentric Backscatter Detector
<b>CCP</b>	Capacitively Coupled Plasma
<b>CVD</b>	Chemical Vapor Deposition
<b>DEZ</b>	Diethylzinc
<b>DMZ</b>	Dimethylzinc
<b>EDS</b>	Energy Dispersive X-ray Spectroscopy
<b>eSEM</b>	Environmental Scanning Electron Microscopy
<b>FFT</b>	Fast Fourier Transform
<b>FIB</b>	Focused Ion Beam
<b>GIXRD</b>	Grazing Incidence X-ray Diffraction
<b>GPC</b>	Growth per Cycle
<b>ICP</b>	Inductively Coupled Plasma
<b>LED</b>	Lower Electron Detector
<b>LFD</b>	Large Field Detector
<b>MB</b>	Methylene Blue
<b>PEALD</b>	Plasma-Enhanced Atomic Layer Deposition
<b>PET</b>	Polyethylene Terephthalate
<b>PIPS</b>	Precision Ion Polishing System
<b>RF</b>	Radio Frequency
<b>ROS</b>	Reactive Oxygen Species

<b>SAED</b>	Selected Area Diffraction
<b>STEM</b>	Scanning Transmission Electron Microscopy
<b>UV</b>	Ultraviolet
<b>UED</b>	Upper Electron Detector
<b>VB</b>	Valence Band
<b>XPS</b>	X-ray Photoelectron Spectroscopy
<b>XRD</b>	X-ray Diffraction
<b>XRR</b>	X-ray Reflectivity

# Chapter 1

## Introduction

The increasing pollution of ecosystems with organic pollutants, including dyes, pharmaceuticals and microplastics, represents a significant threat to the environment and human health [1]. The World Health Organisation has recognised the scale of microplastic pollution and highlighted its global significance [2, 3]. Conventional methods for degrading microplastics, such as mechanical filtration and chemical oxidation, have shown limited effectiveness [4].

Among the various approaches, photocatalysis has emerged as a transformative technology for the degradation of organic pollutants, as it can harvest photon energy and use it for the production of reactive oxygen species [5]. In photocatalysis, semiconductor materials such as titanium dioxide ( $\text{TiO}_2$ ) and zinc oxide ( $\text{ZnO}$ ) absorb light energy and generate electron-hole pairs that stimulate redox reactions to break down organic pollutants into less harmful compounds. When a photon with energy equal to or greater than the band gap of the semiconductor is absorbed, an electron is excited from the valence band to the conduction band, leaving behind a positively charged hole. The excited electron can reduce dissolved oxygen to form superoxide radicals ( $\text{O}_2^{\bullet-}$ ), while the hole can oxidise water or hydroxide ions to generate hydroxyl radicals ( $\bullet\text{OH}$ ). These reactive oxygen species act as powerful oxidants that attack and decompose organic contaminants. The photocatalytic process offers several advantages, such as ease of use, low energy requirements and the potential for complete mineralisation of pollutants, i.e. their degradation into inorganic end products such as carbon dioxide, water and mineral salts. However, the efficiency of photocatalysis is highly dependent on the properties of the semiconductor materials used, in particular their structure and optical properties.

Among semiconductor photocatalysts,  $\text{ZnO}$  has attracted particular interest due to its favourable band gap, high electron mobility and cost efficiency. In addition,  $\text{ZnO}$  exhibits strong photocatalytic activity under ultraviolet (UV) light and has already been successfully used to degrade

dyes [6], pharmaceuticals [7] and microplastics [8].

Despite the advantages of ZnO, conventional deposition methods such as sol-gel [9] and various sputtering techniques [10, 11] offer limited control over film thickness, uniformity and composition, which prevents optimal photocatalytic performance.

To overcome these challenges, atomic layer deposition (ALD) and its plasma-enhanced variant (PEALD) have proven to be promising techniques for the production of high-quality ZnO films. ALD enables the precise control of film thickness at the atomic level through self-limiting surface reactions, resulting in uniform and conformal films on complex 3D geometries [12]. PEALD, which utilises plasma to enhance the deposition process, further improves the film properties by increasing the reactivity of the precursors and enabling lower deposition temperatures [12]. This capability is particularly beneficial for applications where temperature-sensitive substrates are used. The combination of ALD and plasma technology offers an exciting opportunity to customise the properties of ZnO films for improved photocatalytic performance.

Despite the progress made with PEALD, the relationship between deposition parameters, such as temperature and plasma power, and the resulting photocatalytic activity is still poorly understood. This knowledge gap inhibits the optimisation of ZnO films for practical applications in environmental remediation. Therefore, the aim of this study is therefore to systematically investigate how different deposition parameters influence the properties and photocatalytic efficiency of ZnO films synthesised with PEALD.

The presented doctoral thesis aimed to achieve the following goals:

1. Synthesis of high quality ZnO thin films using plasma-enhanced atomic layer deposition for enhanced photocatalytic efficiency.
2. Determination of the synthesis parameters for the photocatalysts to achieve the maximum rate of photocatalytic degradation of dyes.
3. Establish a correlation between the structural and electronic properties of the synthesised films and their photocatalytic properties.
4. Demonstrate the application of the most efficient thin ZnO films for the photocatalytic degradation of microplastics.

Thin ZnO films, which are well suited for the photocatalytic degradation of microplastics, can be synthesized using the PEALD synthesis process by optimizing the synthesis parameters.

The structure of this thesis is given as follows. In Chapter 2, the fundamentals of ALD are presented, with emphasis on the plasma-enhanced variant, which is used as the core method in this study. The mechanisms of film growth, plasma generation and the specific properties of ZnO thin films produced using these techniques are discussed.

In Chapter 3, the concept of heterogeneous photocatalysis is introduced, together with an overview of ZnO as a photocatalytic material. The motivation for the use of thin ZnO films in photocatalytic applications is explained and the selected model pollutants are described.

In Chapter 4, the experimental procedures are described. The parameters for the synthesis of ZnO films using ALD and PEALD are given. The techniques used for film characterization, such as XRD, SEM, TEM, XPS, UV-Vis spectroscopy, SIMS and PL, are presented. The methodology for testing the photocatalytic activity of the films is also explained.

In Chapter 5, the experimental results are presented and discussed. This includes a comparative evaluation of the ZnO thin films produced by ALD and PEALD. The influence of the deposition temperature on the photocatalytic activity is analyzed. In addition, the effects of different light sources and aqueous environments on the photocatalytic efficiency are evaluated. Finally, the photocatalytic degradation of microplastic fibres with ZnO films is presented.

In Chapter 6, the most important results of the study are summarised and possible directions for future research are suggested.



## Chapter 2

# Fundamentals of Plasma-Enhanced Atomic Layer Deposition

This chapter gives a brief overview of the basic concepts of plasma-enhanced atomic layer deposition, the synthesis technique used in this thesis. Since the basic principles of atomic layer deposition are essential for understanding the plasma-enhanced variant, the first section begins with a brief introduction to ALD. This is followed by a general overview of PEALD and a description of plasma generation in a remote capacitively coupled reactor. The final section deals specifically with the deposition of ZnO thin films using PEALD, a material of interest in this thesis.

### 2.1 Principles of Atomic Layer Deposition

Atomic layer deposition is an advanced thin film deposition process known for its ability to produce highly conformal and uniform films with precise thickness control [13, 14]. In this context, good uniformity refers to the even distribution of the film across a surface, while good conformality means consistent thickness even within pores and on complex surfaces (Fig. 2.1). ALD is a specialized form of chemical vapor deposition (CVD), a method of introducing gaseous precursors into a reaction chamber [13]. Unlike CVD, where precursors are introduced simultaneously and may react in the gas phase, ALD involves alternating pulses of precursors, separated by an inert gas purge [13, 16]. This controlled alternation prevents gas-phase reactions, ensuring that the surface reactions are self-limiting and that the film grows layer-by-layer at the atomic scale [17]. Self-limiting means that a chemical reaction stops by itself after the formation of a single layer of material. This happens because once a surface is completely covered with a

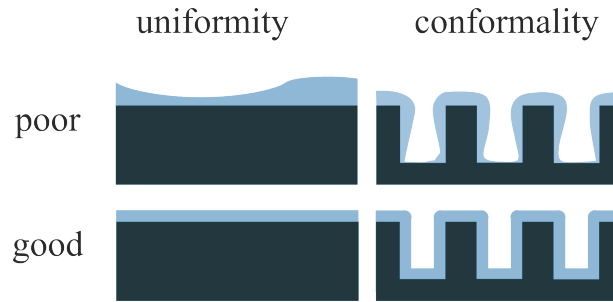


**Figure 2.1:** Demonstration of good and poor uniformity and conformality. Thin films produced with ALD are uniform in thickness across the substrate. Adapted from [15].

layer of molecules, it is no longer reactive enough to continue depositing until the next reaction step [12].

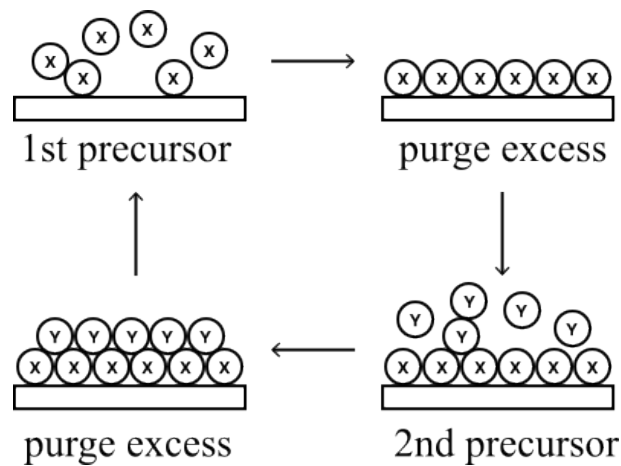


**Figure 2.2:** Four main steps of ALD cycle.

The ALD process consists of a series of cycles (cy), each involving four main steps [18] as shown in Figure 2.2:

1. **Pulse of the first precursor:** the first gaseous precursor is introduced into the reaction chamber, where it chemisorbs onto the substrate surface.
2. **Purge of excess precursor:** an inert gas, such as nitrogen or argon, is used to remove any unreacted precursor and by-products from the chamber.
3. **Pulse of the second precursor:** the second precursor is then introduced, reacting with the chemisorbed layer from the first precursor, forming the desired thin film.

- Purge of excess precursor:** again, an inert gas purge removes any remaining precursor and reaction by-products, completing the cycle.

In the initial stage of film growth, the first few atomic layers form at isolated nucleation sites [19]. Once these islands merge, the film thickness in ALD increases linearly with the number of deposition cycles (Fig. 2.3a). The rate of deposition is known as the growth per cycle (GPC). For each ALD process, the GPC remains constant within a specific temperature range, referred to as the ALD window [12]. Within this window, the reactions are self-limiting, as described earlier. Outside the ALD window, different mechanisms come into play, leading to non-ideal growth (Fig. 2.3b). The GPC can increase at temperatures below the ALD window due to precursor

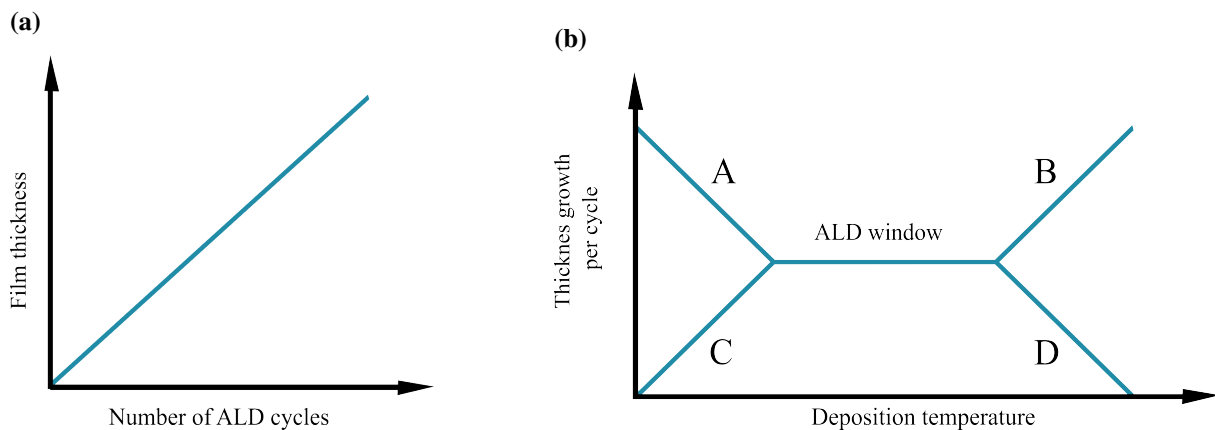


**Figure 2.3:** (a) The film thickness depends linearly on the number of ALD cycles; (b) the growth per cycle is constant in the temperature range called ALD window, and outside it can be increased or decreased due to A: condensation, B: decomposition of precursors, C: incomplete reactions, D: desorption of precursors.

Adapted from [18].

condensation (A), where the precursor continues to physisorb on the substrate. Similarly, the GPC can rise for temperatures above the ALD window (B) due to precursor decomposition. In this scenario, the decomposition products attach to multiple surface sites without reaching saturation, leading to continuous growth, a process similar to that in CVD mode. Conversely, a lower GPC can occur due to incomplete reactions below the ALD window temperatures (C) or because of precursor desorption at temperatures above the ALD window (D) [18, 20].

In addition to the substrate temperature during deposition, which has the greatest influence on GPC and film properties, there are other important synthesis parameters to consider. Firstly, the duration and flow rate of the precursor pulses must be sufficient to achieve self-limiting reactions, especially with more complex substrates [12]. Similarly, the purging process should be long

enough to remove all unbound precursors effectively [21]. Additionally, an optimized process for one precursor or substrate may not apply to a different precursor or substrate [12]. In this work, silicon wafers, glass and quartz were used as substrates to optimize the synthesis parameters for the maximum photocatalytic degradation of dyes. The optimal parameters determined were then applied to the deposition on microplastic substrates, although the deposition behavior on this material could be different [22].

### 2.1.1 Thin ZnO Films Deposited by ALD

Zinc oxide (ZnO) is a widely studied metal oxide that can be conveniently synthesized using atomic layer deposition. Various zinc precursors have been reported for ALD synthesis, including zinc acetate [23, 24, 25], zinc chloride [26], dimethylzinc (DMZ) [25, 27, 28], diethylzinc (DEZ) [25, 27, 28, 29] and elemental zinc [30]. Among these, diethylzinc ( $\text{Zn}(\text{C}_2\text{H}_5)_2$ , DEZ) is the most commonly used due to its high volatility, reactivity and stability [31].

In ALD processes employing DEZ, deionized water is typically used as the oxygen source, while nitrogen ( $\text{N}_2$ ) serves as the purge gas to remove excess reactants and by-products. This process is schematically illustrated in Figure 2.4.

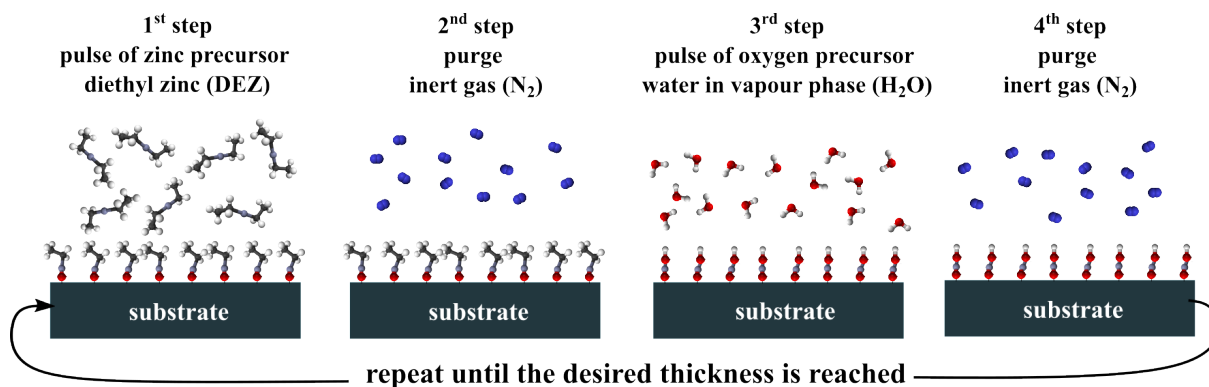
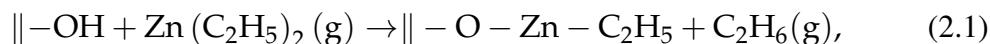


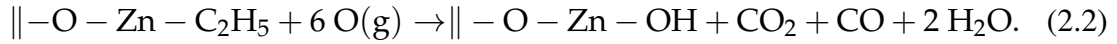
**Figure 2.4:** Four steps of a cycle in the deposition of thin ZnO films using ALD.

The ALD growth mechanism consists of alternating half-reactions. Based on Musschoot [32], the reaction sequence for DEZ and water can be described as follows:

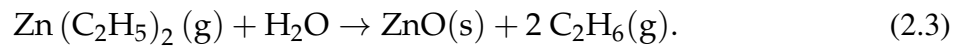
1. The surface hydroxyl groups react with DEZ, forming a surface-bound ethyl-zinc species and releasing ethane gas:



2. The ethyl-zinc species reacts with water in the following half cycle, regenerates the hydroxyl groups of the surface and forms a ZnO layer and releases by-products:



The overall reaction can be summarized as:



This process is usually carried out in a temperature range from 60 °C to 300 °C, with the optimal window being 120 °C to 200 °C for Si substrate [33]. Under these conditions, an average GPC of 1.5 – 2.3 Å/cy is achieved [33, 34].

As is common in other films, ZnO grows as isolated islands that coalesce after a few cycles to form a continuous film [35]. The deposited films generally adopt a hexagonal wurtzite structure, the most thermodynamically stable and commonly observed crystalline phase of ZnO. The crystal orientation of these films is influenced by several factors, including the choice of precursors, the deposition temperature, the substrate material and the purging conditions [24].

The properties of thin ZnO films grown with ALD can be further tailored through various treatments and doping strategies. Pre-treatment [36], post-deposition annealing [37] and plasma treatment [38] can significantly change film characteristics, including conductivity, optical properties and morphology. Doping is another effective strategy to optimise ZnO properties [39]. Among the dopants, aluminum is extensively studied. It can be easily incorporated into ALD-grown ZnO by alternating ZnO and aluminum oxide (Al<sub>2</sub>O<sub>3</sub>) layers during deposition, resulting in aluminum-doped ZnO films with improved conductivity and transparency [34]. In addition to doping with metals, strategies for doping with non-metals have also been researched in order to improve the properties of ZnO. One common approach is doping with hydrogen, which can increase the charge carrier concentration and change the electronic structure [40]. In addition, the formation of nanolaminates, such as ZnO/TiO<sub>2</sub> heterojunctions, is used for applications that require customised band alignment and improved charge transport properties [41].

ALD-deposited thin ZnO films are used in many areas. One important application is transparent conductive oxides, where ZnO films are used as transparent and conductive layers in devices such as flat panel displays, touch screens and photovoltaic cells [42]. Their high transparency in

the visible spectrum combined with electrical conductivity makes them an excellent alternative to indium tin oxide, especially for applications where cost efficiency and earthbound materials are important [34]. Thin ZnO films are also commonly used in gas sensors due to their high sensitivity to various gasses [43], such as volatile organic compounds and environmental pollutants such as nitrogen oxides [44, 45]. These sensors are important for environmental monitoring and industrial safety applications. The piezoelectric properties of ZnO also make it an ideal material for microelectromechanical systems, where it is used in devices such as actuators and sensors [46]. The strong ultraviolet absorption capability of ZnO has led to its widespread use in UV-protective coatings for various surfaces, as well as in sunscreens, where it serves as a physical UV filter [47]. Additionally, the photocatalytic properties of ZnO under UV illumination are exploited in various environmental applications. More detailed information on the photocatalytic activity of ZnO is provided in Section 3.2. The combination of these different functions demonstrates the versatility of thin ZnO films and underlines their importance for the further development of technologies in various fields.

In ALD, even if it is referred to as low-temperature deposition, the deposition temperatures are rarely below 80 °C [48, 49], as extremely low temperatures can lead to incomplete reactions and poor film quality. Nucleation and growth rates can also be slower [50], especially on non-ideal substrates such as polymers where surface activation is limited [51, 52, 53]. Also, one must be careful when claiming that a certain precursor combination enables thermal ALD at low temperatures without considering the resulting film properties for specific applications. For example, while DEZ/H<sub>2</sub>O can form ZnO films below 80 °C, Al-doped ZnO shows a drastic drop in conductivity from 750 S/cm at 150 °C to only 3 S/cm at 80 °C, which makes it unsuitable for transparent electrodes in optoelectronics [54]. Plasma-enhanced atomic layer deposition offers a solution to this challenge by utilising a plasma as an energy source. Plasma activation increases surface reactivity and enables faster growth and better film quality at lower temperatures.

## 2.2 Overview of Plasma-Enhanced ALD

Plasma-enhanced atomic layer deposition is a variant of ALD that extends the capabilities of conventional ALD by using a plasma to generate reactive species such as ions, radicals and excited molecules. These reactive species can activate or enhance surface reactions, enabling processing at lower temperatures, which is important for temperature-sensitive substrates and provides access to new material properties and compositions [55]. The main difference to thermal ALD lies in the plasma exposure step instead of the second precursor pulse. In this step,

plasma gas is introduced into the chamber, creating a flux of highly reactive species (radicals and ions). This step not only increases the reactivity of the surface reactions, but can also enable the deposition of materials that are difficult or impossible to grow at lower temperatures in the thermal ALD due to the insufficient reactivity of the precursors. The ability to deposit films at lower temperatures expands the range of materials that can be used as substrates, e.g. polymers. In addition, growth rates are often higher with the PEALD process because the plasma has a higher reactivity, which enables shorter deposition times compared to purely thermal processes. In addition to the substrate temperature, the plasma conditions are the most important parameters in PEALD synthesis. These conditions include the reactor configuration, the plasma power and the duration of the plasma treatment. The plasma power determines the density and energy of the reactive species produced. A higher power increases the density of ions and radicals, but also carries the risk of uncontrolled synthesis and damaging the substrate. The duration of the plasma treatment determines how long the reactive species interact with the substrate and thus influences the quality, uniformity and composition of the film.

Two types of plasma reactors are used for PEALD synthesis, depending on how the electrical energy is coupled into the plasma: inductively coupled plasma (ICP) and capacitively coupled plasma (CCP). In an ICP reactor, as shown in Fig. 2.5a, an radio-frequency (RF) power supply drives a coil to generate a magnetic field that ionises the gas and creates a high density plasma ( $n_e \sim 10^{10} - 10^{12} \text{ cm}^{-3}$ ) and moderate electron temperatures ( $T_e \sim 1 - 5 \text{ eV}$ ) [55]. This configuration is ideal for achieving uniform plasma conditions with minimal damage from ion bombardment, promoting effective surface reactions even at low substrate temperatures. A CCP reactor uses an RF source to generate a plasma between two electrodes, a powered electrode and a grounded electrode. It can be configured as follows:

- Direct CCP (Fig. 2.5b): the substrate is placed directly on the grounded electrode and thus exposed to a plasma with relatively high ion energies, which can improve surface cleaning but carries the risk of substrate damage [53]. The plasma density in direct CCP is usually in the range of  $10^8$  to  $10^{10} \text{ cm}^{-3}$  [55].
- Remote CCP (Fig. 2.5c): a semi-transparent, grounded electrode is placed between the power electrode and the substrate to reduce ion bombardment and provide a gentler plasma exposure, suitable for sensitive substrates. For remote CCP systems, the electron density can be at the lower end of the scale (approximately  $10^{10} \text{ cm}^{-3}$ ) as the plasma is generated at some distance from the substrate and the reactive species must travel through the chamber to reach the substrate [55].

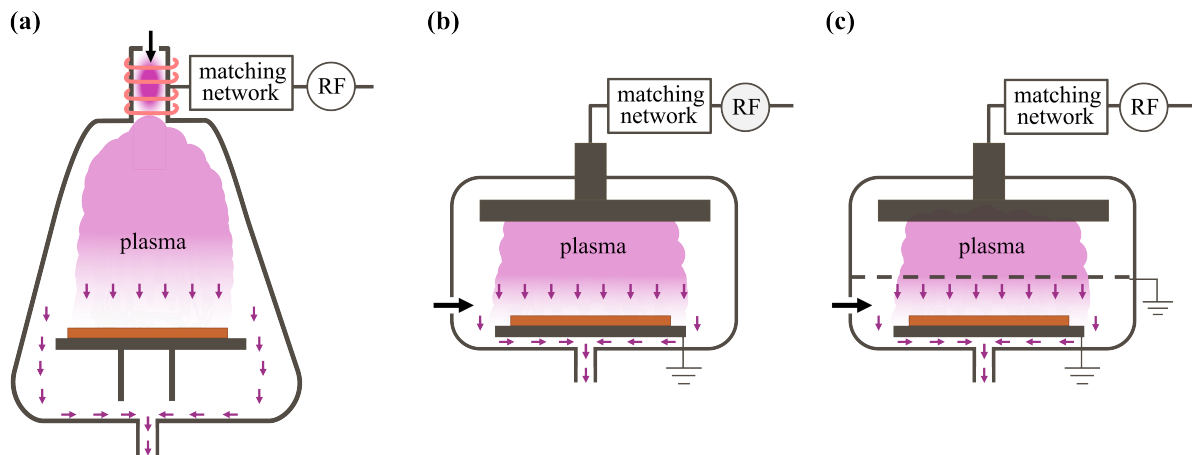


**Figure 2.5:** Most common PEALD configurations: (a) ICP configuration, (b) direct CCP configuration and (c) remote CCP configuration. Adapted from [55].

Different reactor configurations influence the crystal structure, density and properties of the deposited films [53]. ICP reactors with their high-density plasma and low ion energies are better suited for uniform deposition on temperature-sensitive materials. In contrast, direct CCP reactors can enable more aggressive surface cleaning or etching, but can also cause damage. Remote CCP reactors provide a balance by minimizing damage to the substrate while still allowing effective deposition [53].

### 2.2.1 Plasma Generation in Remote Capacitive-Coupled PEALD

As already mentioned, in a capacitively coupled plasma system, an alternating voltage with a radio frequency of 13.56 MHz is applied between two electrodes in a low-pressure gas environment. This RF power generates an oscillating electric field that accelerates electrons between the electrodes. These electrons collide with neutral gas atoms or molecules, ionise them and form a plasma. The electrode connected to the RF power supply is the power electrode, while the other electrode is grounded. The rapidly alternating electric field causes the electrons to oscillate back and forth, gaining enough energy to ionise the gas molecules and maintain the plasma [55]. The electric field accelerates the ions onto surfaces, such as a substrate, which is advantageous for material processing.

In order to transmit the RF signal efficiently from the generator to the plasma chamber, it is important to match the impedance of the RF generator to that of the plasma chamber or the RF supply network. The matching network adjusts this impedance to ensure optimal power transfer from the RF source to the plasma and minimise power reflection back to the generator.

This efficient power transfer is important to maintain the stability of the plasma and achieve the desired conditions for PEALD.

The ALD system used in the experimental setup is the Beneq TFS 200, a CCP reactor that can be operated in both direct and remote configurations thanks to its removable grid. It was used in the remote configuration for all experiments in this work. Also in this system, the matching network consists of two capacitors: a load capacitor ( $C_L$ ) and a tuning capacitor ( $C_T$ ). The load capacitor matches the impedance of the RF power source to the load impedance of the plasma chamber and thus ensures efficient power transmission. The tuning capacitor can be precisely adjusted to ensure optimal matching when process conditions or operating frequencies change [56]. By properly adjusting  $C_L$  and  $C_T$ , plasma conditions can be optimized, resulting in better film quality and better control over the deposition process [57]. The Beneq TFS 200 automatically adjusts  $C_L$  and  $C_T$  to minimise reflected power. The operator must ensure that this automatic function works correctly. Stable plasma conditions can be achieved by carefully controlling the plasma parameters and impedance matching. This is crucial for precise film deposition in PEALD.

### 2.2.2 Thin ZnO Films Deposited Using PEALD

With a clear understanding of how plasma is generated and controlled in a PEALD system, we can now explore how this process is utilized to deposit thin ZnO films using PEALD. Various zinc precursors were investigated for the deposition of ZnO using PEALD, including dimethylzinc (DMZ) and bis-3-(N,N-dimethylamino)propyl-zinc ( $[Zn(DMP)_2]$ , BDMPZ) [45, 58]. Despite these alternatives, DEZ remains the most widely used precursor [59].

DEZ reacts readily with oxygen-containing plasma species to form ZnO. During the plasma step, oxygen ( $O_2$ ) is usually used as a gas source, which is ionized in the plasma and generates oxygen radicals ( $O$ ,  $O_2^+$ ,  $O_2^-$ ), ions, and excited molecules. These highly reactive species enable efficient oxidation reactions with the chemisorbed DEZ layer, leading to the formation of ZnO. In the last step of a cycle, all by-products generated during the process are removed by purging with an inert gas.

According to Musschot [32], the PEALD process for ZnO involves two alternating half-reactions:

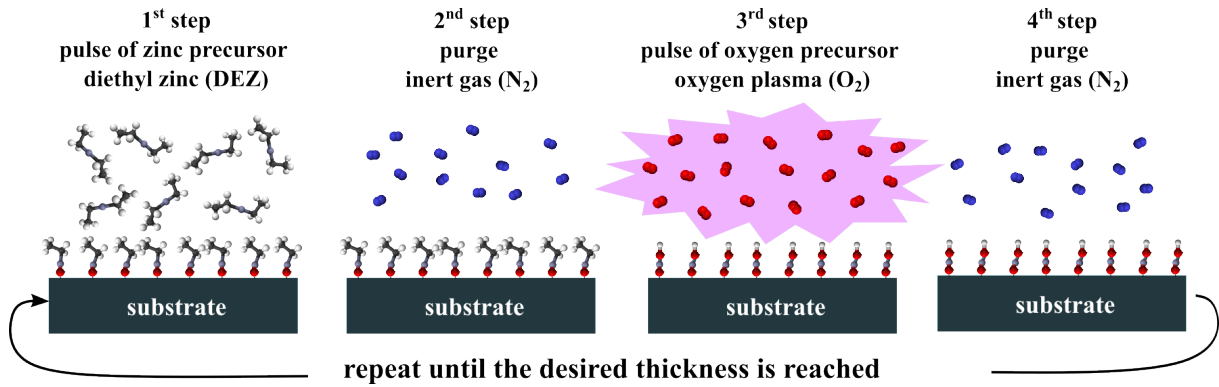
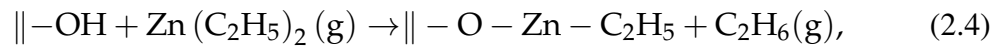
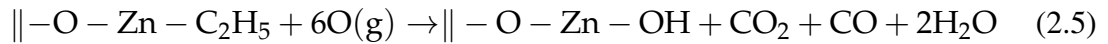


**Figure 2.6:** Four steps of a cycle in the deposition of thin ZnO films using PEALD.

1. The first half-reaction involves the reaction of surface hydroxyl groups with DEZ, forming a surface-bound ethyl-zinc species and releasing ethane gas:



2. In the second half-reaction, the ethyl-zinc species reacts with oxygen radicals or other plasma-generated oxygen species, regenerating surface hydroxyl groups and releasing volatile by-products such as  $\text{CO}_2$ ,  $\text{CO}$ , and  $\text{H}_2\text{O}$ :



The initial interest in PEALD ZnO was primarily driven by its potential applications in thin-film transistors [60, 61, 62]. Over time, research expanded to other areas, including resistive switching memory [63, 64], solar cells [65], Schottky diodes [66] and gas sensors [45].

Comparative studies between thermal ALD and PEALD were performed to evaluate the differences in film properties. Kim et al. [50] and Zhang et al. [64] analysed the effects of plasma exposure on film quality, while Thomas et al. [62] investigated plasma-enhanced thermal ALD (PET-ALD), a hybrid approach that combines elements of both techniques to optimise film properties.

The influence of different plasma configurations and substrate materials on the growth of PEALD ZnO was also investigated. Napari et al. [53] investigated room temperature deposition using different plasma configurations - ICP, direct CCP and remote CCP - on substrates such as silicon (Si), polymethyl methacrylate (PMMA) and polycarbonate (PC). Their results showed that ICP

and remote CCP produced amorphous films, while direct CCP resulted in more crystalline films, but also caused surface roughening on polymer substrates. Pilz et al. [67] examined the influence of RF power on the optical and structural properties of ZnO films deposited by direct CCP. In a subsequent study, they investigated the effects of deposition temperature under the same plasma configuration [68]. More recently, Castillo-Saenz et al. [69] have shown that under optimised direct CCP conditions, ZnO films can be successfully deposited on Si, quartz and ITO/PET without damaging the substrate.

Considering the importance of plasma conditions for tuning the properties of ZnO, our investigation focuses on the deposition of ZnO to determine the best synthesis parameters for photocatalytic applications. Since one goal is the deposition of thin ZnO films on microplastic fibres, we need to ensure that the films are deposited without damaging the polymer substrates. Therefore, the remote CCP was chosen as the plasma configuration because it enables deposition at low temperatures while preserving the integrity of the substrate.

In the following chapter, we examine the principles of photocatalysis and the mechanisms by which ZnO utilises light energy to degrade organic pollutants. We also discuss its potential for environmental remediation, particularly in the degradation of polymers such as poly(ethylene terephthalate) (PET).



## Chapter 3

# Photocatalytic Degradation of Organic Pollutants

This chapter provides a general overview of the photocatalytic degradation of organic pollutants. In the first section, the basic principles of heterogeneous photocatalysis are presented, focussing on zinc oxide as a photocatalyst. Subsequently, the motivation for the use of thin ZnO films in photocatalytic applications is briefly discussed. In the following sections, two groups of model pollutants are considered: organic dyes and microplastic fibres. The degradation of methylene blue is presented as a representative example of dye removal, while polyethylene terephthalate (PET) is used to investigate the potential of photocatalysis in the treatment of microplastics.

### 3.1 Overview of Heterogeneous Photocatalysis

Photocatalysis is a process in which light energy, typically in the ultraviolet or visible range, activates a semiconductor material to accelerate chemical reactions on its surface. Unlike conventional thermal catalysis, where heat serves as the main driver for the reactions, photocatalysis uses the energy of photons to initiate and sustain a series of physical and chemical processes. The key to this process is the interaction between light and a semiconductor. The semiconductor excites charge carriers when irradiated with light of a suitable wavelength, resulting in the formation of electron-hole pairs. These charge carriers in turn play a crucial role in enabling redox reactions on the surface of the semiconductor [70]. The efficiency of the photocatalytic processes depends on the physical properties of the semiconductor, e.g. its band gap, the recombination rate of the charge carriers and the properties of the surface of the catalyst [71].

The mechanism of photocatalysis is shown in Figure 3.1. The first step of photocatalysis is the absorption of light by the semiconductor material. When a photon with an energy equal to or greater than the band gap of the material is absorbed, it excites an electron from the valence band (VB) to the conduction band (CB), leaving a positively charged "hole" in the VB. Once the electron has been excited into the CB, it becomes a free carrier with a negative charge, while the hole remaining in the VB behaves like a carrier with a positive charge. Once electron-hole pairs are formed, they migrate to the surface of the semiconductor where they can participate in redox reactions. On their way to the surface, they can collide with the carrier of the opposite charge and annihilate themselves. This process is called recombination. In order to obtain an effective photocatalyst, the recombination rate should be low. Several strategies have been developed to mitigate recombination, including doping the semiconductor with certain elements, using co-catalysts or constructing nanostructures to enhance the spatial separation of charge carriers [71]. These methods can extend the lifetime of the electron-hole pairs, thereby increasing the likelihood that they will participate in surface reactions.

At the surface of the semiconductor, the photogenerated charge carriers interact with the surrounding molecules, typically oxygen, water or other adsorbed species, to initiate redox reactions. Such reactions are often the driving force behind the degradation of organic pollutants. For example, the electron in CB can reduce oxygen molecules adsorbed on the catalyst surface to superoxide anions ( $O_2^-$ ):



At the same time, the positively charged holes in VB can oxidize water molecules or hydroxide ions and form hydroxyl radicals ( $\bullet OH$ ):



Hydroxyl radicals and superoxide anions are reactive oxygen species (ROS) that are non-selective and highly reactive in the degradation of complex organic molecules, including persistent pollutants such as microplastics [72]. Hydroxyl radicals are characterised by their strong oxidative potential and are even able to cleave carbon-carbon bonds in polymers and initiate their decomposition into smaller fragments [72].

The role of the band gap and the relative positions of the conduction and valence bands in a semiconductor are crucial for photocatalytic efficiency. The band gap determines the energy threshold required for electron excitation. The positions of CB and VB must align with the

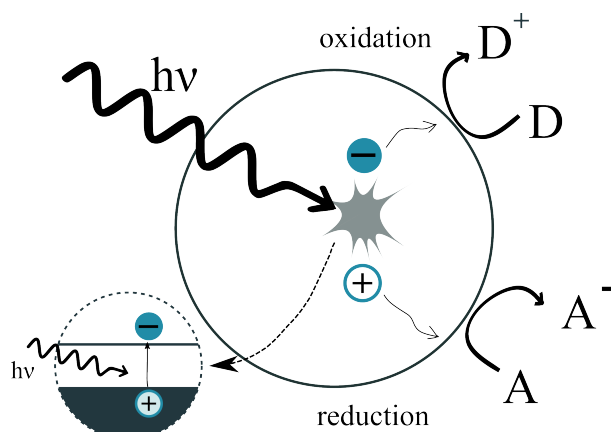


**Figure 3.1:** Mechanism of the heterogeneous photocatalytic process.

oxidation and reduction potentials of the target reactions to enable efficient charge transfer. For example, CB must be negative enough to reduce protons to hydrogen ( $\text{H}_2$ ) or oxygen to superoxide anions ( $\text{O}_2^-$ ), and the valence band must be positive enough to oxidize water to hydroxyl radicals ( $\cdot\text{OH}$ ) or degrade organic pollutants.

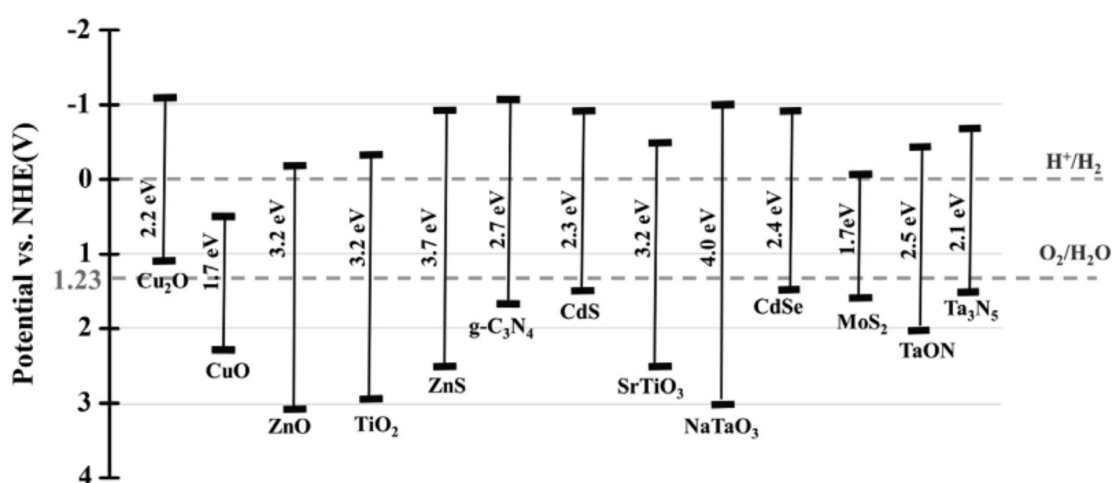


**Figure 3.2:** Positions of VB and CB of various semiconductors relative to the oxidation and reduction potentials of water. Adopted from [73].

The surface characteristics of a photocatalyst also play a significant role in its efficiency. A larger surface area provides more active sites for photocatalytic reactions to occur, and thus increases the overall catalytic activity of the material. Nanostructured semiconductors offer large surface areas and are often employed in photocatalysis to improve efficiency. In addition to surface area, the morphology and crystal structure of the semiconductor influence its catalytic properties. For

instance, defects in the crystal structure can serve as active sites for the adsorption of pollutants or enhance the charge separation efficiency [74].

## 3.2 Zinc Oxide as a Photocatalyst

Zinc oxide has emerged as a promising material for photocatalysis and is attracting a lot of attention due to its unique properties and wide range of applications. It is a II-VI compound semiconductor with a wide, direct band gap ( $\sim 3.3$  eV) and an exciton binding energy of 60 meV [75]. This characteristic enables the formation of excitons even at room temperature and promises good optical properties of the material. In practice, ZnO has proven its high effectiveness in water purification, where it can degrade a variety of organic pollutants, including dyes and pharmaceuticals [7]. Its ability to operate under UV light makes it particularly suitable for water treatment technologies. The photocatalytic properties of ZnO also extend to air purification, as it effectively removes volatile organic compounds from the atmosphere through photocatalytic oxidation processes [76]. Another interesting area is the potential role of ZnO in hydrogen production through photocatalytic water splitting [77], making ZnO a candidate for sustainable energy solutions. In addition, ZnO can be synthesised in a variety of nanostructures [78], such as nanoparticles [79], nanorods [80], thin films [81] each with unique surfaces that significantly affect the photocatalytic performance. The thermal and chemical stability of ZnO also contributes to its attractiveness and enables a wide range of applications without significant decomposition.

In addition to these proven applications, ZnO films exhibit antibacterial activity [82], making them a promising material for applications in the health and hygiene applications. The antibacterial properties of ZnO are based on its ability to generate reactive oxygen species when exposed to light and to release  $\text{Zn}^{2+}$  ions that destroy the cell membranes of bacteria. ZnO coatings can therefore be applied to medical devices, textiles and food packaging to inhibit the growth of microbes and increase safety.

Despite these advantages, the use of ZnO as a photocatalyst is not without its problems. One important limitation is its narrow absorption spectrum, which is mainly in the UV range and limits its effectiveness in visible light. To solve this problem, researchers have explored various strategies, including doping ZnO with metallic or non-metallic elements to increase its light absorption capacity [79, 83]. In addition, the rapid recombination of electron-hole pairs poses a challenge that can affect photocatalytic efficiency. To improve charge separation, approaches

such as the formation of heterojunctions [84] and the integration of cocatalysts are being actively investigated.

ZnO crystallizes in three different forms: rocksalt (NaCl structure), cubic zinc-blende and hexagonal wurtzite. The hexagonal wurtzite structure is the most common and thermodynamically most stable form under ambient conditions, while the rocksalt and zinc-blende structures only form at higher temperatures and pressures. A more detailed discussion of wurtzite ZnO can be found in the section 4.2.1. Thin ZnO films deposited by ALD and PEALD retain the wurtzite crystal structure. The crystallinity and morphology of these films depend on the deposition parameters, which can influence their photocatalytic and optoelectronic properties [85, 86]. Despite its advantageous properties, wurtzitic ZnO has limitations in photocatalysis as it photocorrodes under UV light and is unstable in extreme pH environments (soluble in strong acids and alkalis) [37, 87, 88].

### **3.3 Motivation for the use of thin ZnO films in Photocatalysis**

Although ZnO nanoparticles benefit from a high surface-to-volume ratio, they also face problems such as aggregation, complex recovery processes and potential secondary contamination. In contrast, thin ZnO films provide a stable and reusable photocatalytic platform. They have fewer oxygen defects, which improves charge transport and reduces electron trapping [89]. In addition, studies suggest that despite the higher specific surface area of nanoparticles, factors such as film stability and charge carrier dynamics play a more crucial role in photocatalytic efficiency [89]. Thin films also offer a practical advantage in terms of reusability, as they adhere to the substrates. This eliminates complex separation steps and reduces material losses and operating costs.

A key advantage of thin ZnO films grown by ALD is their ability to coat complex, porous substrates, effectively increasing the surface area available for photocatalysis [90]. This allows thin films to combine their inherent stability with the enhanced photon absorption and pollutant interaction typically associated with nanoparticles. Furthermore, Sarma et al. [89] discussed that thin films can achieve a more negative potential at the conduction band edge, which promotes efficient electron transfer and facilitates the formation of ROS such as superoxide radicals ( $O_2^{\cdot-}$ ). ALD-grown thin ZnO films further optimise charge separation through precise control of thickness and crystallinity.

Another significant advantage of thin films is their role in the formation of heterojunctions. The combination of ZnO with other semiconductors, such as  $TiO_2$  [91, 92] or  $g-C_3N_4$  [93],

improves charge separation and extends the spectral response of ZnO to visible light. ALD enables atomic-level precision in these heterojunctions and optimises interfacial properties to further improve photocatalytic efficiency.

The ability to fine-tune crystal structure using ALD and PEALD allows precise control of photocatalytic properties [85, 86]. Thin films exhibit lower electron-hole recombination rates and improved charge transfer at the interface, leading to enhanced degradation of organic pollutants [89].

This study investigates PEALD-deposited thin ZnO films as photocatalysts and focuses on optimising their structural and electronic properties for maximum degradation efficiency. While the application of these films on porous substrates and the development of heterojunctions are beyond the scope of this work, these areas offer promising directions for future research.

## **3.4 Model Pollutants**

Organic pollutants are of increasing concern as they persist in the environment, can be toxic and are often difficult to degrade. To overcome these challenges, photocatalysis has gained attention as a promising solution. In this chapter, we focus on two important types of organic pollutants, organic dyes and microplastics.

### **3.4.1 Photocatalytic Degradation of Organic Dyes**

Organic dyes are synthetic chemicals that are widely used in the textile, paper and leather industries for dyeing processes. Their extensive use has led to significant discharge into the aquatic environment, where they cause serious ecological and health problems. Even in low concentrations, these dyes are highly visible, cause aesthetic problems and disrupt aquatic ecosystems by blocking sunlight and inhibiting photosynthesis. Many dyes also contain toxic, mutagenic or carcinogenic components that can endanger both the environment and human health [94]. Conventional wastewater treatment methods are often unable to effectively remove these persistent pollutants. In contrast, heterogeneous photocatalysis has shown considerable potential for the degradation of organic dyes, especially those that are resistant to conventional treatment methods.

### Methylene blue

Methylene blue ( $C_{16}H_{18}ClN_3S$ , MB) is a synthetic dye that can be harmful to the environment, especially if it enters aquatic ecosystems.

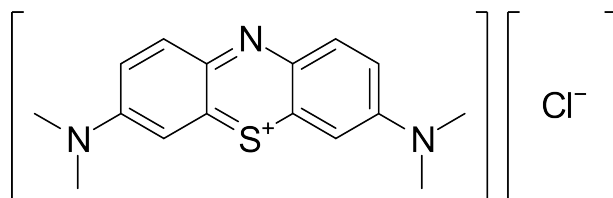


**Figure 3.3:** Structural formula of methylene blue.

MB dissolves easily in water and is not biodegradable [95]. This makes it a persistent pollutant that can have harmful effects on the environment and health. Like many synthetic dyes, MB disrupts photosynthesis by limiting the penetration of sunlight, thereby reducing oxygen solubility and affecting the photosynthetic activity of aquatic flora. In addition, MB can enter the food chain and act as a toxin to aquatic life. In humans, exposure to MB, can lead to a number of health problems such as nausea, vomiting, diarrhea, increased heart rate, etc [95].

Due to its carcinogenic properties and its longevity in the environment, MB requires strict control of its release into natural ecosystems and efficient degradation solutions. The photocatalytic degradation of MB leads to the formation of carbon dioxide, water and various inorganic by-products such as nitrate ( $NO_3^-$ ), sulphate ( $SO_4^{2-}$ ) and chloride ( $Cl^-$ ) ions [95, 96]. Although these inorganic substances are generally considered less harmful than methylene blue itself, it is still important to monitor and control their accumulation in the environment.

In this study, the chemical composition of the treated solution was not analysed and the discussion on MB degradation is based on theoretical assumptions and existing literature.

#### 3.4.2 Photocatalytic Degradation of Microplastic Fibers

Microplastics, defined as plastic particles smaller than 5 mm, have become a widespread environmental pollutant. These particles originate either from the decomposition of larger plastic waste or are intentionally manufactured as microbeads for use in personal care products. Due to their small size, microplastics can be ingested by aquatic organisms, leading to bioaccumulation and ecosystem disruption [97].

Microplastics are generally divided into two categories according to their origin. Primary microplastics are intentionally produced particles that are often found in cosmetics, exfoliants and

industrial abrasives. Secondary microplastics, on the other hand, result from the decomposition of larger plastic items such as bottles, bags and fishing nets, which is caused by environmental factors such as UV radiation, mechanical abrasion and chemical decomposition [98].

Extensive studies have confirmed the presence of microplastics in various waters, including rivers, lakes, oceans and even groundwater [99]. These tiny plastic fragments pose a serious threat to marine life as they are often ingested by organisms ranging from plankton to fish and large marine mammals. Ingestion can lead to physical damage, internal injuries and digestive blockages, which in turn can result in growth disorders, reproductive problems and, in severe cases, death [1, 100]. Microplastics not only cause physical damage, but also act as a carrier for toxic substances such as heavy metals and pesticides by absorbing and concentrating them from the environment [100]. New research has raised concerns about their potential impact on human health, particularly on the reproductive, digestive and respiratory systems. Some studies suggest a possible link to colon and lung cancer [101].

The degradation of microplastics poses a major challenge due to their chemical resistance and slow decomposition in nature. Conventional removal methods, such as mechanical or thermal treatments, are energy-intensive and can lead to secondary pollution. However, photocatalysis has proven to be a promising alternative, as it promotes the oxidative degradation of plastic polymers when exposed to light and thus represents a potential solution to microplastic pollution [84, 102, 103, 104].

### Polyethylene terephthalate

Polyethylene terephthalate (PET) is a widely used thermoplastic polymer that is mainly used in the packaging and textile industries [105]. Although polyesters offer numerous advantages in everyday products, their widespread use has led to significant environmental problems. Unlike organic dyes, polyesters do not dissolve easily in water but break down into smaller particles over time [106].

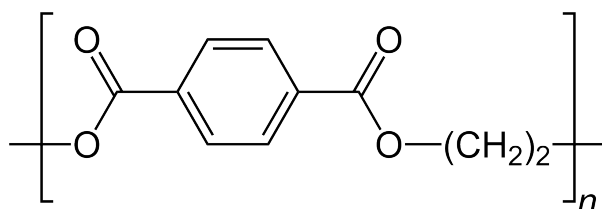


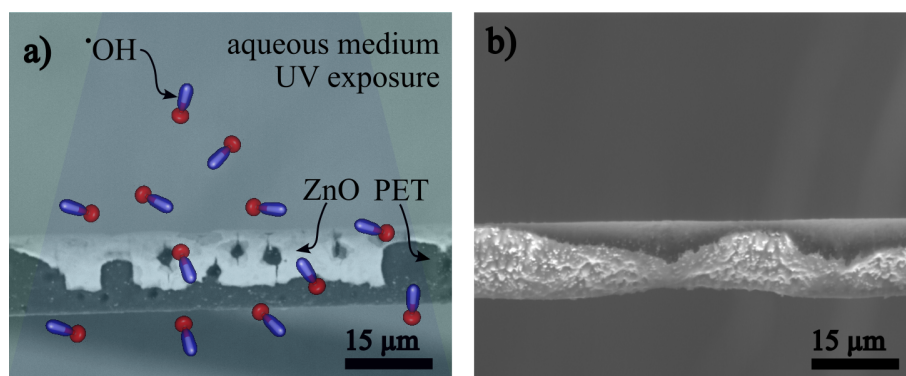
**Figure 3.4:** Chemical structure of polyethylene terephthalate.

The chemical structure of PET (Fig. 3.4), which consists of aromatic rings and ester bonds, ensures high stability so that it remains in landfills, oceans and other ecosystems [107, 108]. To address these issues, various remediation strategies have been explored. Physical and chemical methods such as incineration, pyrolysis, and hydrolysis can degrade PET, but often generate toxic by-products and greenhouse gases [108]. Biological treatments, including microbial degradation, offer a more sustainable approach, although they are currently less efficient and slower than conventional methods [108, 109]. Among emerging solutions, photocatalytic degradation (using heterogeneous catalysts under light irradiation) shows promise for breaking down PET into smaller, less harmful molecules [110, 111, 112].

The chemical formula of PET is  $(C_{10}H_8O_4)_n$  and its photodegradation primarily targets the ester bonds ( $-COO-$ ) within the polymer chain:

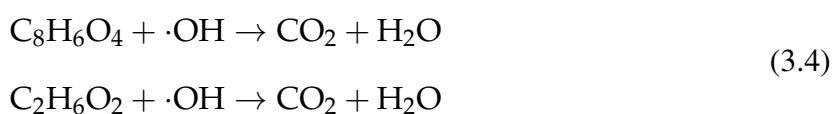


Figure 3.5 shows an illustrated process of photodegradation of PET fibre.



**Figure 3.5:** a) Schematic representation of the degradation process of PET microfibrils under UV exposure. b) Fibre after degradation.

The main degradation products of PET are carboxylic acids (e.g. terephthalic acid,  $C_8H_6O_4$ ), alcohols (e.g. ethylene glycol,  $C_2H_6O_2$ ), aldehydes, esters and olefins [113]. Over time, further oxidation leads to complete mineralization yielding carbon dioxide and water [113]:



In this dissertation, the degradation products of PET were not analysed experimentally. The discussion of degradation pathways and mineralisation is based on theoretical assumptions and previous research results. Further experimental studies are required to confirm these degradation processes and to evaluate the efficiency of photocatalysis under real conditions.

## Chapter 4

# Materials and Methods

This chapter gives a brief overview of the main experimental characterisation methods used in this thesis. Since the basic principles of plasma-enhanced atomic layer deposition, the synthesis technique that is the focus of attention, are explained in Section 2.1, the first section concentrates on the presentation of the most important deposition parameters. The second section contains a summary of all characterisation techniques and a brief explanation of their underlying principles. Finally, the last section describes the method used to evaluate the photocatalytic activity of the synthesised films.

### 4.1 Synthesis of thin ZnO films with ALD and PEALD

Thin ZnO films were deposited using a Beneq TFS 200 ALD system. The films were mainly produced using PEALD, with DEZ and oxygen plasma serving as zinc and oxygen precursors, respectively. For comparison, some films were deposited using the thermal ALD technique, where DEZ and H<sub>2</sub>O were used as precursors. High purity nitrogen was used for all purging processes (purity 6.0). For all PEALD processes, the capacitively coupled plasma source was operated in remote configuration with a frequency of 13.56 MHz.

All samples were grouped into four categories based on their synthesis parameters:

#### 1. ZnO films deposited at fixed temperature

Thin ZnO films were deposited at a fixed temperature of 80 °C using either the PEALD or the ALD technique. In the PEALD method, each growth cycle consisted of a 250 ms DEZ pulse followed by a 1.25 s nitrogen purge, a 3 s oxygen plasma exposure with an RF power of 150 W and a 6 s nitrogen purge. In the thermal ALD process, the deposition

cycle included a 200 ms DEZ pulse, a 1 s nitrogen purge, a 180 ms exposure to H<sub>2</sub>O and another 1 s nitrogen purge.

## 2. ZnO films deposited at fixed plasma RF power at different temperatures

Thin ZnO films were deposited using PEALD at different temperatures between 60 °C and 250 °C with a fixed RF power of 50 W. The growth cycles corresponded to those described in 1: 250 ms DEZ pulse, 1.25 s nitrogen purge, 3 s oxygen plasma exposure and 6 s nitrogen purge.

## 3. ZnO films deposited at room temperature and variable plasma RF power

The ZnO films were deposited using PEALD at room temperature while the RF power varied between 50 W and 250 W. The deposition process was carried out using similar growth cycle parameters as in 1. and 2., with a 250 ms DEZ pulse, a 2.5 s nitrogen purge, a 3 s oxygen plasma exposure and a 12 s nitrogen purge.

## 4. ZnO films deposited for photodegradation of microplastics

ZnO films developed for the degradation of microplastics were deposited at 80 °C and RF power set to 50 W and at room temperature with an RF power of 250 W using PEALD. The growth cycles were the same to those in 3.

The substrates used for the first three types of deposition were glass slides (for photocatalytic activity measurements), fused silica wafers (for optical measurements) and silicon wafers (for HRTEM, XPS, XRD, SEM, EDS and SIMS characterisations). PET microfibrils were the substrates for the last group of samples. Further details on the PET substrates used can be found in the section 4.3.2.

## 4.2 Thin Film Characterization Techniques

### 4.2.1 X-ray Diffraction

X-ray diffraction (XRD) is a widely used technique for analysing the structure of crystalline materials. It provides detailed information about the arrangement of atoms in a material, including lattice parameters, crystallite size, phase determination and crystallite orientation. In X-ray diffraction, a monochromatic X-ray beam is directed at a crystal, which causes the atoms in the crystal lattice to scatter the X-rays in certain directions through constructive and destructive

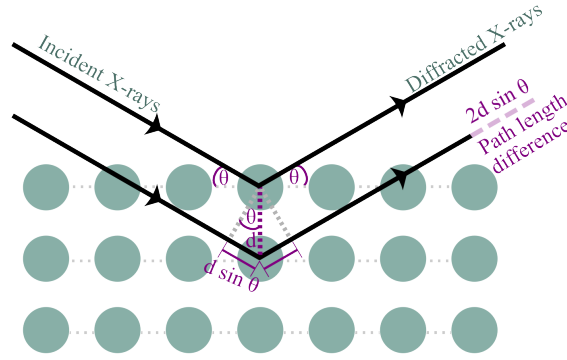


**Figure 4.1:** Schematic illustration of X-ray diffraction.

interference. This happens because the X-rays are reflected from different lattice planes. The condition for constructive interference is described by Bragg's law:

$$n\lambda = 2d \sin \theta \quad (4.1)$$

where  $n$  is the diffraction order ( $n = 1, 2, 3 \dots$ ),  $\lambda$  is the wavelength of the incident X-rays,  $d$  is the distance between the planes and  $\theta$  is angle of diffraction. This technique is non-destructive and is suitable for the investigation of bulk and thin-film materials. However, it is only suitable for crystalline materials. Amorphous materials or those with low crystallinity do not produce useful diffraction patterns. For complex and multiphase materials, the diffraction peaks can overlap, making it difficult to identify and quantify the individual phases by minimizing the diffraction signal from the substrate. In addition, relatively large and homogeneous samples are required to obtain reliable data. For the analysis of thin films and coatings, a variant of X-ray diffraction is used in which the X-ray beam only penetrates the thin surface layer, the so-called grazing incidence X-ray diffraction (GIXRD).

As previously mentioned, ZnO deposited by ALD and PEALD exhibit wurtzite structure. The hexagonal unit cell of wurtzite is defined by two lattice parameters,  $a$  and  $c$ . In an ideal wurtzite structure, the ratio is  $c/a = \sqrt{8/3}$ . The structure consists of two overlapping hexagonal, close-packed sublattices, whereby in an ideal wurtzite structure one sublattice is shifted by  $3/8$  in relation to the other. The positions of the atoms in the unit cell for an ideal wurtzite structure are  $(0, 0, 0)$  and  $(2/3, 1/3, 1/2)$  for the first type of atom and  $(0, 0, 3/8)$  and  $(2/3, 1/3, 7/8)$  for the second type of atom. According to Kittel [114], the structure factor  $S(hkl)$  is defined as:

$$S(hkl) = \sum_j f_j e^{2\pi i(hx_j + ky_j + lz_j)} \quad (4.2)$$

where  $f_j$  is the atomic scattering factor of the  $j$ th atom and  $(x_j, y_j, z_j)$  are the fractional coordinates of the atom in the unit cell. For ZnO, this expression can be expanded as follows:

$$S(hkl) = f_{\text{ZnO}} \left( 1 + e^{2\pi i \left( \frac{2}{3}h + \frac{1}{3}k + \frac{1}{2}l \right)} \right) + f_{\text{O}} \left( e^{\pi i \frac{3}{4}l} + e^{2\pi i \left( \frac{2}{3}h + \frac{1}{3}k + \frac{7}{8}l \right)} \right). \quad (4.3)$$

This can be further simplified to:

$$S(hkl) = \left( f_{\text{ZnO}} + f_{\text{O}} e^{\pi i \frac{3}{4}l} \right) \left( 1 + e^{2\pi i \left( \frac{2}{3}h + \frac{1}{3}k + \frac{1}{2}l \right)} \right). \quad (4.4)$$

From the equation 4.4 it follows that the reflections in the diffractogram disappear if  $2h + 4k + 3l = 3p$ , where  $p$  is an odd integer [115]. Examples of permitted reflections are (100), (002), (101), (102), (110), (103), (112). Forbidden reflections, on the other hand, are: (001), (111), (201). The orientation of some of the allowed planes, in particular (002), (101) and (100), is shown in Figure 4.2.

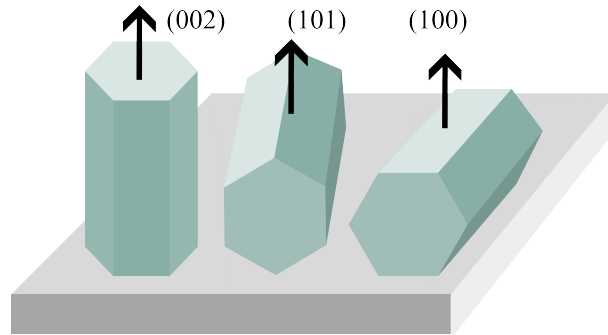


**Figure 4.2:** The orientation of the (002), (101) and (100) planes in ZnO films grown on a glass substrate. Adapted from [116].

For ZnO in its wurtzite form, the experimentally determined lattice parameters are  $a = 3.25 \text{ \AA}$  and  $c = 5.207 \text{ \AA}$ , i.e.  $c/a = 1.602$  and an internal parameter  $u = 0.345$ , which indicates a slight deviation from the ideal atomic positions [117].

For this dissertation, the measurements were performed with a GIXRD diffractometer equipped with a cobalt (Co) X-ray tube and a tungsten/carbon (W/C) multilayer for beam shaping and monochromatization (Siemens D5000). The diffraction spectra were recorded with a curved

position-sensitive detector (RADICON) located 120 mm from the sample. The GIXRD measurements were performed at a fixed grazing incidence angle of  $\alpha_i = 1^\circ$  to ensure that the X-ray penetration depth covered the entire thickness of the ZnO films.

X-ray reflectivity (XRR) was used to determine the thickness and average density of the ZnO films. The XRR measurements were performed with the same diffractometer as the GIXRD measurements, but with a different detector (Hecus PSD-50M) located 500 mm from the sample. In the XRR measurements, a series of diffuse scattering spectra were recorded over an angle of incidence  $\alpha_i$  from  $0^\circ$  to  $2.5^\circ$  with a step size of  $0.003^\circ$ . The intensity of the specular reflection was determined from these measurements, corrected for the background and the diffuse scattering components.

### 4.2.2 High-Resolution Transmission Electron Microscopy

High-resolution transmission electron microscopy (HR-TEM) is a powerful technique that provides images with atomic resolution and enables the direct visualisation of individual atoms, crystal lattice defects, grain boundaries and dislocations. In addition to imaging in real space, HR-TEM also enables diffraction analysis by selected area electron diffraction (SAED) or fast Fourier transform (FFT) of lattice images. This diffraction capability provides detailed crystallographic information such as lattice parameters, crystal size, orientation and phase identification. In combination with techniques such as energy dispersive X-ray spectroscopy, HR-TEM can provide localised data on elemental composition at the nanoscale. This technique is suitable for a wide range of materials, including metals, semiconductors, ceramics, polymers and biological samples. We have used it to determine the crystal structure in a cross-section of a thin ZnO film.

The TEM images were recorded with the Jeol JEM 2100 device at an applied voltage of 200 kV. The FFT analyses were performed with the Gatan Micrograph software.

HR-TEM cross-sectional analysis (like any other TEM analysis) requires extremely thin samples (less than 100 nm thick), which can be difficult to prepare. We used a conventional method to prepare thin films, which involves four main steps: sample cutting, mechanical thinning, dimpling and ion milling (Fig. 4.3). First, the sample was cut into rectangles of  $1.8 \text{ mm} \times 2 \text{ mm}$  with a diamond saw. Then two sample pieces were bonded together with a two-component resin to form a "sandwich", with the film-covered surfaces facing each other.

The glued "sandwich" was then inserted into a brass ring, fixed with pieces of Si and filled with resin. After curing at  $130^\circ \text{C}$ , the sample is ready for the second step, mechanical thinning,

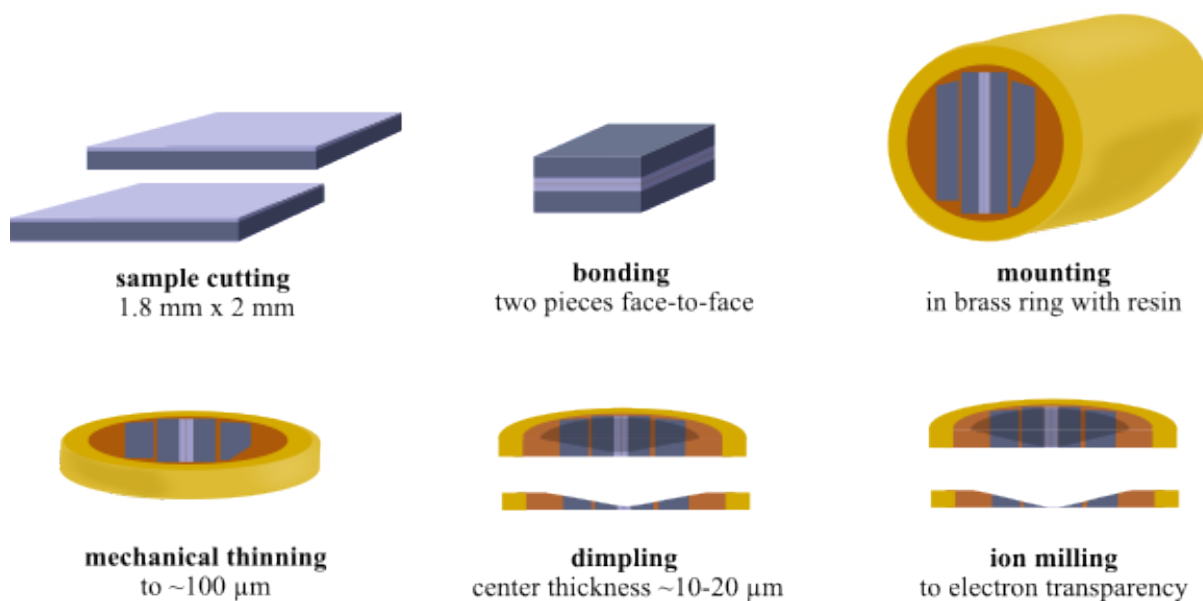


**Figure 4.3:** Preparation of thin films for cross-sectional TEM analysis.

where abrasive papers with different gradations were used to obtain a sample of about 100  $\mu\text{m}$  thickness.

Although a thickness of 100  $\mu\text{m}$  is not sufficient to analyse the structure of the film, further mechanical thinning would damage the sample. Therefore, in the third step, we thinned the sample only in the centre with a "dimple grinder" and created a 20  $\mu\text{m}$  thick dimple in which the film (the area of interest) is located. The sample is then carefully milled at a shallow angle using the precision ion polishing system (PIPS II, Gatan) with a high-energy argon beam (energy 3.5 keV) until a small hole is created in the centre. Once the sample is sufficiently thin, we switch to a lower energy ion beam (energy 1.5 keV) to polish the surfaces and remove amorphous layers that were created during the first milling. This step is important to improve the quality of the HR-TEM images. At this point, the sample next to the hole is only a few nanometres thick so that the electrons can tunnel. Before the TEM analysis, the sample was coated with a thin layer of carbon to prevent charging under the high-energy electron beam.

An alternative method for preparing thin films for TEM imaging is the use of a focused ion beam (FIB). Conventional FIB uses a finely focused gallium ion beam to selectively mill a specific area, often with micron-level precision. This technique is well suited for targeted sample preparation, e.g. to localise a specific defect or interface in a component. In this work, the FIB was not used to prepare samples for TEM analysis, but to cut the microplastic fibre and analyse its cross-section with the SEM.

### 4.2.3 Scanning Electron Microscopy

Scanning electron microscopy (SEM) is an important technique for characterising materials. It provides high-resolution images of the surface of a material and is frequently used in scientific and industrial applications. In SEM, a focused electron beam is scanned across the surface of the sample. When the electron beam interacts with the sample, it generates various signals, including secondary electrons, backscattered electrons and X-rays (Fig. 4.4). The most frequently detected

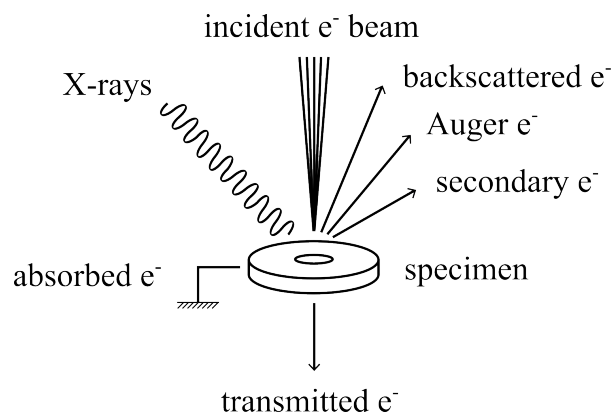


**Figure 4.4:** In the SEM, the incident electron beam interacts with the sample surface and causes the emission of secondary electrons, backscattered electrons, characteristic X-rays and, if sufficiently thin, transmitted electrons. Adopted from [118].

signal in the SEM are secondary electrons, which are emitted by atoms near the surface through inelastic scattering of the incident electrons. A detector collects these secondary electrons and their intensity is used to generate an image showing the surface topography of the sample. Backscattered electrons, which are the result of elastic scattering, can also be detected. Heavier elements that backscatter electrons more efficiently appear brighter in the SEM image and provide a contrast based on atomic number. This feature is often used when differences in the composition of heterogeneous samples are to be observed. In this work, for example, it was used to measure the thickness of thin films in cross-section and to detect ZnO residues on polymer fibres. In addition, the SEM can be equipped with a detector for energy dispersive X-ray spectroscopy (EDS) to analyse the elemental composition of the sample and obtain both qualitative and quantitative data on the investigated materials.

Sample preparation is much simpler than for TEM imaging. Firstly, the sample must be clean and dry. In addition, the samples must be electrically conductive so that they do not become charged under the electron beam. The sample is attached to a holder with a conductive adhesive to ensure good electrical contact between the sample and the holder. Non-conductive samples

are usually coated with a thin layer of conductive material such as gold, platinum or carbon to improve electron conduction. The resulting SEM image provides information about the surface topography of the sample with high resolution and depth of field. Image contrast and resolution can be optimised by adjusting the acceleration voltage, working distance and probe current. The acceleration voltage influences the beam penetration and signal generation. The working distance influences the depth of field and image sharpness. The probe current determines the number of electrons that hit the sample, which has an effect on the brightness and the signal-to-noise ratio. For thin films, a deceleration mode (gentle beam) is often used, in which the incident electrons are decelerated shortly before hitting the sample. This is achieved by applying a negative bias voltage to the stage. As a result, the beam penetrates the sample less and consequently the interaction volume and charge are reduced.

The EDS detector is used to analyse the composition. It collects and analyses the characteristic X-rays emitted by the sample when the electron beam excites the atoms. This process allows the elements in the sample to be identified and quantified, providing valuable information about its composition.

The scanning electron microscope has some limitations. It requires high vacuum conditions, which make it unsuitable for imaging wet samples. Another limitation of the SEM is the high electron energy, which can cause damage when imaging sensitive materials. Non-conductive samples require additional preparation to prevent the high-energy electrons from causing a charging effect that leads to image distortion or artifacts. To overcome these limitations, the environmental SEM (eSEM) was developed, which allows imaging of wet or hydrated samples without high vacuum and also reduces the charging of non-conductive samples. However, the eSEM has a lower resolution than the normal SEM. In this work, the eSEM was used to image microplastic fibers.

In this work, the JEOL JSM-7800F field emission SEM and the Thermo Fisher Quanta 650 eSEM were used to visualise the samples. The JEOL JSM-7800F is a field emission SEM with a maximum resolution of 0.8 nm and an accelerating voltage of 0.01 – 30 kV. It is equipped with the following detectors: lower secondary electron detector (LED), upper secondary electron detector (UED), backscattered electron detector (BED), scanning transmission electron microscopy detector (STEM), energy dispersive X-ray spectrometer (X Max 80, Oxford Instruments).

The Thermo Fisher Quanta 650 eSEM is equipped with a thermionic tungsten (W) electron source and offers a maximum resolution of 3.0 nm at 30 kV. The accelerating voltage can be adjusted

from 0.2 to 30 kV. This instrument features a differential pumping system that allows operation in three vacuum modes: high vacuum (HiVac), low vacuum (LoVac) and environmental SEM (eSEM). The Quanta 650 eSEM is equipped with a large-field secondary electron detector (LFD), a coherent backscattered electron detector (CBS) and a gaseous secondary electron detector (GSED) for eSEM mode. It is also equipped with an energy dispersive X-ray spectrometer (EDS) for elemental analysis.

The particle size distribution was determined with the ImageJ programme using the "Analyse particles" function after filtration and setting the threshold values.

#### 4.2.4 X-ray Photoelectron Spectroscopy

X-ray photoelectron spectroscopy (XPS) is a highly sensitive, non-destructive method for determining the chemical composition of surfaces. It is ideal for the investigation of surface modifications, thin films, surface contamination, etc. In this technique, a sample is irradiated with monoenergetic X-rays to excite electrons from bound states in atoms into unbound vacuum states (Fig. 4.5).

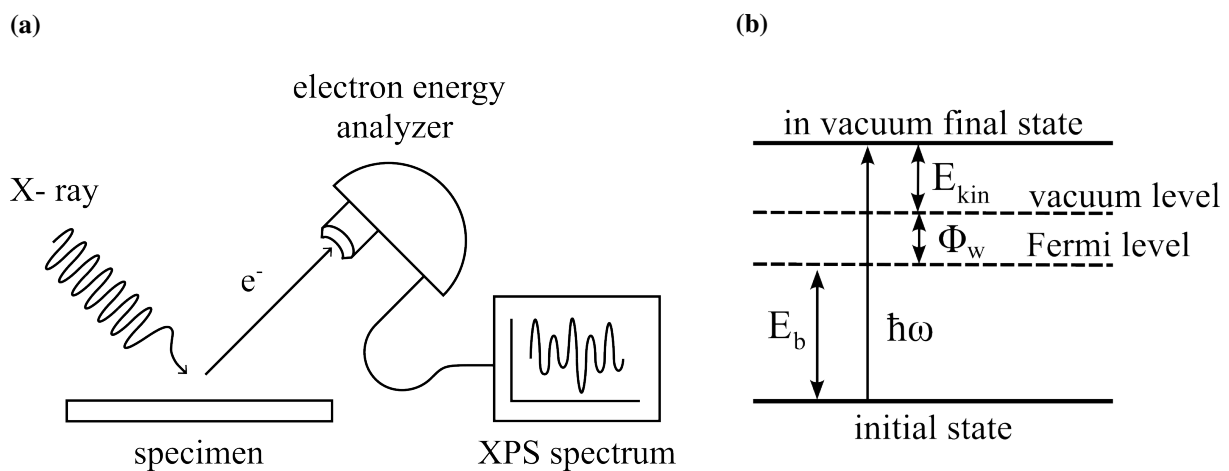


**Figure 4.5:** a) Schematic representation of the XPS process. Adopted from [118].  
b) Photoemission process. Adopted from [119].

The kinetic energy ( $E_{kin}$ ) of the emitted photoelectrons is determined by the following equation (Fig. 4.5):

$$E_{kin} = \hbar\omega - E_b - \Phi_w \quad (4.5)$$

where  $\hbar\omega$  is the energy of an incident photon,  $E_b$  is the binding energy with respect to the Fermi level and  $\Phi_w$  is the work function of the material. The kinetic energy is measured in the electron energy analyser, which is one of the main components of the XPS spectrometer.

Because the kinetic energy of an electron depends on the energy of the incident photon, the binding energy is a more valuable quantity, as it provides information about the elemental composition and atomic state from which the photoelectron originates. Hence, the XPS spectra usually represents the number of electrons as a function of their binding energy. Since the binding energy of the electrons changes slightly depending on the chemical environment of the emitting atom, this technique provides information about the chemical states of the atoms.

Photoelectrons that leave the material without energy loss contribute to characteristic peaks in the spectra and are emitted from the surface of the material (only a few atomic layers). Photoelectrons that are ejected from greater depths are scattered and contribute to the background signal in the spectrum. For this reason, XPS is considered a surface technique, where the uppermost 70 Å of a material is examined.

For homogeneous samples, the intensity of the photoemission peak is equal to

$$I = n f \sigma \theta y \lambda A T, \quad (4.6)$$

where  $n$  is the number of atoms of the element per unit volume,  $f$  is the X-ray flux,  $\sigma$  is the photoemission cross section for the atomic orbital of interest,  $\theta$  is an angular efficiency factor for the instrumental setup which depends on the angle between the photon trajectory and the detected electron,  $y$  is the efficiency of the photoemission process for the formation of photoelectrons with normal photoelectron energy,  $\lambda$  is the mean free path of the photoelectrons in the sample,  $A$  is the area of the sample from which photoelectrons are detected, and  $T$  is the detection efficiency for electrons emitted from the sample [120, 121].

The concentration of atoms can then be written as:

$$n = \frac{I}{S}, \quad (4.7)$$

where  $S$  is the atomic sensitivity factor for a given atomic orbital,  $S = f \sigma \theta y \lambda A T$ . Therefore, we can express the relative concentration of two elements as follows:

$$\frac{n_1}{n_2} = \frac{I_1/S_1}{I_2/S_2}. \quad (4.8)$$

Since the relative values  $S_1/S_2$  are constant for each spectrometer, the expression 4.8 in the case of ZnO can be written as follows:

$$\frac{n_{\text{Zn}}}{n_{\text{O}}} = \frac{I_{\text{Zn}}}{I_{\text{O}}} S_{\text{O/Zn}}, \quad S_{\text{O/Zn}} = \frac{S_{\text{O}}}{S_{\text{Zn}}} = \text{const. (for a given spectrometer)}. \quad (4.9)$$

In our measurements, we have considered the intensities of O 1s and Zn 2p<sub>3/2</sub> XPS lines ( $I_{\text{O}}$  and  $I_{\text{Zn}}$  respectively), and areas under the O 1s and Zn 2p<sub>3/2</sub> experimental curves were calculated using the program *CasaXPS* with Shirley background subtraction. The calculations were repeated at four different intervals around each peak and then the average was calculated.

The relative atomic sensitivity factor for given elements can be determined using empirically derived atomic sensitivity factors, but in our case we determined the relative atomic sensitivity factor  $S_{\text{O/Zn}}$  from the measurement taken on the single crystal ZnO, for which

$$n_{\text{Zn, mono}} = n_{\text{O, sc}} \Rightarrow S_{\text{O/Zn}} = \frac{I_{\text{O, sc}}}{I_{\text{Zn, sc}}}. \quad (4.10)$$

In this dissertation, photoemission spectra were recorded with a SPECS type spectrometer equipped with a monochromatic Al – K<sub>α</sub> X-ray source of 1486.74 eV and a Phoibos MCD 100 electron analyser. High resolution scans were recorded with a pass energy of 10 eV and an energy step of 0.05 eV. To remove adventitious carbon and other residual adsorbents on the surface, 15 min - 30 min sputtering was performed with 1 keV Ar<sup>+</sup> ions in the XPS chamber. For all samples, measurements were performed before and after sputtering to ensure that all carbon atoms were removed. All measurements were performed at room temperature. The selected photoemission spectra were deconvoluted with the product of Gaussian and Lorentzian functions and the Shirley background subtraction, using the UNIFIT program.

#### 4.2.5 UV-Vis Spectroscopy

UV-Vis spectroscopy is a method of absorption spectroscopy in the ultraviolet and visible range of the electromagnetic spectrum.

The method measures the intensity of the light that passes through a sample ( $I$ ) and compares it with the intensity of the light before it passes through the sample ( $I_0$ ). The transmittance  $T$  is defined as:

$$T = \frac{I}{I_0}. \quad (4.11)$$

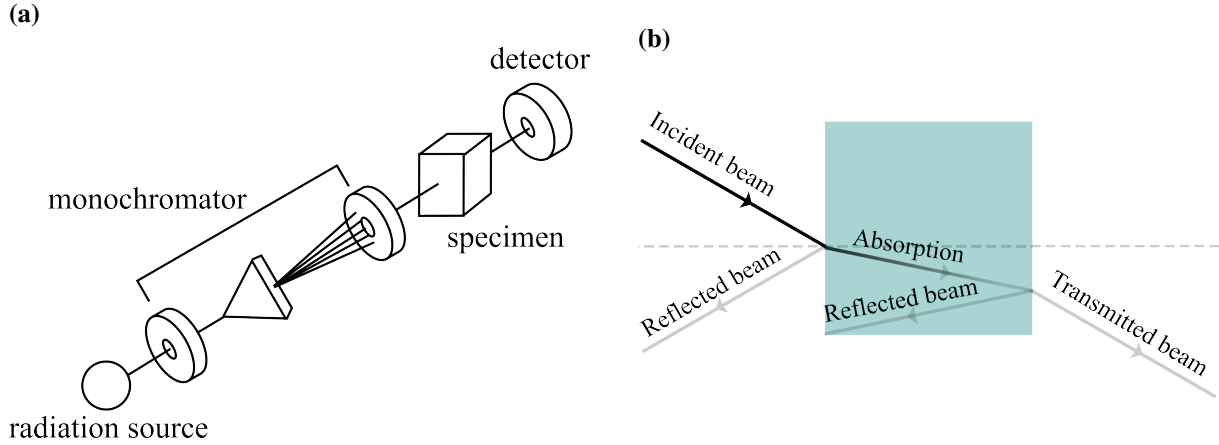


**Figure 4.6:** a) Schematic representation of UV-Vis spectrophotometer. Adopted from [118]. b) Reflection, absorption and transmission of the incident beam.

The absorption  $A$  is linked to the transmittance:

$$A = -\log_{10} T = -\log_{10} \left( \frac{I}{I_0} \right). \quad (4.12)$$

The absorption is specified as a function of the wavelength. The absorption depends on the optical properties and the thickness of the material and is described by the Beer-Lambert law:

$$A = \alpha \cdot d \cdot c, \quad (4.13)$$

where  $\alpha$  is the absorption coefficient,  $d$  is the sample thickness and  $c$  is the concentration of the absorbing species. UV-Vis spectroscopy is often used to determine the band gap energy of semiconductors. By plotting the absorbance or the square root of the absorbance against the photon energy, the band gap energy can be extrapolated.

In semiconductors with a direct band gap (Fig. 4.7a), the conduction band minimum and the valence band maximum occur with the same momentum  $\vec{k}$ . This enables efficient absorption and emission of photons, as an electron can transition directly between the conduction and valence bands without changing its momentum. The absorption coefficient  $\alpha$  for direct semiconductors is typically described by:

$$\alpha \hbar\omega \propto \sqrt{\hbar\omega - E_g} \quad (4.14)$$

where  $\hbar\omega$  is the photon energy and  $E_g$  is the band gap energy of the semiconductor.

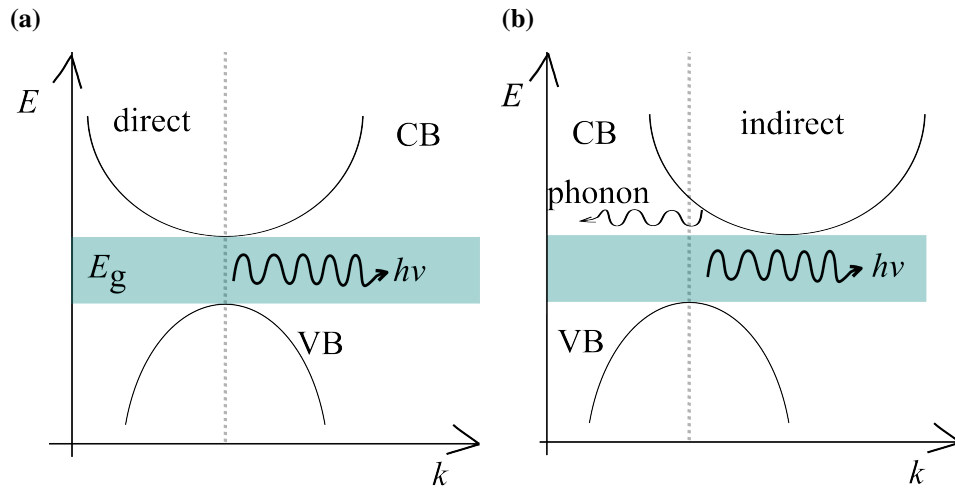


**Figure 4.7:** Positions of the valence band and the conduction band as a function of momentum ( $k$ ) for (a) direct and (b) indirect bandgap semiconductors.

This relationship shows that the absorption coefficient increases as the photon energy approaches the band gap energy. At photon energies above the band gap, the absorption coefficient  $\alpha$  increases rapidly due to the density of states in the conduction band, which allows a large number of transitions.

The square of the absorption coefficient is proportional to the difference between the photon energy and the band gap energy:

$$(\alpha\hbar\omega)^2 \propto \hbar\omega - E_g \quad (4.15)$$

This quadratic dependence is characteristic of semiconductors with a direct band gap and is used to determine the band gap energy from absorption spectra. A Tauc plot in which  $(\alpha\hbar\omega)^2$  is plotted against  $\hbar\omega$  results in a straight line, and the band gap  $E_g$  can be determined from the intersection of this line with the photon energy axis.

In semiconductors with an indirect band gap (Fig. 4.7b), the conduction band minimum and the valence band maximum occur at different momenta. Thus, for an electron to transition between these bands, it must also include a phonon to conserve momentum. This makes the absorption process less efficient compared to direct semiconductors.

The energy required for an electron to transition from the valence band to the conduction band in an indirect semiconductor contains the energy of a phonon  $\hbar\omega_{\text{phonon}}$ . The photon energy  $\hbar\omega$

must therefore correspond to the sum of the band gap energy  $E_g$  and the phonon energy:

$$\hbar\omega = E_c - E_v \pm \hbar\omega_{\text{phonon}} \quad (4.16)$$

where  $E_c$  is the conduction band edge,  $E_v$  is the valence band edge and  $\hbar\omega_{\text{phonon}}$  is the energy of the phonon involved.

The absorption coefficient can be approximated by:

$$\alpha\hbar\omega \propto (\hbar\omega \pm \hbar\omega_{\text{phonon}} - E_g)^2 \quad (4.17)$$

For indirect semiconductors, the  $\sqrt{\alpha\hbar\omega}$  plot against  $\hbar\omega$  provides information on the bandgap  $E_g$  and the phonon energy  $\hbar\omega_{\text{phonon}}$ . This quadratic dependence reflects the requirement of phonon involvement for electronic transitions.

#### 4.2.6 Secondary Ion Mass Spectrometry

Secondary ion mass spectrometry (SIMS) is a highly sensitive analysis technique that enables the precise elemental characterisation of solid materials by bombarding a sample with a focused primary ion beam and analysing the emitted secondary ions using mass spectrometry. This technique is frequently used for depth profile analysis of solid materials.

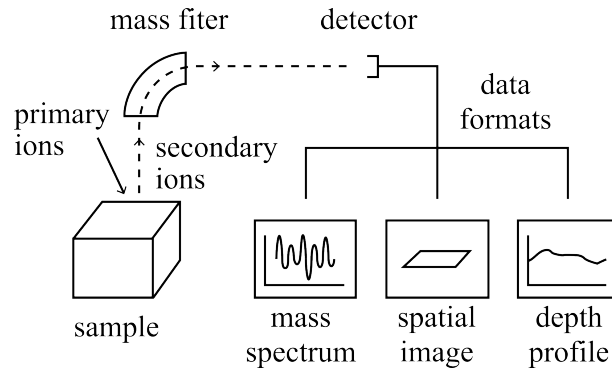


**Figure 4.8:** Schematic representation of SIMS spectrometer. Adopted from [118].

With this technique, all elements of the periodic table and their combinations can be detected with a spatial resolution of a few  $\mu\text{m}$  and a depth resolution of a few nm, requiring only minimal sample preparation [122]. However, quantification of the recorded signals is often challenging as the intensity of SIMS signal highly depends on the substrate and experimental conditions

[122]. Primary ions such as  $O_2^+$ ,  $Ar^+$  or  $Cs^+$  are used to bombard the sample surface and the sputtering process leads to the emission of secondary ions, which are subsequently analysed using a mass filter. The instrument used in this work, manufactured by the company Hiden, is equipped with a quadrupole mass analyser. The analyser consists of four closely spaced rods whose axes are aligned parallel to the original ion trajectory. RF and DC voltages are applied to opposing pairs of rods and by tuning these voltages, only ions with a certain mass-to-charge ratio ( $m/q$ ) can pass through the filter.

### 4.2.7 Photoluminescence Spectroscopy

Photoluminescence spectroscopy (PL) is a widely used technique for analysing the optical and electronic properties of materials, especially semiconductors, nanomaterials and organic compounds. In case of semiconductors, this technique is particularly used for the evaluation of band structure, defect states, recombination dynamics of charge carriers and impurity levels. When a semiconductor is irradiated with light of sufficient energy, photons are absorbed by the material, causing electrons to be excited from the valence band into the conduction band. This process leaves holes, that form electron-hole pairs or excitons. When these excited charge carriers fall back to lower energy states, they can recombine through radiation and emit photons. A typical setup includes a light source to excite the sample, wavelength selectors (filters or monochromators) to isolate specific excitation and emission wavelengths, and a detector positioned at right angles to the excitation beam to reduce background noise from scattered light [123].

When analysing ZnO, two main areas in the PL spectra are typically observed: the NBE emission (near band edge) and the green emission (Fig. 4.9). The NBE emission is the result of excitonic recombination and the energy of this photon is very close to the bandgap energy. Green emission, on the other hand, is due to defects in the material, such as oxygen vacancies or zinc interstitials and occurs in the broad visible spectrum, usually at 500 nm (2.5 eV).

## 4.3 Photocatalytic Activity Testing

### 4.3.1 Testing on Methylene Blue

The photocatalytic activity is often tested using organic dye as a testing agent. One of the most widely used dyes is methylene blue (MB) because of its high stability, low toxicity at low concentrations and affordability. Additionally, methylene blue is frequently present in

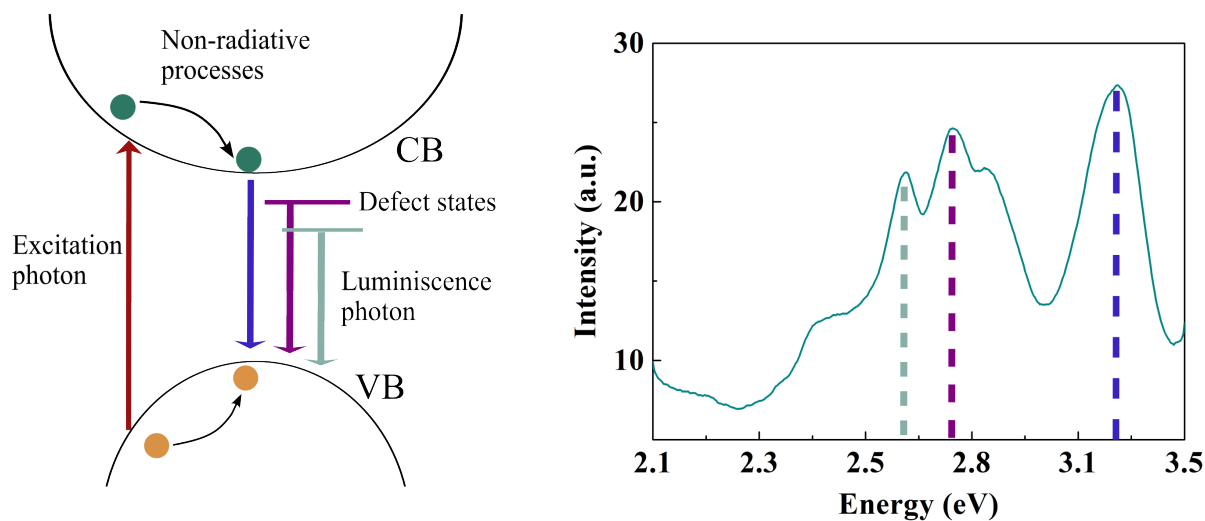


**Figure 4.9:** Schematic illustration (left) and measured PL spectrum (right) of ZnO.

wastewater and its photodegradation is well studied, making it a good reference for comparing the performance of different photocatalysts.

In our experiment, thin films of ZnO deposited on a glass substrate were illuminated for 16 hours before being immersed in a solution of MB in distilled water. This preliminary step was intended to disinfect the surface, increase hydrophilicity and activate the photocatalyst [124]. Following this, the sample with the ZnO film was immersed into the MB solution and illuminated for 7 hours. For illumination, a UVC light source (OSRAM Puritec HNS 6 W G5) was primarily used, although UVA light (OSRAM Supratec 18 W/73) and sun-simulating light (OSRAM Vitalux Ultra 300 W) were also used in some testings. During 7-hour illumination period, the decay of MB concentration was monitored by measuring the optical absorption of MB at 664 nm at consistent time intervals of 60 minutes (Fig. 4.11). Two additional peaks at 246 nm and 292 nm were not used to calculate the photodegradation rate, but their gradual decrease was observed qualitatively and served as evidence for MB mineralisation.

The relationship between concentration and absorption was described by Beer-Lambert (Eq. 4.13). The concentration curve followed the pseudo-first-order kinetics and can be described by the following equation

$$C(t) = C(0) \exp(-kt) \quad (4.18)$$

where  $C(t)$  is concentration at time  $t$ ,  $C(0)$  is the initial dye concentration,  $k$  is photodegradation rate and  $t$  is exposure time to UV light. To determine the rate  $k$ , we linearise the equation by

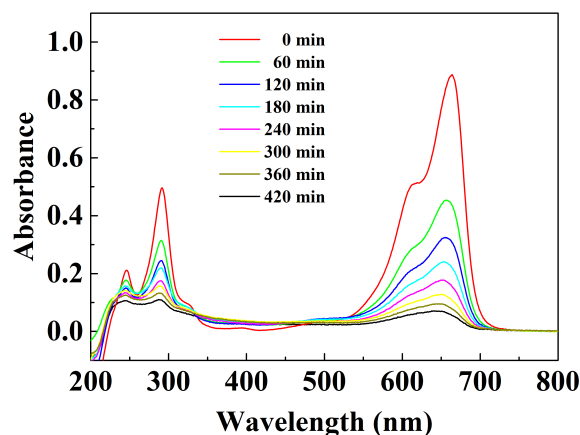


**Figure 4.10:** Time-dependent UV-Vis absorption spectra of MB during photocatalytic degradation under illumination in the range of 200–800 nm.

taking the natural logarithm.

$$\ln \left( \frac{C(t)}{C(0)} \right) = -kt \quad (4.19)$$

Plotting  $\ln \left( \frac{C(t)}{C(0)} \right)$  against  $t$  on a semi-logarithmic graph yields a straight line, with the slope corresponding to  $-k$ . This method allows the rate constant to be extracted from the experimental

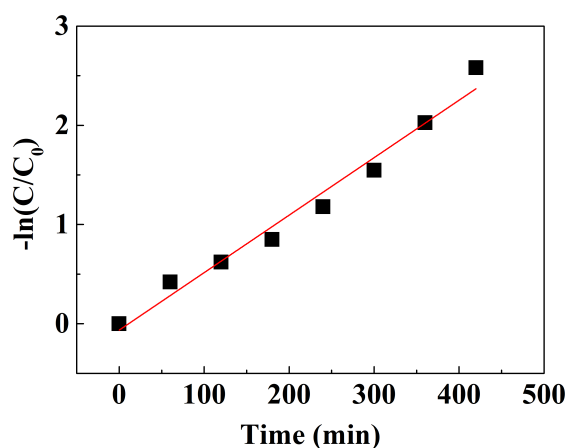


**Figure 4.11:** Semilogarithmic plot of  $\ln (C(t)/C(0))$  against illumination time. The linear trend confirms the pseudo-first-order kinetics of the MB photodegradation, with the slope corresponding to the photodegradation constant  $k$  as given by the equation 4.19.

data and provides a clear and quantitative measure of photocatalytic activity by evaluating how

quickly the MB dye concentration decreases under UV illumination. For thin film photocatalysts, the degradation rate  $k$  is usually normalized by the film area. For our experiments, the films are deposited on glass plates with an area of  $3 \text{ cm}^2$ . This normalization enables a standardized comparison of the photocatalytic activity of different film samples, as the influence of the film surface area on the photodegradation process is taken into account. In addition, several different parameters were defined for each test series to ensure consistent and reliable results. Firstly, the initial dye concentration was  $5 \text{ mg/L}$ . It was found that higher concentrations lead to longer degradation times. Secondly, the volume of the solution was  $15 \text{ mL}$ . This standardization ensures that the dye concentration and the volume of the solution are the same in all experiments, allowing an accurate comparison of photocatalytic activity. The intensity of the light was also controlled by maintaining a uniform distance between the lamp and the film. The distance between the UV lamp and the photocatalyst was set at  $4 \text{ cm}$ , and in the case of simulated solar light it was  $33.5 \text{ cm}$ . The light intensity at a given distance was  $0.2 \frac{\text{mW}}{\text{cm}^2}$  and  $2.2 \frac{\text{mW}}{\text{cm}^2}$ . The positions of the photocatalysts were fixed during the experiments to prevent fluctuations in light intensity from influencing the photodegradation rate. In addition, the film thickness should be above a certain threshold to ensure maximum efficiency. During the experiments, the temperature was kept approximately constant. This control is important as temperature fluctuations can influence photocatalytic activity by affecting both the catalyst and the degradation kinetics.

These fixed parameters help to minimize experimental variability and ensure that observed differences in photocatalytic performance are primarily due to the properties of the photocatalyst and not to external factors.

### 4.3.2 Testing on Microplastic Fibers

In the second part of the experimental study, the films with the best photocatalytic activity from the first phase were tested for their ability to degrade microplastics. Three types of microplastics were selected for this purpose: Polypropylene (PP), Polyamide (PA) and Polyethylene Terephthalate (PET). Preliminary tests showed that only the PET fibers exhibited a measurable reduction in fiber diameter. These PET fibers supplied by Goodfellow Cambridge Limited have an initial diameter of  $14 \mu\text{m}$ . The packaging contains a continuous thread of 15 fibers.

For sample preparation, a single fiber was separated from the bundle and wrapped around a holder. The holder was a  $1.5 \text{ cm} \times 1 \text{ cm}$  Teflon (polytetrafluoro ethylene, PTFE) frame with small notches on the sides to hold the fiber in place. These holders ensured uniform fiber spacing

during synthesis and uniform height during photocatalytic degradation. In addition, the design of the holder allowed the same spots to be imaged at different stages of the experiment.

After the microplastic fibers were prepared on the holder, a thin ZnO film was applied to the fibers. Two synthesis methods were used: one at room temperature with 250 W RF power and the other at 80 °C with 50 W RF power. The film thickness was varied and ranged from 40 cy to 360 cy (corresponding to about 5 to 43 nm).

After synthesis, the holders with the fibers were placed in different aqueous media: ultrapure water (Milli-Q, MQ), tap water and an aqueous NaCl solution (simulated seawater). For all listed solutions pH and conductivity was measured.

Medium	pH	$\kappa$ ( $\mu\text{S}/\text{cm}$ )
Milli-Q water	6.92	0.055
tap water	7.39	476
0.65 M NaCl solution	7.7	32400

**Table 4.1:** Measured pH values and electrical conductivities ( $\kappa$ ) of aqueous media used as a medium for PET degradation. The media tested included ultrapure water (Milli-Q), tap water and a 0.65 M NaCl solution.

Two types of light sources were used for illumination: a UVC light source (OSRAM Puritec HNS 6 W G5) and a sun simulation lamp (OSRAM Vitalux Ultra 300 W). The duration of illumination varied from 1 hour to 48 hours.

The degradation of PET microfibrils was quantified using eSEM. The fibre thicknesses were measured directly from the eSEM images. The following equations were used to evaluate the percentage of photodegradation:

$$\text{Degradation}(\%) = 100\% - \left( \frac{d_{\text{final}}}{d_{\text{untreated}}} \right)^2, \quad (4.20)$$

$$\text{Degradation}(\%) = 100\% - \left( \frac{d_{\text{final}}}{d_{\text{control}}} \right)^2. \quad (4.21)$$

Where  $d_{\text{final}}$  stands for the diameter of the fibres after degradation treatment.  $d_{\text{untreated}}$  refers to the diameter of the original, untreated fibres, which serve as the basis for the comparison.  $d_{\text{control}}$  refers to fibres that were subjected to the same test conditions (e.g. illumination time, medium), except for the presence of the photocatalyst. The control sample takes into account

any changes in fibre morphology caused by light exposure alone and helps to isolate the specific effect of the photocatalyst on degradation.

## Chapter 5

# Results

This chapter presents the experimental results of this study, focusing on the factors that influence the photocatalytic activity of the ZnO films deposited with PEALD. It begins with a comparison of films synthesized by ALD and PEALD. In the following sections, the influence of the deposition temperature is investigated, including the role of the film thickness and the initial methylene blue concentration. The effect of different light sources on photocatalytic efficiency is also investigated. In addition, the influence of plasma process parameters on the film properties is analysed. Finally, the most promising films are tested for their effectiveness in degrading PET microfibers to illustrate their potential for environmental applications.

### **5.1 Comparative Photocatalytic Activity of Thin ZnO Films Deposited by ALD and PEALD at fixed temperature**

Previous studies have shown that ZnO films synthesised by the PEALD method differ significantly in several important aspects from films deposited by thermal ALD. They have a smaller grain size and a preferred (100) growth orientation [60]. Their electrical resistance is significantly higher [50], while charge carrier density and mobility are significantly lower [62, 125]. The Zn/O is substoichiometric [53, 67], which indicates a deviation from the ideal film composition. In addition, their excitonic emission is significantly increased [64], indicating significant differences in the electronic structure.

The photocatalytic potential of thin ZnO films synthesised by ALD is well established [29, 126]. However, given the different structural and electronic properties of PEALD films, a more detailed investigation of their photocatalytic performance is necessary. In this section, ZnO

thin films deposited using ALD and PEALD techniques at the same temperature of 80 °C are compared. Glass slides were used as substrates for photocatalytic measurements, silicon wafers for structural characterization and quartz substrates for optical analysis. The SEM images showed

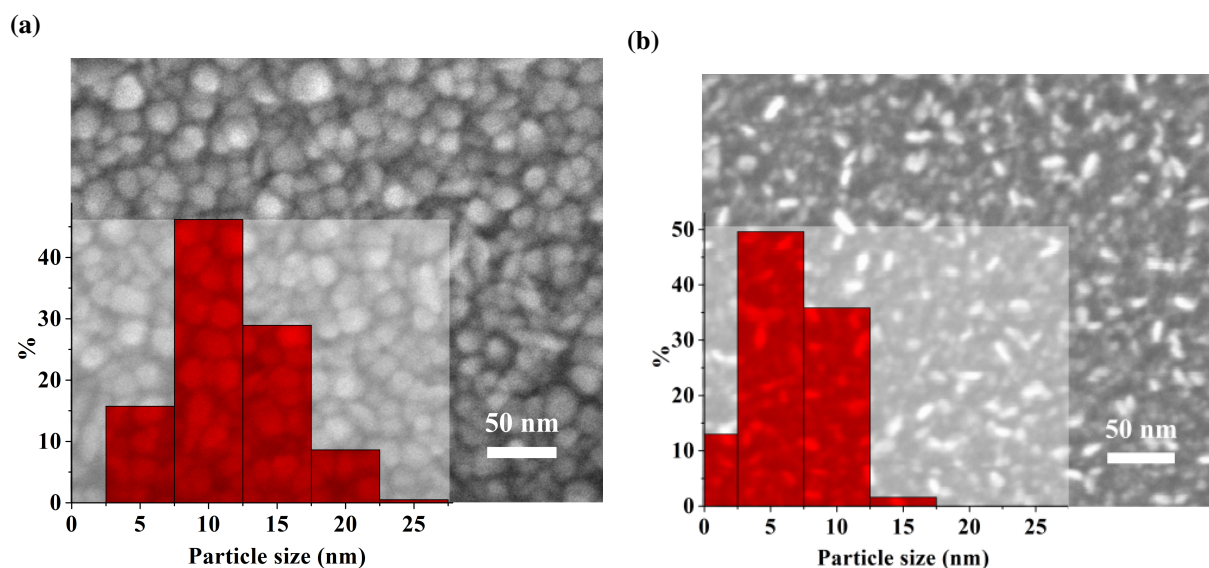


**Figure 5.1:** SEM images of (a) ALD grown thin ZnO film and (b) PEALD grown thin ZnO film with grain size distribution. Deposition temperature for both films is 80 °C.

clear differences in the surface morphology. The ALD film (Fig. 5.1a) showed densely packed, round grains with diameters between 10 and 20 nm. In contrast, the PEALD film (Fig. 5.1b) showed smaller, more elongated grains with a diameter of around 5–10 nm. HRTEM analysis (Fig. 5.2) revealed further differences in the crystal structure in cross-section. The ALD-grown films have columnar grains orientated perpendicular to the surface, while the PEALD-grown films are consisted of smaller, rounded grains with diameters of 5–10 nm. For both films, FFT of HRTEM images reveals (010) and (011) planes of wurtzite ZnO. Diffraction spots corresponding to the (002) plane are observed in the ALD-grown ZnO thin film, but remain unresolved in the PEALD-grown film.

Similar structural differences between the two films can also be seen in the GIXRD spectra (Fig. 5.3). For both the ALD and PEALD films, the positions of the GIXRD peaks match well with the reference diffraction peaks of wurtzite ZnO powder. However, variations in the relative intensities of the Bragg peaks indicate favoured crystallographic orientations in both cases. The ALD film exhibits a dominant (002) peak. In contrast, the PEALD film shows a stronger (100) peak, indicating a (100)-like texture, although the degree of preferential orientation is

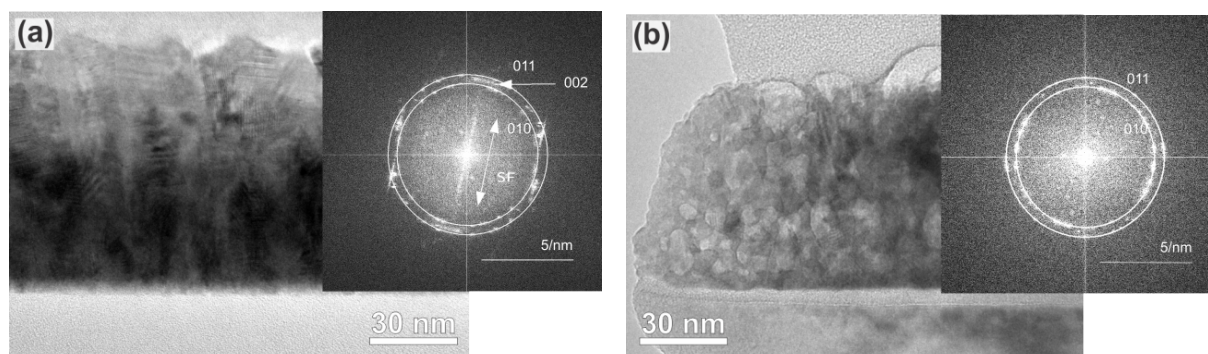


**Figure 5.2:** HR-TEM cross-sectional images of thin ZnO films deposited by (a) thermal ALD and (b) PEALD, together with the corresponding FFT analyses.

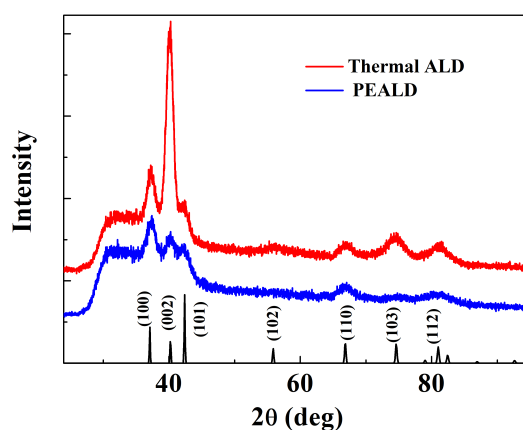


**Figure 5.3:** GIXRD analysis of thin ZnO films deposited with ALD and PEALD at same temperature of 80 °C.

significantly weaker. This indicates a higher proportion of randomly orientated ZnO crystallites in the PEALD films compared to the thermally grown ALD films.

Additional insights into the chemical composition of the films were gained through XPS analyses. Both the ALD and PEALD samples exhibit symmetric Zn  $2p_{3/2}$  peaks centred at the binding energy of 1022.4 eV, consistent with Zn<sup>2+</sup> in ZnO. The O 1s core level spectra (Fig. 5.4b) consist of two components: a dominant peak at 531.5 eV, which is attributed to O<sup>2-</sup> ions in the ZnO lattice, and a secondary peak at 533.0 eV, which is usually associated with oxygen impurities due to O-H groups on the surface [29] or low-coordinated oxygen ions such as the oxygen ions adjacent to the Zn vacancies [127]. A higher intensity of the 533.0 eV peak in the PEALD sample could indicate the presence of zinc vacancies.

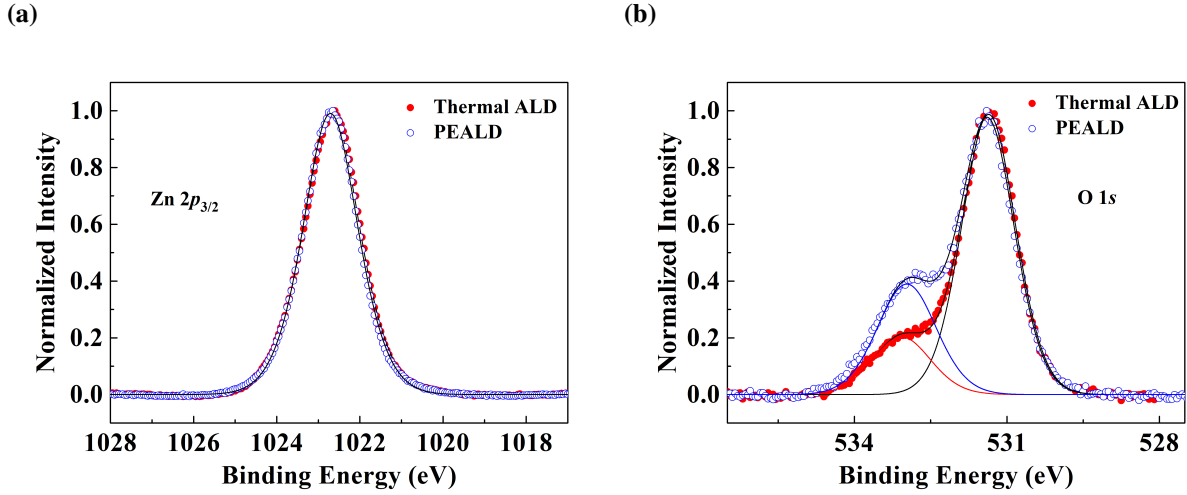


**Figure 5.4:** XPS spectra around Zn 2  $p_{3/2}$  (a) and O 1s core-levels (b).

In addition, the Zn/O atomic ratio was estimated from the integrated areas of the Zn 2 $p_{3/2}$  and O 1s peaks after subtracting the Shirley background and normalising to a stoichiometric epitaxial ZnO reference. The PEALD film exhibited a Zn/O ratio of 0.85, indicating a Zn-deficient composition, while the ALD film exhibited a near-stoichiometric ratio.

The optical properties of the PEALD-grown ZnO thin film differ markedly from those of the thermally grown ALD film. The optical absorption edge of the PEALD film is significantly broadened below 400 nm (Fig. 5.5a), suggesting a less ordered crystal structure. Moreover, the optical bandgap is noticeably blue-shifted, with a value of 3.52 eV, compared to 3.26 eV for the ALD film, as determined from Tauc plots (Fig. 5.5b).

The PL measurements show even clearer differences. The PEALD film shows a significantly increased excitonic near-band edge emission at 390 nm (Fig. 5.6a). This enhancement correlates with more efficient photoexcitation in both the UVC (200–280 nm) and UVB (280–315 nm) spectral ranges (Fig. 5.6b). Similar differences in PL between ALD and PEALD ZnO films were reported, with higher oxygen content leading to stronger excitonic emissions [64].

The photocatalytic performance, evaluated through MB dye degradation under UV light (Fig. 5.7a), follows an first-pseudo model (eq. 4.19). The rate constant for the ALD film is  $k_{\text{ALD}} = 0.8 \cdot 10^{-3} \text{ min}^{-1}\text{cm}^{-2}$ , while the PEALD film shows a significantly higher constant of  $k_{\text{PEALD}} = 2.7 \cdot 10^{-3} \text{ min}^{-1}\text{cm}^{-2}$ . This indicates that PEALD can achieve effective photocatalytic activity even at a low deposition temperature of 80 °C, attributed to increased charge carrier concentration and reduced recombination rates due to lower crystallinity and

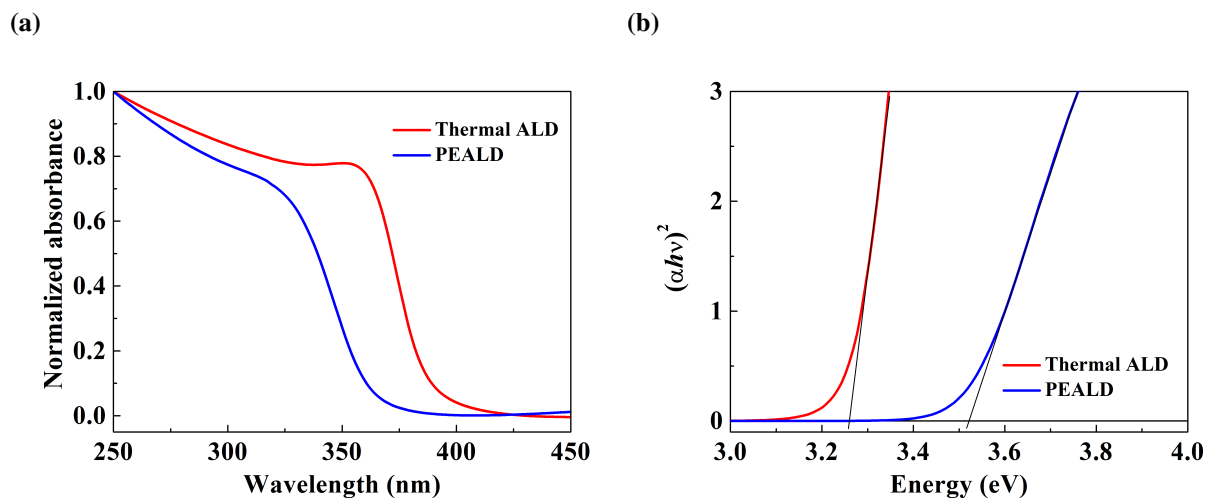


**Figure 5.5:** Optical absorption spectra (a) and corresponding Tauc plots (b) for thALD and PEALD grown thin ZnO films.

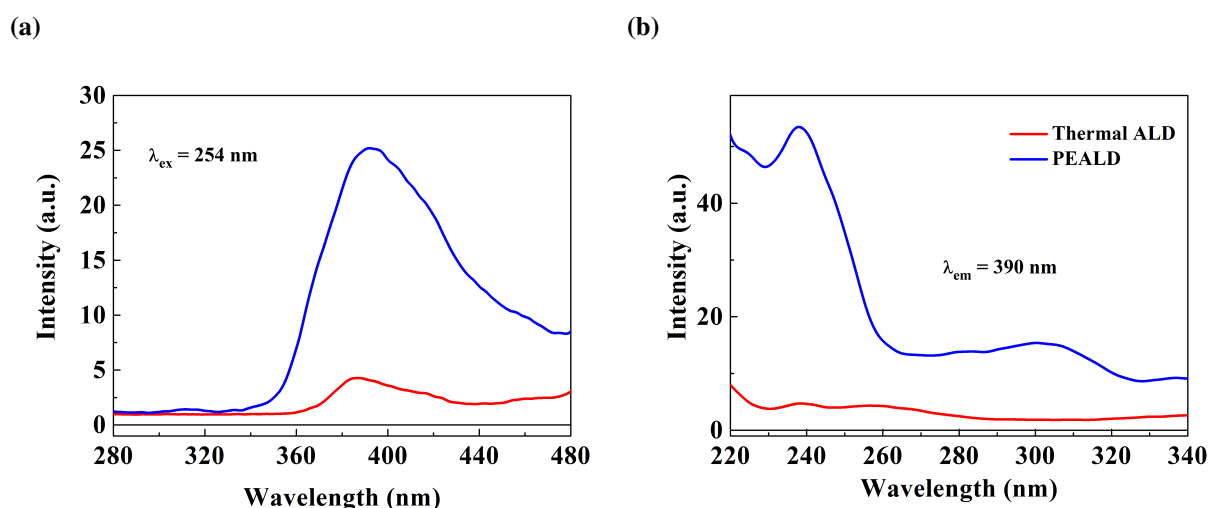


**Figure 5.6:** Photoluminescence spectra of ZnO films: (a) emission spectra for  $\lambda_{ex} = 254$  nm; (b) excitation spectra  $\lambda_{em} = 390$  nm

higher defect density. To evaluate the reusability of the thin ZnO films deposited with ALD and PEALD, we performed several successive 7-hour degradation cycles on a single sample (Figure 5.8). For the PEALD films, a significant decrease in photocatalytic activity was observed in the third cycle, while the films deposited with ALD showed a constant decrease in efficiency.

To summarise, thin ZnO films deposited with PEALD exhibit significantly improved photocatalytic activity for low deposition temperature (80 °C). These results formed the basis for

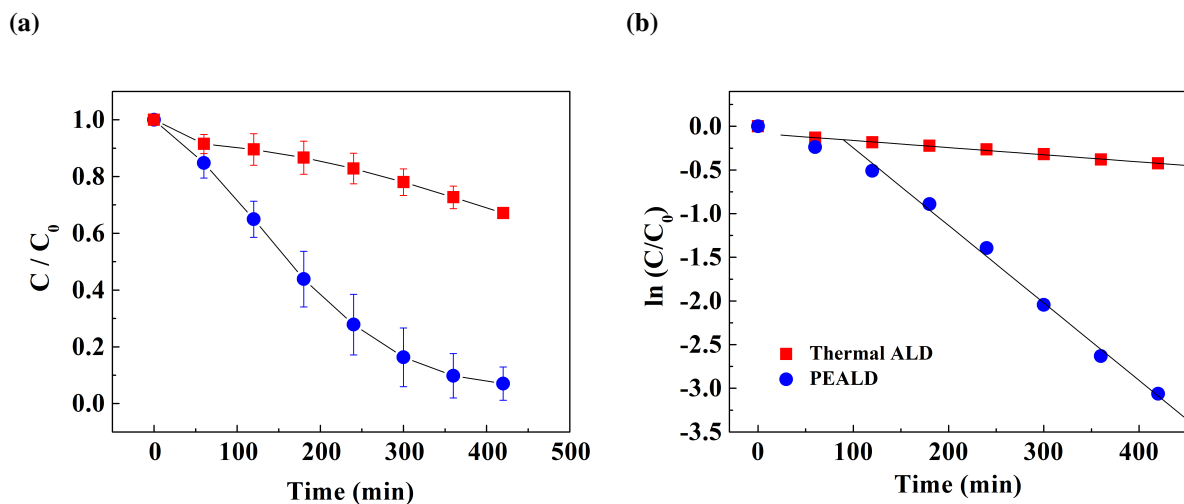


**Figure 5.7:** (a) Photodegradation of MB during 7 hours of UV irradiation for thin ZnO films deposited with thermal ALD (red) and PEALD (blue). (b) A semi-logarithmic diagram was used to evaluate the photodegradation rate.

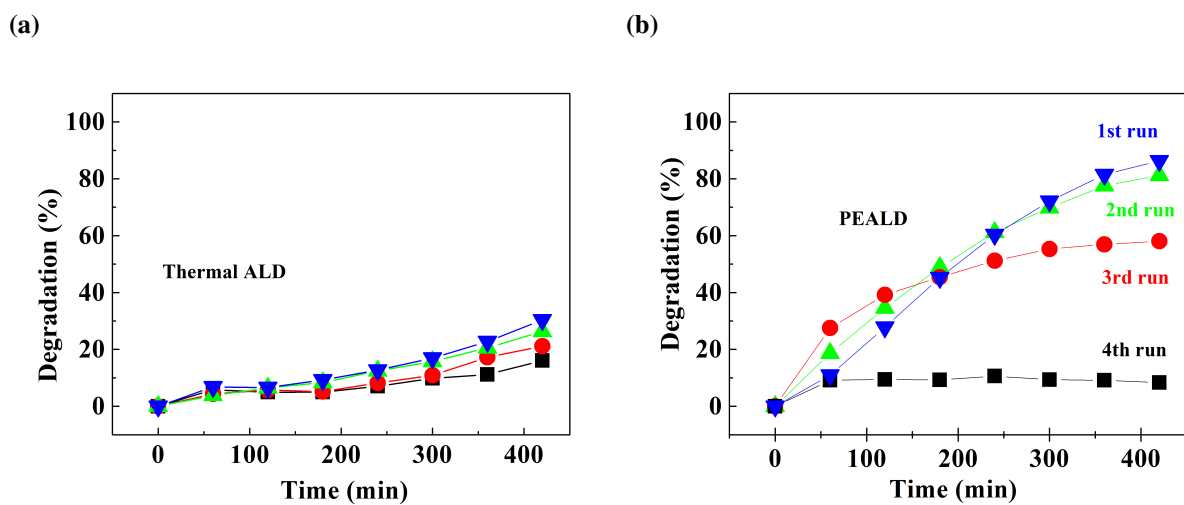


**Figure 5.8:** Stability of thin ZnO films deposited with thALD (a) and PEALD (b).

further investigation of PEALD synthesis parameters and their influence on film morphology and functional performance.

## 5.2 Impact of Deposition Temperature on Photocatalytic Activity

The results presented in section 5.1 show the great potential of thin ZnO films deposited with PEALD for photocatalysis. As in conventional ALD, the deposition temperature is a crucial factor influencing the properties of the films and is the first parameter to be systematically investigated. To ensure the reliability and consistency of the experiments, initial measurements were performed to standardise two key parameters of the photodegradation process: the film thickness and the initial concentration of methylene blue.

### 5.2.1 Role of Film Thickness

The first step was to determine the minimum effective film thickness, as photocatalysis is a surface-driven effect. The photocatalytic activity was measured for different film thicknesses at a synthesis temperature of 80 °C. It was found that increasing the film thickness beyond 175 cycles did not further enhance the efficiency of photocatalytic degradation (Fig. 5.9).

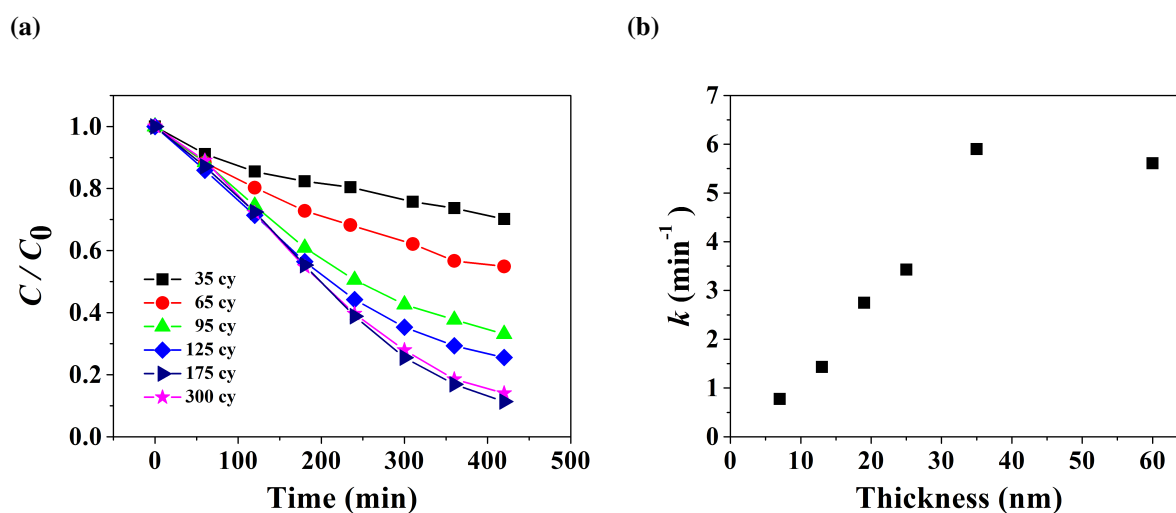


**Figure 5.9:** Photocatalytic performance of PEALD-grown thin ZnO films as a function of film thickness at a deposition temperature of 80 °C: photodegradation curves (a), corresponding first-order rate constants (b).

Given a GPC of 0.2 nm/cy at 80 °C, 175 cycles correspond to a film thickness of 35 nm. This result aligns well with the findings of Di Mauro et al. [128], which report that film thickness

has no significant influence on photocatalytic activity beyond 20 nm. Their measurements were conducted on thin ZnO films deposited by conventional atomic layer deposition (ALD).

### 5.2.2 Impact of Initial Methylene Blue Concentration

The concentrations of methylene blue should be within the measurable range of the UV-Vis spectrophotometer, which has a saturation limit above an absorbance of 4. It was also found that the concentration of MB affects the photodegradation rate: higher concentrations lead to slower photodegradation. This is because the light intensity decreases at higher concentrations and the reaction kinetics are affected. All measurements presented here were performed for thin ZnO films deposited by thermal ALD at different deposition temperatures, although a similar dependence on MB concentration can also be observed for PEALD-grown films.

As can be seen in Figure 5.10a, although the trend remains the same for different photocatalysts, the absolute photodegradation rate varies depending on the initial MB concentration.

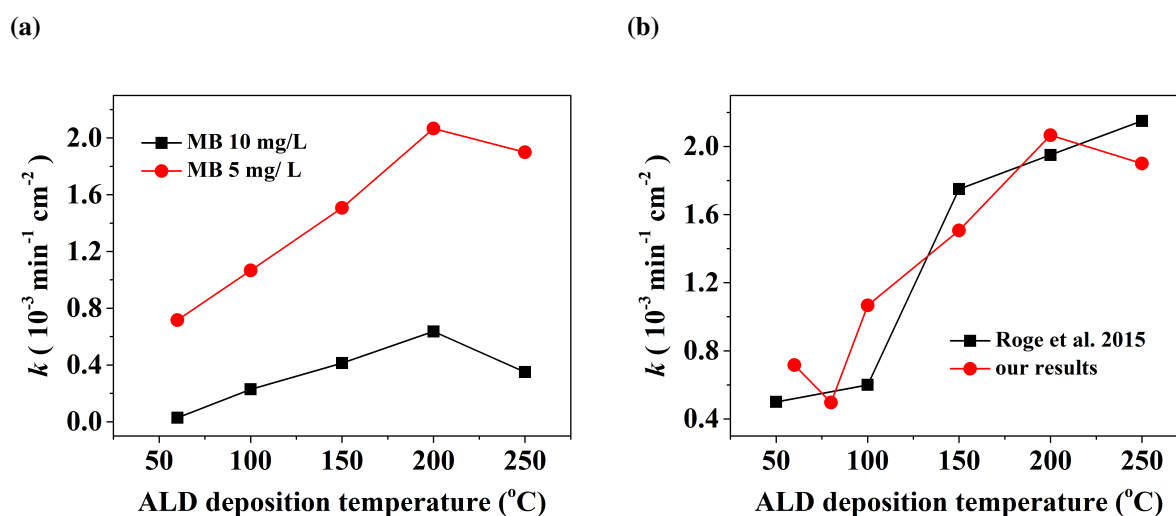


**Figure 5.10:** Photodegradation kinetics of MB at two initial concentrations (a). Comparison of our results at 5 mg/L with data from Rogé et al. [126], which show excellent agreement (b).

This comparison was performed at initial absorbance values of  $A = 2.3$  and  $A = 1.15$ . Taking into account the Beer-Lambert law 4.13 and using the extinction coefficient of  $\epsilon(664 \text{ nm}) = 74000 \frac{\text{L}}{\text{mol cm}}$ , the absorbance value for  $A = 1.15$  corresponds to a concentration of 5 mg/L, while  $A = 2.3$  corresponds to a concentration of 10 mg/L. In a publication by Rogé et al.

[126], the initial MB concentration was also set to 5 mg/L, and the results were almost identical to ours (Fig. 5.10b). For this reason, we also chose this concentration as the starting point.

### 5.2.3 Influence of Deposition Temperature

In this section, the optimisation of the deposition temperature at minimum RF power was carried out. Thin ZnO films were deposited by PEALD at different temperatures between 60 °C and 250 °C. At a constant number of deposition cycles (500 cycles), film thicknesses between 75 and 125 nm were obtained. This corresponds to a GPC of 0.15 to 0.25 nm/cy, which is comparable to the values reported in [50, 60, 64]. A few publications report higher growth rates [62, 129], but as discussed in [68], the growth rates vary considerably due to different reactor configurations and synthesis conditions.

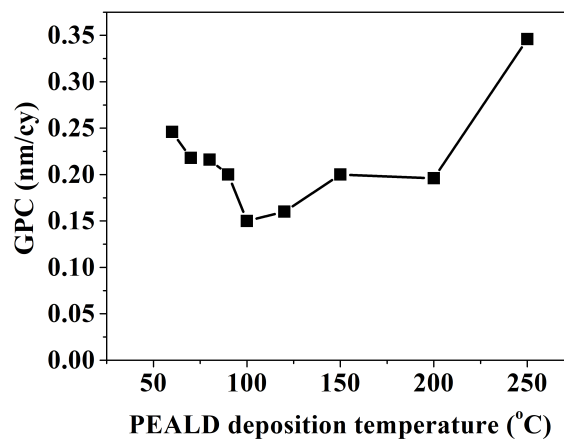


**Figure 5.11:** GPC of ZnO films deposited by PEALD at varying substrate temperatures with a fixed RF power of 50 W.

In our case, the GPC is approximately constant in the temperature range from 60 °C to 200 °C and increases below and above this range, as described in the section 2.1.

The results of the GIXRD analysis show that the positions of the diffraction peaks correspond to those characteristic of ZnO in a wurtzite structure [130] with widths typical of nanomaterials. However, there were significant differences between the samples deposited at different temperatures (Fig. 5.12). For a sample deposited at 60 °C, the relative intensities of the dominant peaks are similar to the randomly orientated ZnO powder (JPG), with a weak (002) peak. At higher deposition temperatures, the intensity of the (002) peak gradually increased, indicating a

preferential orientation of growth along this plane perpendicular to the substrate surface. These results are consistent with previous studies [50, 60].

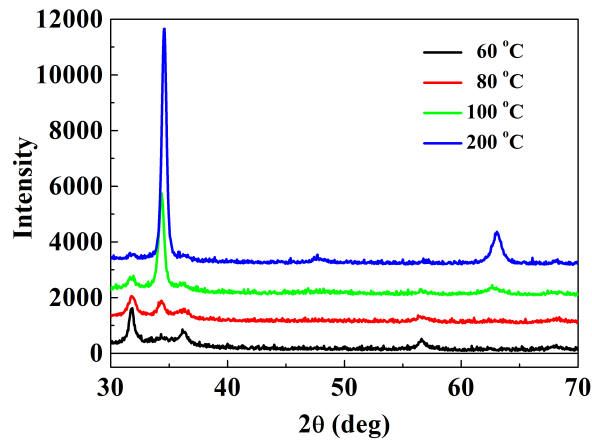


**Figure 5.12:** GIXRD diffractograms of ZnO films deposited with PEALD at different temperatures.

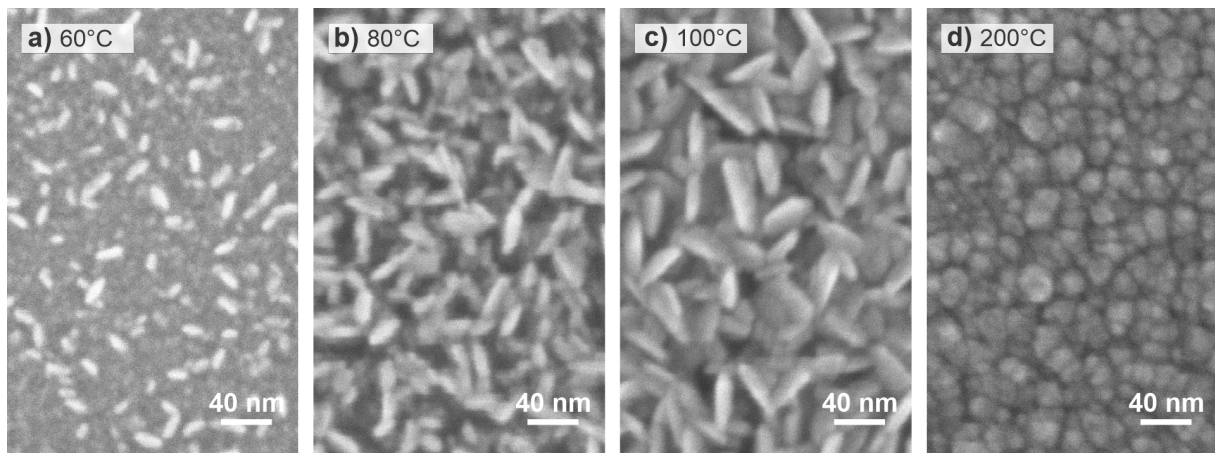


**Figure 5.13:** SEM images of thin ZnO films deposited with PEALD at different temperatures: 60 °C (a), 80 °C (b), 100 °C (c), 200 °C (d).

SEM images (Fig. 5.13) revealed a homogeneous polycrystalline surface across all samples. For sample deposited at 60 °C, grains were poorly resolved, only revealing small and bright elongated features. At 100 °C, well-defined rectangular facets ( $\sim 100 \times 10$  nm) appeared. Surface of samples grown at 200 °C, exhibited a ceramic-like texture with uniform 20 nm grain diameter. While XRD suggested stronger orientation along the z-axis, SEM only revealed surface features, not subsurface crystallinity or defects.

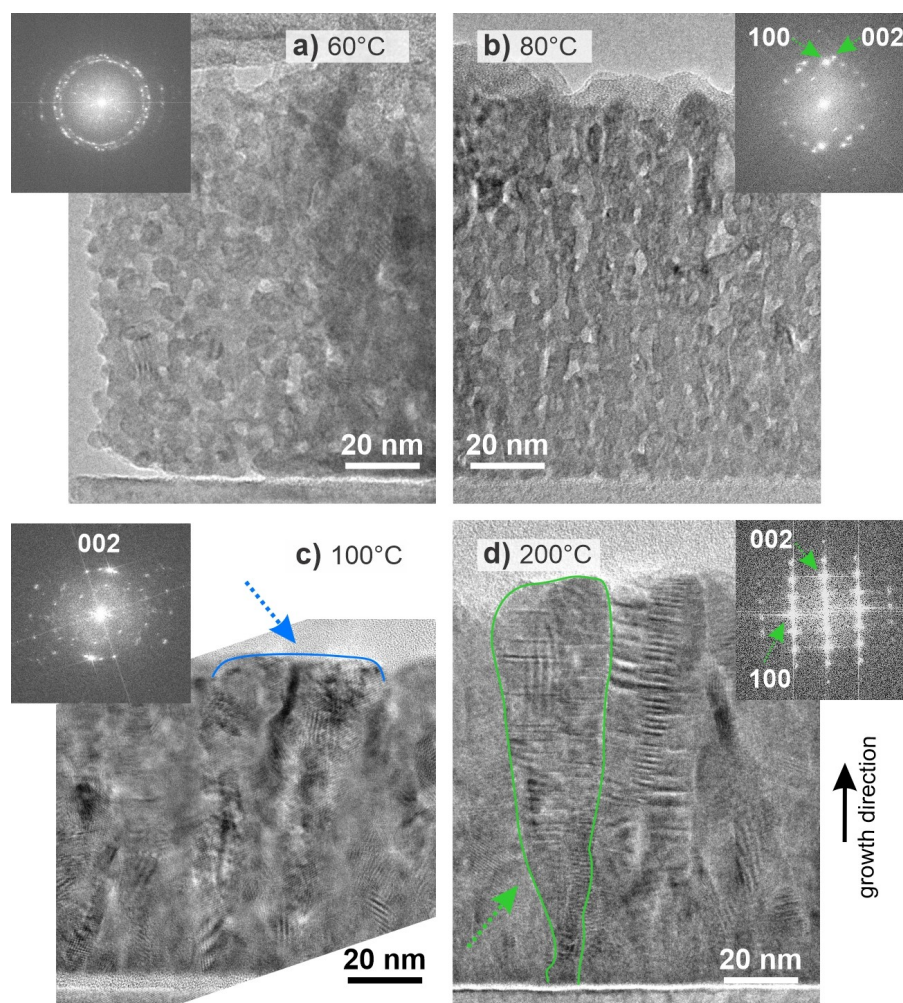


**Figure 5.14:** HRTEM analysis of ZnO thin films deposited at different temperatures: 60 °C (a), 80 °C (b), 100 °C (c), 200 °C (d).

HRTEM images (Fig. 5.14) provided further insight into the polycrystalline nature. The films grown at 60 °C consist of small ( $\sim 5$  nm) round crystallites with no obvious preferential orientation, which was confirmed by FFT (Fig. 5.14a). In samples deposited at 80 °C, more (002) planes aligned parallel to the surface (Fig. 5.14b). At 100 °C (Fig. 5.14c), the voids decreased as the ZnO lattices bridged adjacent grains. For samples deposited at 200 °C, more grains extend from near the substrate to the top surface and show a strong preferred orientation along the  $z$ -direction of the wurtzite lattice. The average grains are narrower near the substrate and become wider towards the top, densely filling the space. This dense packing has probably led to deformations or stacking faults, as can be seen in the calculated FFT image (Fig. 5.14d). XPS analysis revealed consistent Zn  $2p_{3/2}$  spectra across samples, but O  $1s$  spectra (Fig. 5.15a)

showed temperature-dependent trends. Two peaks were observed: a primary peak at 531 eV (photoemission from  $O^{2-}$  ions in wurtzite ZnO) [29, 126] and a smaller peak at 533 eV, attributed to oxygen related defects: non-stoichiometric oxygen (O atoms in a ZnO wurtzite crystal matrix in the vicinity of Zn vacancies [127], surface adsorbed/chemisorbed oxygen [131, 132] or hydroxyl groups/water molecules [133]).

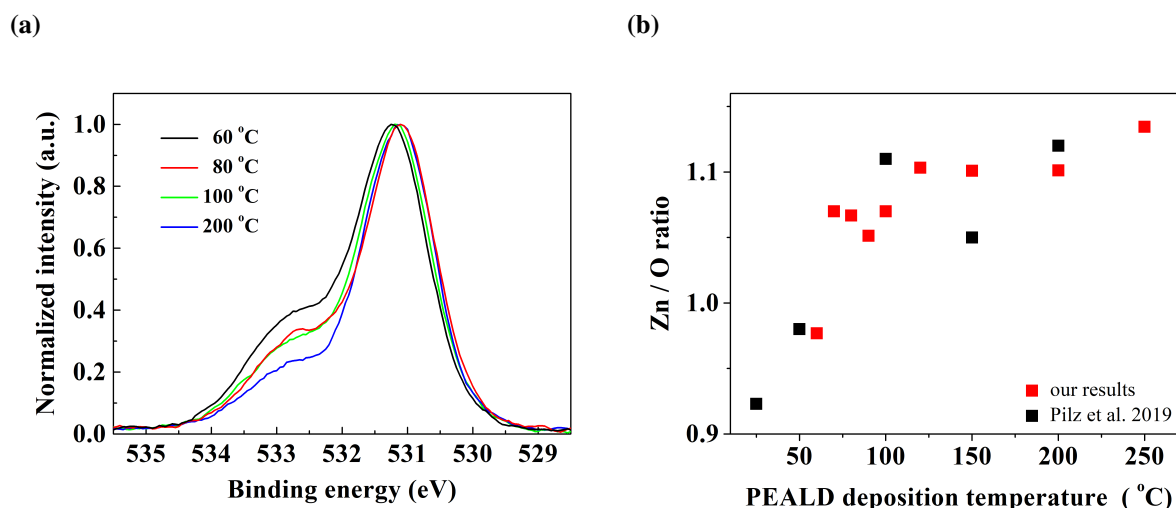


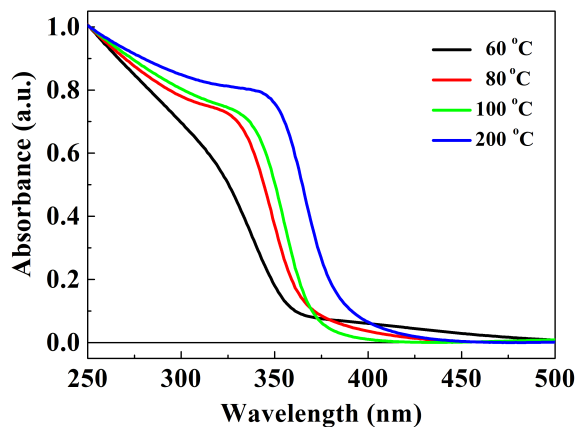
**Figure 5.15:** XPS O 1s spectra of thin ZnO films deposited with PEALD at different temperatures (a). Corresponding Zn/O atomic ratio trends derived from XPS (b).

In the earlier ALD studies on ZnO, where DEZ and  $H_2O$  were used as precursors, minor peak was usually attributed to OH impurities [29, 126]. Since the oxygen precursor in PEALD synthesis is the  $O_2$  plasma and not water vapour as in the case of thermal ALD synthesis, we can rule out a large contribution of OH impurities or  $H_2O$  molecules in our films. The intensity of the minor peak increases for lower deposition temperatures. This indicates a larger amount of non-stoichiometric oxygen and surface oxygen species for ZnO samples grown at lower temperatures. This is in good agreement with our TEM analysis, which shows smaller crystallites and a larger amount of grain interstices for samples deposited at temperatures below 100 °C. Therefore, we can attribute the peak at 533 eV to non-stoichiometric oxygen located at the grain boundaries and Zn vacancies.

Deposition Temp. (°C)	O 1s Peak Area	Zn 2p <sub>3/2</sub> Peak Area	Zn/O Ratio
60	8203	99706	0.9769
80	8688	115312	1.0667
100	7697	102474	1.0700
150	8355	114446	1.1009
200	8337	114240	1.1012
250	8244	116371	1.1345

**Table 5.1:** Average peak areas for O1s and Zn 2p<sub>3/2</sub> at different deposition temperatures and the corresponding Zn/O ratios.

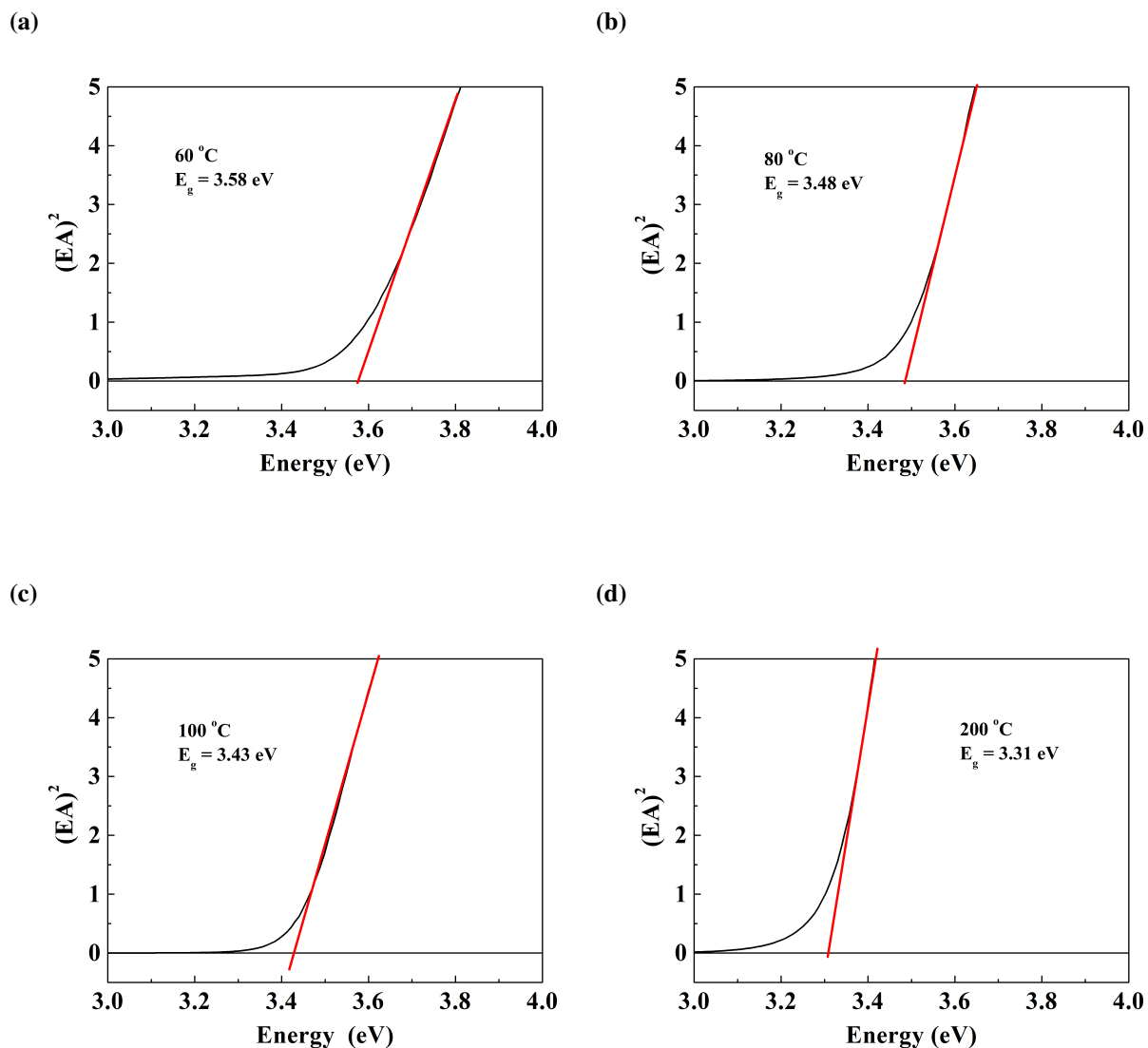
To obtain the Zn/O ratio, the areas under the O 1s and Zn 2p<sub>3/2</sub> peaks are determined. Table 5.1 gives the average values for four measurements. The obtained results agree well with the results obtained in [68], where the thin ZnO films deposited by the method PEALD for the RF - power of 60 W were observed (Figure 5.15b).



**Figure 5.16:** Optical absorption spectra of ZnO films deposited at different temperatures.

The absorption edge in the optical absorption spectra (Fig. 5.16) showed a blue shift in the films deposited at lower temperatures. This shift is consistent with [134], where it is associated with changes in the crystal size of ZnO nanoparticles. For films with crystal grains smaller than 10 nm, the quantum confinement effect leads to a larger band gap and a blue shift of the absorption edge. In contrast, films deposited at higher temperatures form larger crystal grains, reducing quantum confinement and shifting the absorption edge towards the visible spectrum. This size limitation

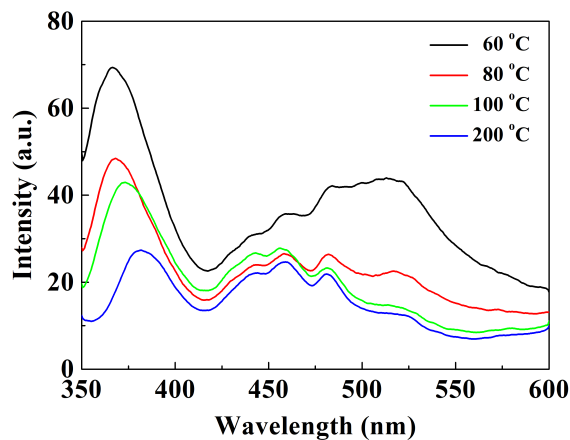
increases the zero kinetic energy of the photoexcited charge carriers, effectively widening the semiconductor bandgap [135]. In addition, the films deposited at low temperatures exhibited an extended absorption tail, which is characteristic of localised electron states in the band gap of amorphous semiconductors [136, 137]. The defect-rich structure of these films likely contributes to the observed optical absorption properties.



**Figure 5.17:** Tauc plots for ZnO films deposited at 60 °C (a), 80 °C (b), 100 °C (c) and 200 °C (d), used to evaluate the optical band gap energies from the absorption spectra.

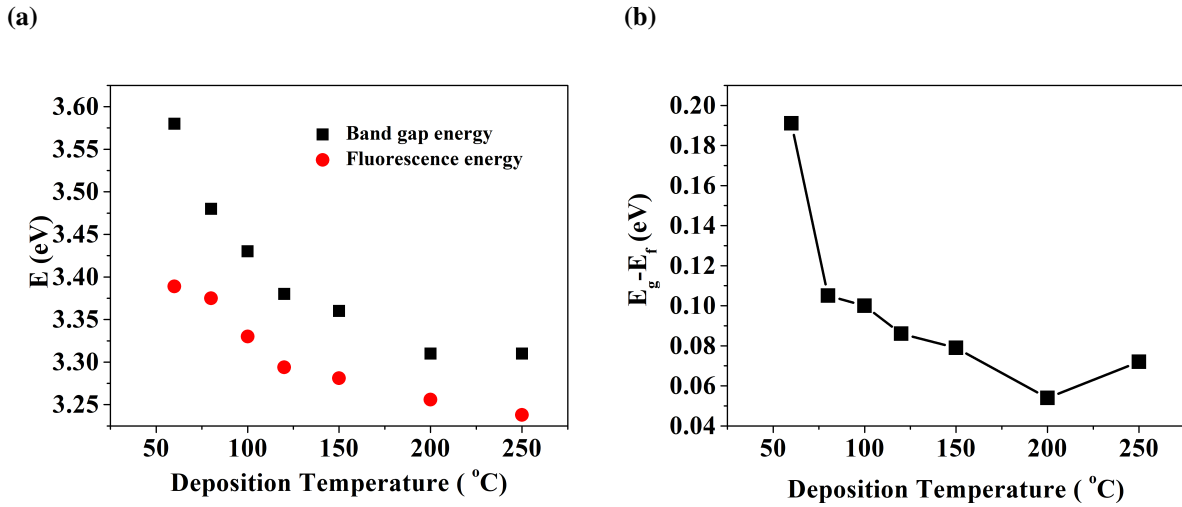
The band gap energies of the films were determined using Tauc plots (Fig. 5.17) and the results are presented in Table 5.2.

Figure 5.18 shows the photoemission spectra of thin PEALD-ZnO films at an excitation wavelength of 320 nm. Two main regions can be distinguished: the emission near the band edge (NBE) between 350 nm and 400 nm and the broad emission between 430 nm and 550 nm, which is due to band defect emissions in the visible range (green emission) [62]. The wavelength of the maximum excitonic emission gradually increases with the increase of the deposition temperature from 366.5 nm for 60 °C to 382 nm for 200 °C.



**Figure 5.18:** Photoluminescence spectra of PEALD-ZnO films excited for excitation wavelength of 320 nm.

The corresponding fluorescence energy was calculated from these wavelengths. There is a slight difference between the band gap energy and the fluorescence energy, which is due to the rapid transition to states below the band gap energy. In Fig. 5.19a the band gap energy and the fluorescence energy are plotted as a function of the deposition temperature.



**Figure 5.19:** Band gap energy and fluorescence energy of PEALD-grown ZnO films as a function of deposition temperature (a). Difference between band gap energy and fluorescence energy as a function of deposition temperature (b).

Both the band gap energy and the fluorescence energy decrease with the deposition temperature, and their difference also decreases. Since the crystal grain size increases with the deposition temperature, it can be concluded that the difference between band gap energy and fluorescence energy decreases with the crystal grain size, which is consistent with the literature [134]. Furthermore, the green emission present in all spectra can be attributed to zinc vacancies, which agrees well with XPS spectra.

Temperature ( $^{\circ}\text{C}$ )	$E_g$ (eV)	$E_f$ (eV)	$E_g - E_f$ (eV)
60	3.58	3.389	0.191
80	3.48	3.375	0.105
100	3.43	3.33	0.100
150	3.36	3.281	0.079
200	3.31	3.256	0.054
250	3.31	3.238	0.072

**Table 5.2:** Band gap ( $E_g$ ) and fluorescence energy ( $E_f$ ) values for different deposition temperatures.

To evaluate the influence of deposition temperature on the photocatalytic performance of ZnO thin films, MB degradation tests were carried out under UV illumination. Figure 5.20b shows the results of the photocatalytic degradation test. For the PEALD-ZnO film deposited at 60 °C, the MB concentration degradation is the fastest. The photocatalytic efficiency of each sample can be defined by the photodegradation kinetic constant  $k$ , which is given by the following expression 4.18. The values of the kinetic constant for each deposition temperature for the ALD and PEALD methods are shown in Fig. 5.20a. For the thermal ALD, the best photocatalytic activity was observed for films deposited at temperatures above 150 °C [29, 126], while the films deposited by the PEALD method showed a maximum value for films deposited at temperatures below 100 °C. Comparable results for ALD-grown films were previously reported by Roge et al. [126] as discussed in 5.2.2. In Fig. 5.20b the results of the photocatalytic tests for ALD-grown thin ZnO films are compared with PEALD-grown films.

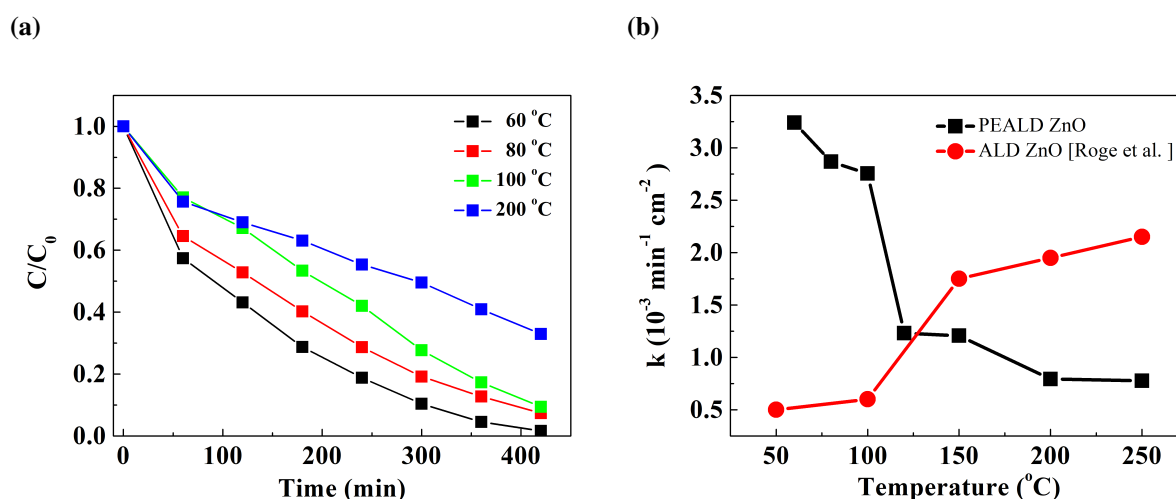


**Figure 5.20:** Photodegradation curves of MB in aqueous solution under UV irradiation for PEALD-ZnO films deposited at different temperatures (a). Corresponding photocatalytic rate constants ( $k$ ) in comparison between thermal ALD and PEALD processes (b).

Photocatalytic activity was evaluated using UV degradation of methylene blue in aqueous solution (Fig. 5.20). A clear trend emerged: lower deposition temperatures resulted in stronger photocatalytic performance. The 60 °C film completely degraded MB in 420 minutes, while films deposited at higher temperatures exhibited  $\sim 30\%$  lower activity.

This behavior aligns with structural differences observed in our study. Low-temperature films consist of small ( $\sim 5$  nm) grains with a high surface-to-volume ratio and abundant trapping

sites, reducing charge carrier recombination. A prolonged lifetime of photoexcited carriers in ZnO quantum dots smaller than 5 nm has been observed in fluorescence decay measurements [134] and in ultrathin ZnO films [138]. The reduced recombination rate directly increases the surface concentration of active charge carriers, enhancing photocatalytic activity. A comparable relationship between particle size and photocatalytic efficiency has also been noted in ZnO nanoparticles [139].

## 5.3 Photocatalytic Performance under Different Light

### Sources

The photocatalytic efficiency is strongly influenced by the optical properties and structural characteristics of the photocatalyst material as well as the spectral distribution of the incident light. In this section, the photocatalytic performance of ZnO thin films prepared by PEALD and ALD is compared under different illumination conditions. The deposition temperature was selected as the one that has maximum photocatalytic efficiency and was 200 °C for the ALD [29, 126] and 60 °C for the PEALD method (section 5.2). To understand the underlying mechanisms of photocatalytic activity, the optical absorption, crystal morphology and grain structure of the films are analysed and correlated with their response to different light sources: UVC, UVA and simulated sunlight.

Figure 5.21a shows the UV-Vis absorption spectra for thin ZnO films prepared using the PEALD and ALD processes. The absorption spectrum of the ALD film shows a clear increase below 380 nm, indicating a well-ordered ZnO structure. In contrast, the absorbance of the PEALD film increases gradually below 360 nm, indicating a less ordered structure. In addition, the PEALD film has a significantly larger band gap (3.62 eV) compared to the ALD film (3.28 eV), as shown in the Tauc plot (Fig. 5.21b).

SEM images show that the ALD film (Fig. 5.22a) consists of larger, round grains (10–20 nm), while the PEALD film (Fig. 5.22b) contains smaller, cylindrical grains (2–5 nm). The crystal structures of ZnO films produced by ALD and PEALD are described in the references [29] and [140].

The emission spectra for different light sources are shown in Figure 5.23a. The OSRAM Supratec lamp exhibits a strong peak at 367 nm, the OSRAM Puritec lamp at 254 nm, and the OSRAM Vitalux lamp displays a spectrum resembling sunlight, with significant intensity above

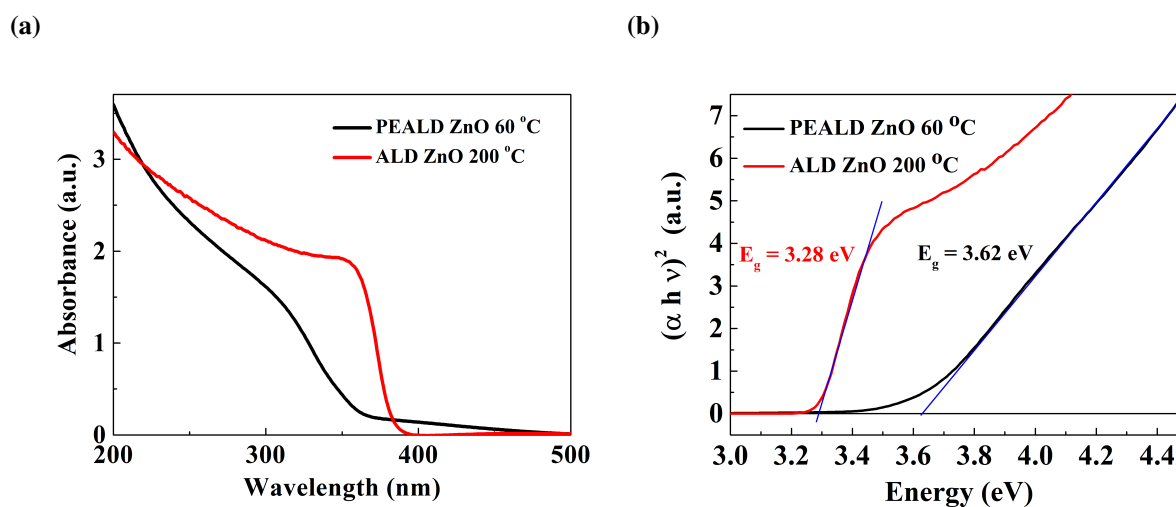


**Figure 5.21:** UV-Vis absorption spectra of ZnO thin films prepared by ALD and PEALD (a). Tauc plots used to evaluate the optical band gap of the ZnO thin films (b).

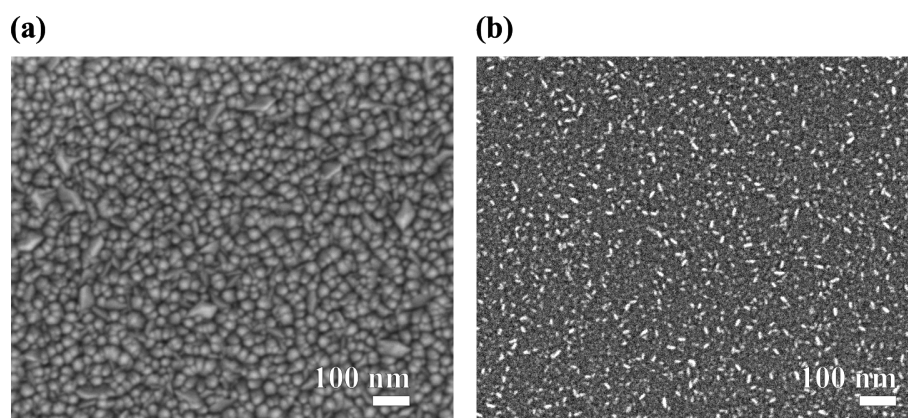


**Figure 5.22:** SEM images of ZnO films deposited by ALD (a) and PEALD (b).

300 nm. The OSRAM Puritec lamp also presents two strong emission peaks at 402 nm and 433 nm, but these are outside the relevant absorption range for the samples.

The results of the photocatalytic degradation test are shown in Figure 5.23b. Under UVC illumination, greater photocatalytic activity is observed for the PEALD film. Despite similar absorbance values at 254 nm for both films (as shown in Figure 5.21a), there are significant structural differences. The smaller grain size of the PEALD film was presented in the previous section with XRR and HRTEM results. In contrast, the ALD film is almost stoichiometric and has a crystal structure similar to the ideal ZnO [29]. Under simulated sunlight, improved photocatalytic performance is observed for the ALD film due to increased absorption in the 300–400

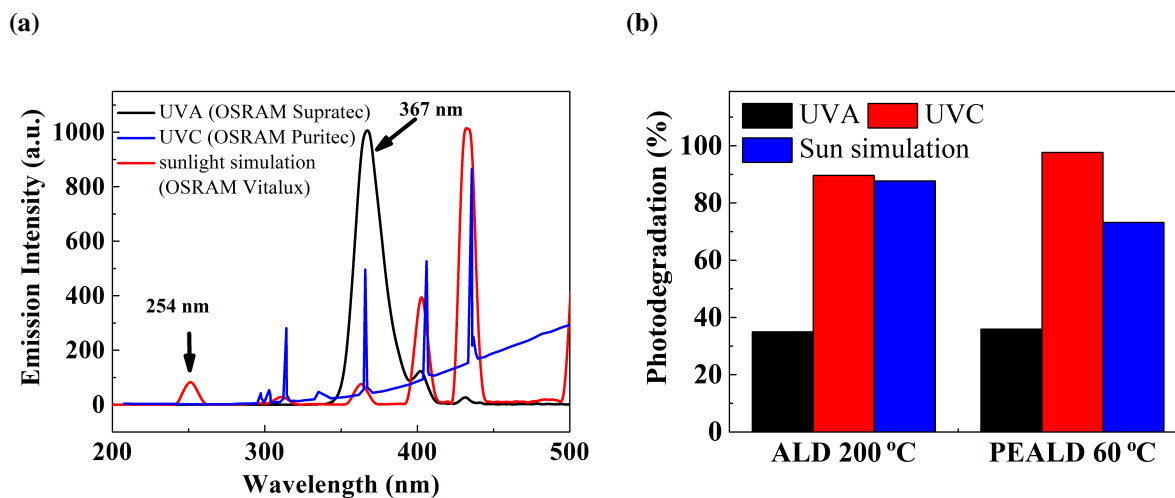


**Figure 5.23:** (a) Emission spectra of light sources used in photocatalytic experiments: OSRAM Supratec (UVA), OSRAM Puritec (UVC) and OSRAM Vitalux (simulated sunlight). (b) Photodegradation efficiency for ZnO thin films deposited with ALD at 200 °C and with PEALD at 60 °C.

nm range. Under UVA illumination (367 nm), no significant difference in photocatalytic activity is observed between ALD and PEALD films, suggesting that the higher optical absorption of the ALD film and the favourable surface morphology of the PEALD film offset each other.

## 5.4 Impact of Plasma Process Parameters

In another set of experiments, the deposition temperature of thin ZnO films was fixed at room temperature (RT), while the RF power was varied between 50 W and 300 W. In this case, a constant number of deposition cycles (500 cy) resulted in a wide range of film thicknesses, from 180 nm to 520 nm. To ensure consistent film thickness across the samples, the depositions were repeated and adjusted, maintaining the thickness approximately between 100 and 200 nm.

GIXRD patterns (Fig. 5.24) show that the crystal structure of the ZnO films depends significantly on the plasma power applied during deposition. Films synthesised at the lowest RF power exhibited a broad, weak maximum centred at 33°, which is characteristic of amorphous material. With increasing plasma power, diffraction peaks corresponding to the ZnO wurtzite phase appeared, indicating the coexistence of small crystalline domains in an amorphous matrix. These peaks remained broad and of low intensity, indicating the presence of nanocrystals (~ 5 nm) with random orientation. A remarkable improvement in crystallinity was observed at 200 W,

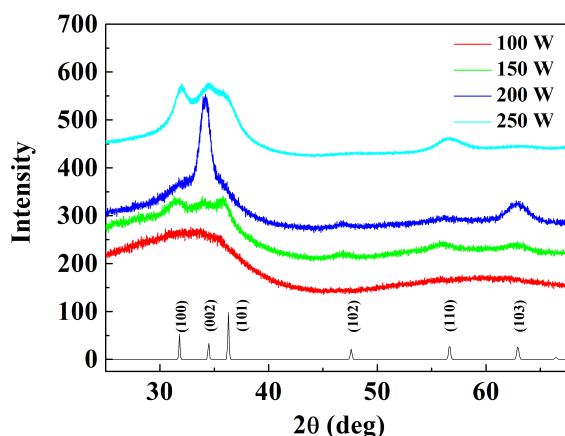


**Figure 5.24:** GIXRD patterns of ZnO films deposited at room temperature with different plasma RF powers.

with more intense diffraction peaks and a pronounced (001) texture, indicating a preferential c-axis orientation perpendicular to the substrate surface. However, a further increase in power to 250 W resulted in a decrease in crystallinity, shown by broader and less intense peaks, indicating a mixture of disordered and crystalline phases.

HRTEM images supported these observations (Fig. 5.25). Elemental analysis confirmed ZnO composition in all samples, though quantification was complicated by the presence of epoxy and silicon. At 100 W, the films were fully amorphous (Fig. 5.25a), while those deposited at 250 W consisted of nanoscale grains ( $4 \pm 1$  nm), confirming improved crystallinity (Fig. 5.25c). Electron diffraction patterns showed no distinct rings at low power (Fig. 5.25b), whereas a clear ring pattern at 250 W confirmed the formation of nanocrystalline wurtzite ZnO (Fig. 5.25d). The uniform ring intensity suggested a random distribution of crystal orientations.

This transition from the amorphous to the nanocrystalline state with increasing RF power is attributed to increased plasma reactivity. Compared to direct CCP-PEALD, where ion bombardment promotes crystallisation even at lower powers (e.g. 30 W as reported by Pilz et al. [67]), remote CCP-PEALD (used in this study) requires higher plasma powers to achieve similar crystallinity due to the lack of direct ion exposure. In contrast to the (100) orientation observed by Pilz et al., our films at higher powers predominantly exhibited a (002) texture, emphasising the crucial role of plasma configuration in growth orientation.

The formation of ultrafine ZnO grains ( $\sim 4$  nm) can also lead to quantum confinement effects, which can influence optical and electronic properties, including photocatalytic behaviour.

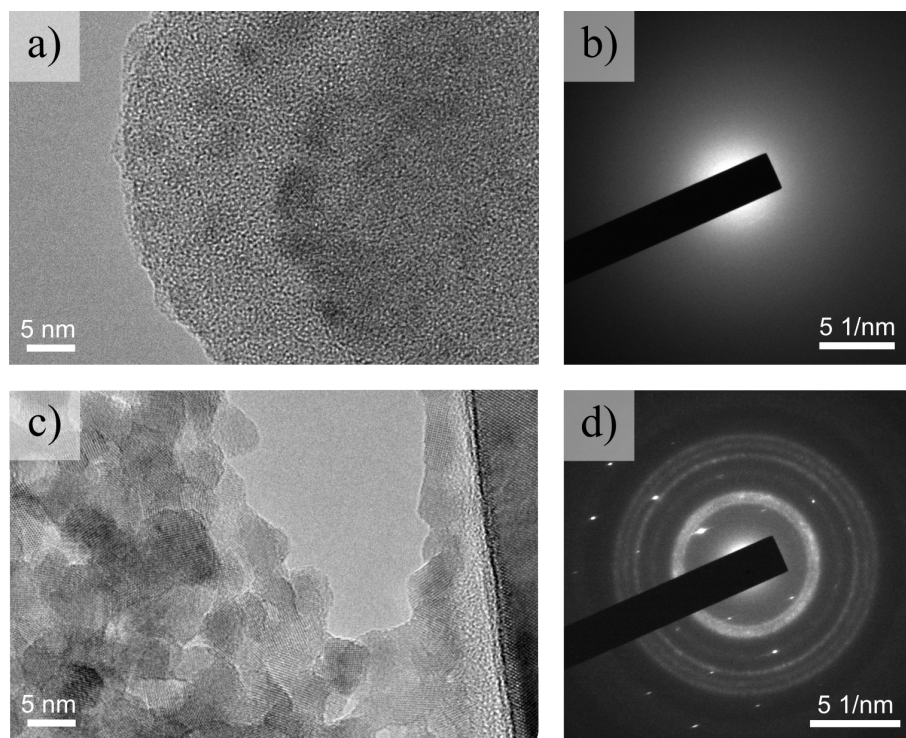


**Figure 5.25:** High-resolution TEM images of PEALD-ZnO films deposited at different RF powers: 250 W (a) and 100 W (c), with corresponding electron diffraction (SAED) patterns (b) and (d).

The chemical stability and composition of the films were analysed using XPS. While the Zn  $2p_{3/2}$  peaks remained the same for all samples, the O 1s region showed considerable differences (Fig.5.26). Two distinct peaks were observed: a dominant one at  $530.7 \pm 0.1$  eV attributed to photoemission from  $O^{2-}$  in the ZnO wurtzite structure [126, 127], and a second peak with  $\sim 1.6$  eV higher binding energy associated with non-stoichiometric oxygen [127, 131]. In conventional ALD with DEZ and  $H_2O$ , this secondary signal is usually associated with OH-related species [29, 126]. In PEALD with  $O_2$  plasma, however, such OH contamination is unlikely. Instead, the increased intensity of this peak at lower RF powers indicates a higher concentration of non-stoichiometric oxygen species and interstitials, which is consistent with the amorphous structure observed at these powers.

To further verify ZnO formation, the modified Auger parameter was calculated by adding up the Zn  $2p_{3/2}$  binding energy and the Zn LMM Auger kinetic energy. The obtained values (2010.2 – 2010.5 eV) are in good alignment with literature values for ZnO [126, 141].

The UV-Vis absorption spectra (Fig. 5.27a) of the ZnO thin films showed a gradual increase in absorption below 350 nm, which is typical for amorphous semiconductors [136]. Films

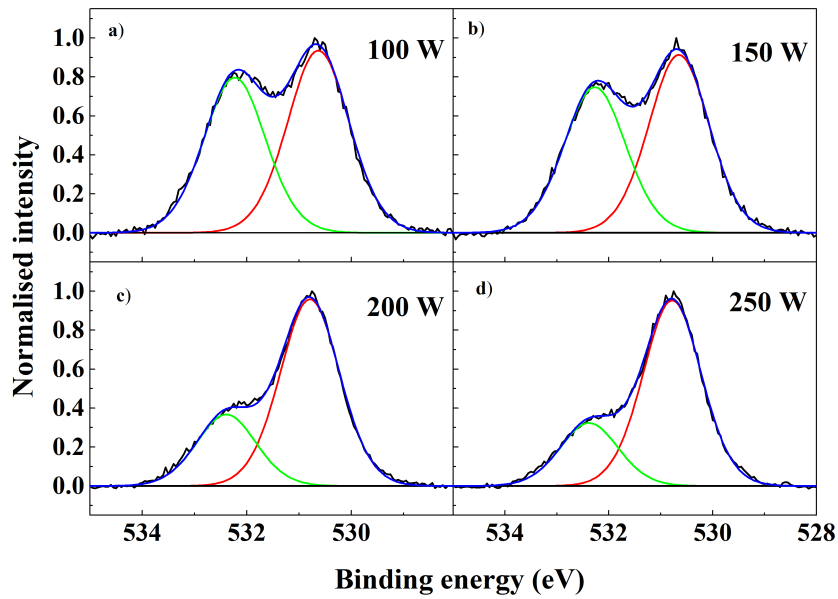


**Figure 5.26:** XPS spectra around the O 1s core-levels for the ZnO thin films deposited at room temperature.

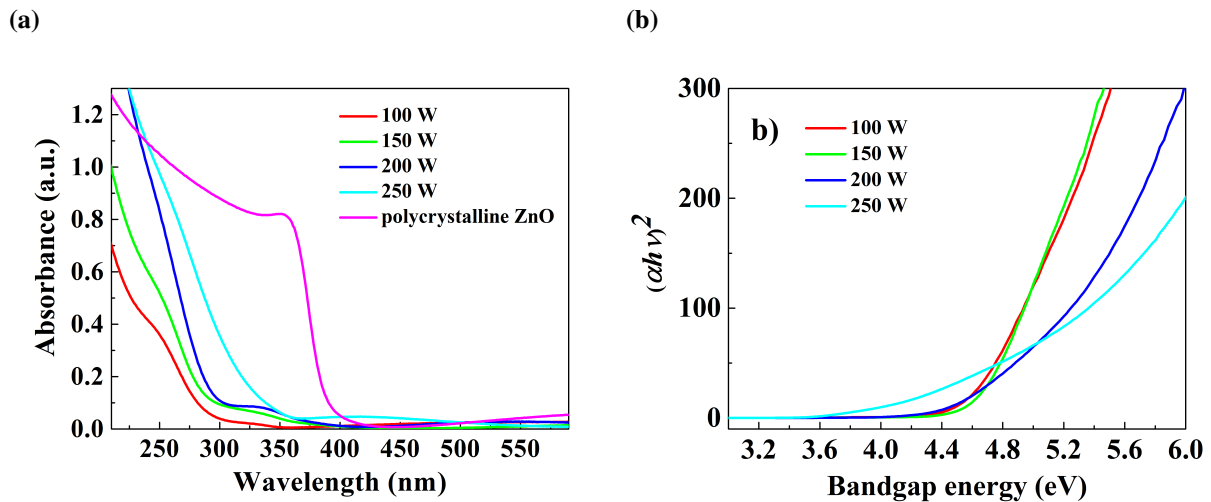


**Figure 5.27:** UV-Vis absorption spectra (a) and Tauc plot (b) of ZnO films deposited with PEALD at room temperature.

deposited with higher RF power exhibited sharper absorption edges and a red shift, indicating improved crystallinity. However, even the most crystalline film (250 W) lacked the abrupt edge seen in polycrystalline ZnO, which is likely due to grain size effects. It is noteworthy that all absorption curves showed a pronounced blue shift compared to the ZnO bulk, which can

be attributed to quantum confinement in grains smaller than 5 nm [135]. The improved UV absorption at higher plasma power indicates an improved light-harvesting potential, which is particularly advantageous for photocatalytic applications.

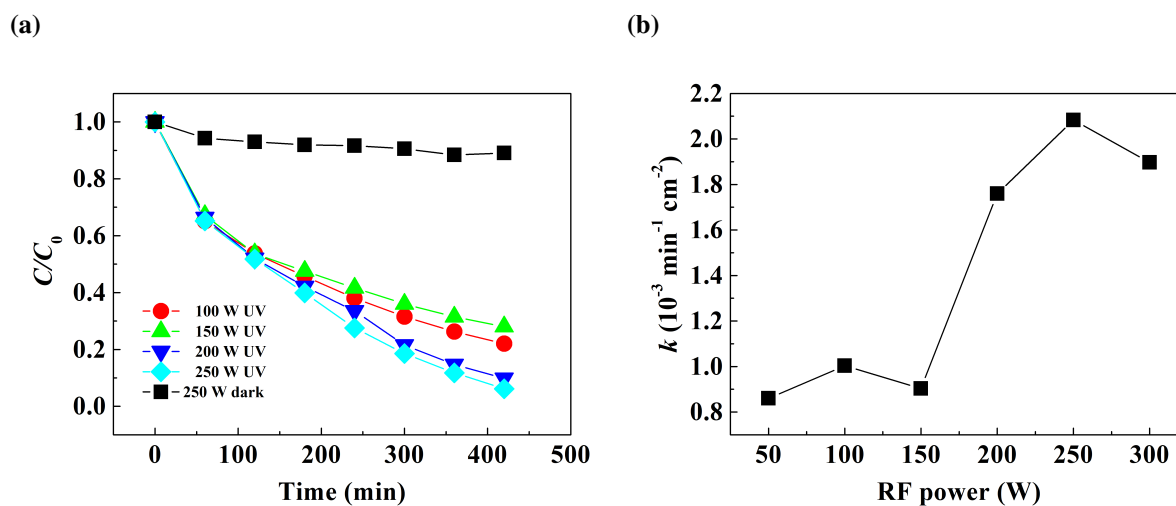


**Figure 5.28:** Photodegradation curve of MB under UV light irradiation for ZnO films deposited at room temperature with different plasma RF powers (a). Variation of the photodegradation constant as a function of the PEALD plasma RF power (b).

The photocatalytic performance improved significantly with increasing RF power (Fig. 5.28a). The film deposited at 250 W exhibited the highest photodegradation rate constant,  $k_{250 \text{ W}} = 2 \cdot 10^{-3} \text{ min}^{-1} \text{ cm}^{-2}$ , which is twice the rate of the film synthesised at 100 W ( $k_{100 \text{ W}} = 1 \cdot 10^{-3} \text{ min}^{-1} \text{ cm}^{-2}$ ). This enhanced activity is linked to better crystallinity and optical absorption, as well as improved charge carrier separation in nanocrystalline ZnO, which minimizes recombination losses.

To elucidate the dominant reactive species in the photocatalytic degradation mechanism, scavenger experiments were performed with 10 mM solutions of isopropyl alcohol (IPA), ethylenediaminetetraacetic acid disodium salt dihydrate (EDTA-2Na) and silver nitrate ( $\text{AgNO}_3$ ), targeting hydroxyl radicals ( $\text{OH}$ ), photogenerated holes ( $\text{h}^+$ ) and electrons ( $\text{e}^-$ ), respectively [142, 143, 144, 145, 146]. The photodegradation behaviour in the presence of these scavengers and the photodegradation efficiency after 120 minutes are shown in Figure 5.29.

The presence of IPA led to a significant decrease in photocatalytic efficiency, suggesting that  $\text{OH}$  radicals play a key role in the degradation process [144]. In contrast, the addition of EDTA-2Na increased the degradation rate, indicating that the recombination of holes and electrons is an

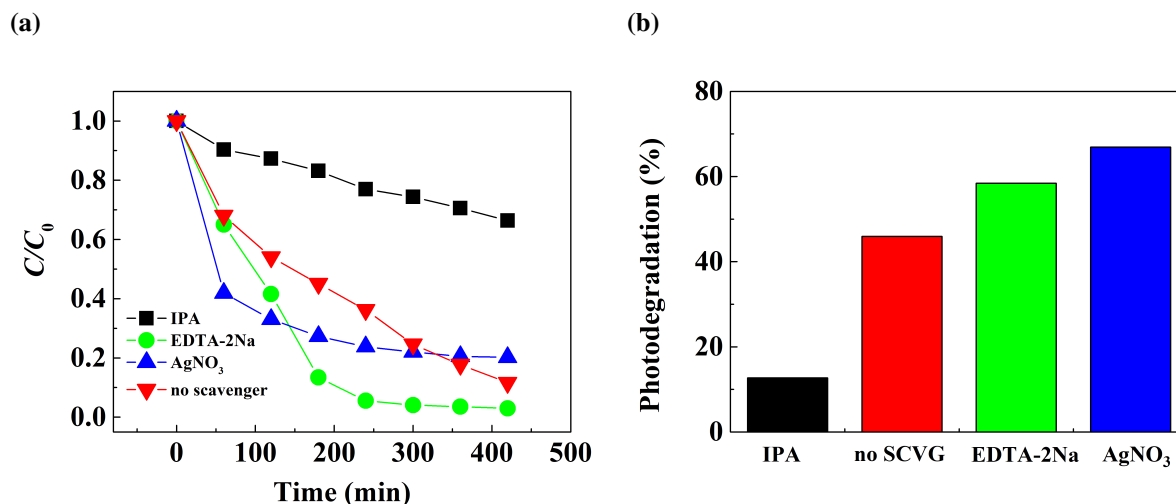


**Figure 5.29:** Photodegradation curves of MB under UV illumination in the presence of different scavengers: isopropyl alcohol (IPA), EDTA-2Na and silver nitrate ( $AgNO_3$ ) (a). Corresponding histograms showing the photodegradation efficiency of MB after 120 minutes of exposure (b).

important limiting factor in this system. By scavenging  $h^+$ , EDTA-2Na reduces recombination and thus increases the availability of electrons for redox reactions [146]. The effect of  $AgNO_3$  was more complex: while initially an improvement in degradation efficiency was observed, probably due to increased charge separation by electron capture by  $Ag^+$ , the reaction rate slowed down over time. This decrease is attributed to the formation of metallic silver nanoparticles on the catalyst surface, which can block active sites or impair light absorption, ultimately reducing photocatalytic performance [147].

## 5.5 Photodegradation of PET Microfibers

In the following section, I present the results of testing the photocatalytic efficiency of ZnO thin films in the degradation of microplastics. The section is divided into two subsections: the first focuses on the application of a ZnO thin film deposited at  $80\text{ }^\circ\text{C}$  ( $ZnO@80\text{ }^\circ\text{C}$ ) and the second with a ZnO thin film deposited at room temperature ( $ZnO@RT$ ). It is important to note that both tests were performed simultaneously to observe any visible degradation. Some experimental runs were intentionally not repeated, especially when early results indicated no significant effect for one of the photocatalysts. This approach was chosen to optimise time and resources by focusing only on the most promising conditions.

### 5.5.1 Photocatalytic Performance of Thin ZnO Films Deposited at 80 °C

As described in section 4.3.2, a thin ZnO film was applied directly to PET microfibrils. The first aim was to determine the optimal film thickness for effective photocatalytic degradation. As the photocatalytic degradation of plastics is based on the interaction between the plastic and the reactive radicals generated in the water, the first approach involved applying an ultra-thin ZnO film to the PET fibres.

In this first series of experiments, ZnO films were deposited on PET fibres at 80 °C using 0, 80, 100 and 120 PEALD cycles, corresponding to film thicknesses of 0 nm, 9 nm, 12 nm and 14 nm, respectively. After deposition, the samples were immersed in Milli-Q water and irradiated with UV light for 6 hours. As shown in Figure 5.30, no significant degradation was observed in any of the samples. These results indicate that ultra-thin ZnO films do not have sufficient catalytic activity to cause noticeable degradation within short UV irradiation durations.

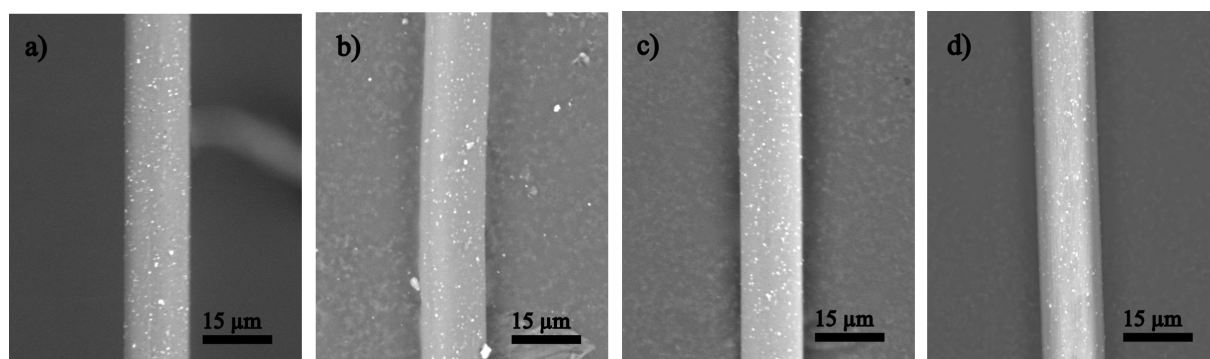


**Figure 5.30:** No significant photodegradation observed with ultra-thin ZnO@80 °C films after 6 h of UV exposure: a) 0 cycles (control sample), b) 80 cycles; c) 100 cycles; d) 120 cycles.

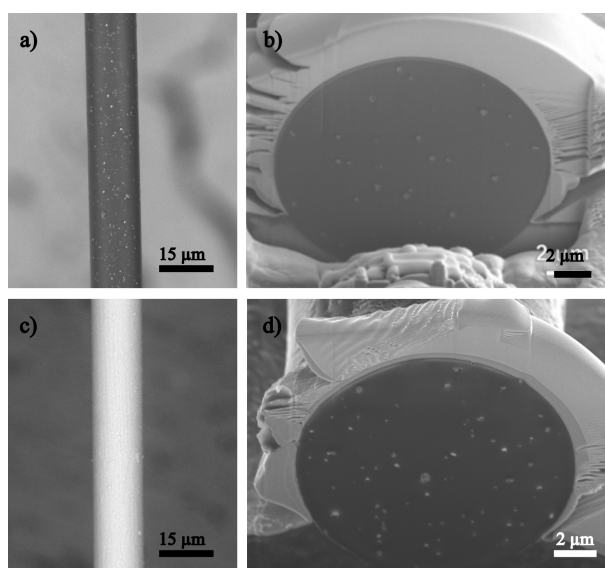


**Figure 5.31:** Surface of an untreated PET microfibre (a), PET microfibre with 360 PEALD cy of ZnO@80 °C (c). Cross-section of an untreated PET microfibre (b) and a PET microfibre with a 360 PEALD cy of thin ZnO@80 °C film.

Based on these results, the thickness of the ZnO film was increased to 360 PEALD cycles and kept constant for the rest of the experiments. Figure 5.31 shows SEM images comparing the surface morphology of untreated PET microfibres (Figure 5.31a) with that of fibres coated with a 360-cycle ZnO film deposited at 80 °C by PEALD (Figure 5.31c). Cross-sectional images taken with FIB-SEM are shown in Figures 5.31b and 5.31d for the untreated and coated fibres, respectively. The images confirm that no structural damage occurred to the PET substrate during deposition, even though it was exposed to elevated temperature and plasma.

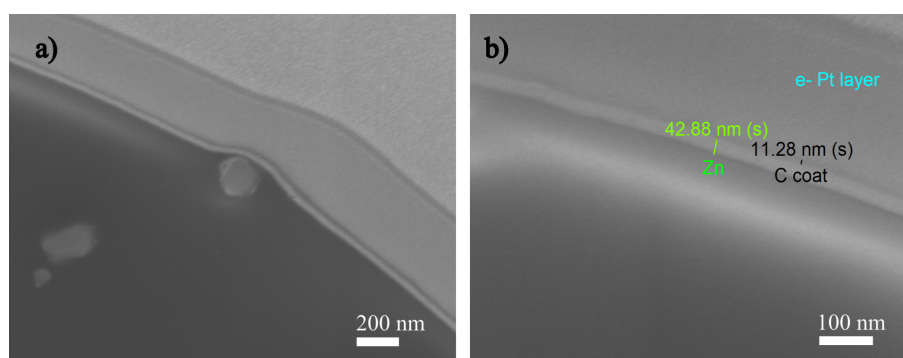


**Figure 5.32:** FIB-SEM images show the uniform deposition of ZnO films on PET substrates (a). 360 PEALD cycles at 80 °C resulted in a film thickness of 43 nm (b).

As discussed in section 2.1, the ALD film thickness can vary depending on the substrate properties. The FIB-SEM analysis shown in Figure 5.5.1 revealed that the ZnO film deposited with 360 PEALD cycles at 80 °C had a thickness of approximately 43 nm. From both SEM and FIB-SEM, the coating proved to be uniform, homogeneous and conformal on the surface of the PET fibre.

The effects of prolonged UV irradiation (48 hours) and the aqueous medium (Milli-Q water vs. tap water) on the degradation of PET microfibrils are shown in Figure 5.33. The reasons for extending the UV exposure time to 48 hours are discussed in the following section; as mentioned in the introduction, not all experiments were repeated for both catalyst.

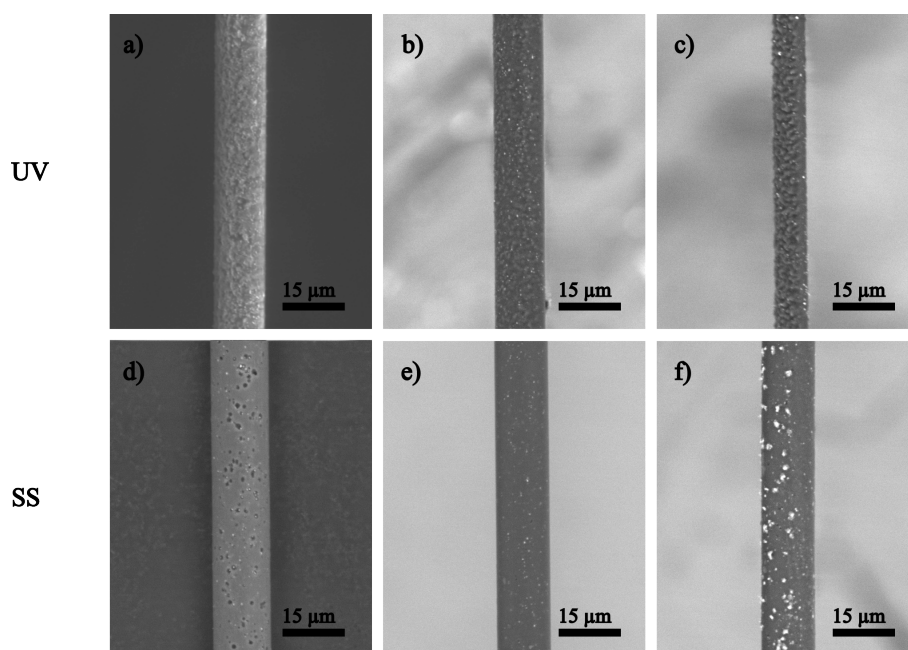


**Figure 5.33:** Photodegradation of PET microfibrils after 48 hours of exposure to UV light: without catalyst in Milli-Q water (a), with ZnO@80 °C in Milli-Q water (b), and with ZnO@80 °C in tap water (c). Photodegradation of PET microfibrils after 48 hours of exposure to simulated sunlight (SS), microfibrils without catalyst (d), with ZnO@80 °C in Milli-Q water (e), and with ZnO@80 °C in tap water (f).

In the absence of a catalyst, UV irradiation alone reduced the average fibre thickness to approximately 13.0  $\mu\text{m}$  (Figure 5.33a). When ZnO was present, degradation was more pronounced: in Milli-Q water, the fibre thickness decreased to 9.5  $\mu\text{m}$  (Figure 5.33b), while in tap water it was further reduced to 7.3  $\mu\text{m}$  (Figure 5.33c). These results suggest that the presence of ZnO enhances photocatalytic degradation and that the ionic content of tap water may further promote radical generation or surface interactions.

Under simulated sunlight, no significant degradation was observed in the absence of a catalyst, with the fibre thickness remaining at approximately  $\phi \sim 14.0 \mu\text{m}$  (Figure 5.33d). In the presence of ZnO, a slight decrease in fibre thickness was observed — down to  $\phi \sim 13.0 \mu\text{m}$  in Milli-Q water (Figure 5.33e) and  $\phi \sim 13.2 \mu\text{m}$  in tap water (Figure 5.33f). These results indicate that although ZnO slightly improves degradation under simulated sunlight, the overall photocatalytic activity remains limited compared to UV exposure.

Furthermore, the photocatalytic degradation of PET microfibres under saline conditions was investigated using a 38‰ solution of NaCl. This test was motivated by the promising results obtained in tap water and the environmental relevance of marine environments, especially in coastal regions where seawater is abundant and an environmentally friendly medium for photocatalytic applications.

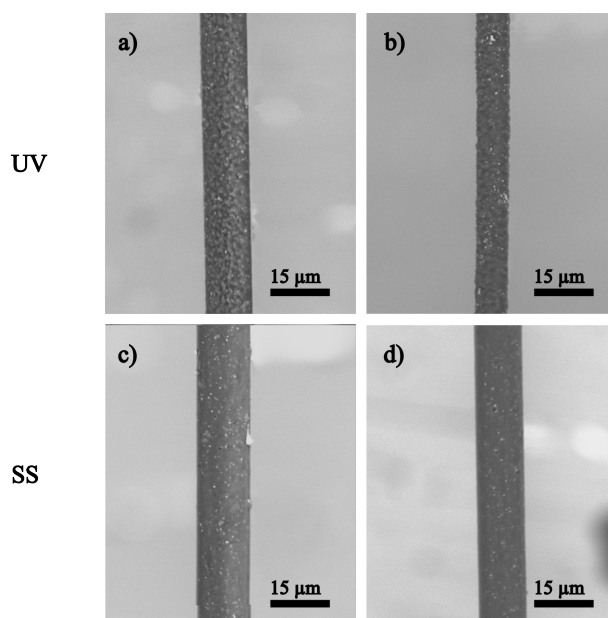


**Figure 5.34:** Photodegradation of PET microfibres in 38‰ NaCl solution after 48 hours of exposure to UV light without catalyst (a) and with ZnO@80 °C (b); and after exposure to simulated sunlight (SS) without catalyst (c) and with ZnO@80 °C (d).

Remarkable degradation was observed after 48 hours of UV irradiation: in the absence of a catalyst, the fibre thickness decreased to about  $\phi \sim 12.1 \mu\text{m}$  (Figure 5.34a), while the presence of a ZnO film deposited at 80 °C further enhanced the degradation and reduced the thickness to  $\phi \sim 8.3 \mu\text{m}$  (Figure 5.34b).

The degradation was less pronounced under simulated sunlight. The fibre thickness decreased to  $\phi \sim 13.6 \mu\text{m}$  without ZnO (Figure 5.34c) and to  $\phi \sim 10.3 \mu\text{m}$  in the presence of ZnO (Figure 5.34d).

## 5.5.2 Photocatalytic Performance of Room-Temperature ZnO Films

The photocatalytic performance of ZnO films deposited at room temperature was also investigated. Figure 5.35 shows SEM images showing the surface morphology of the PET microfibres during a series of treatment steps. Figure 5.35a shows the pristine fibre, which serves as a reference. After the deposition of 40 PEALD cycles of ZnO at room temperature, a uniform and conformal thin film formed on the fibre surface (Figure 5.35b).

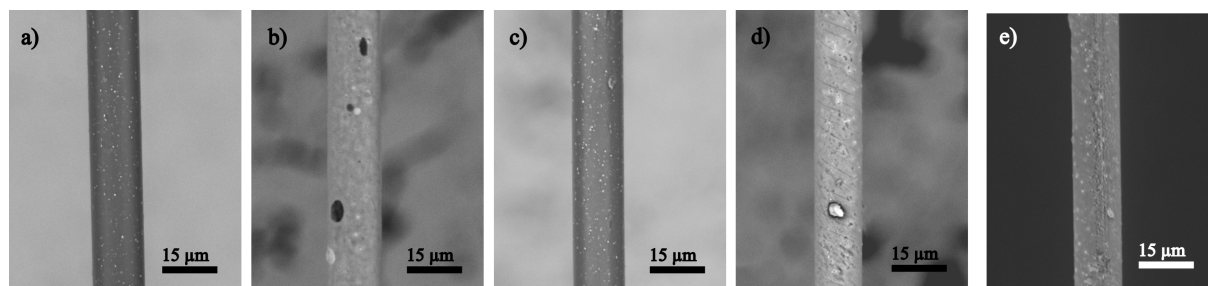


**Figure 5.35:** eSEM images of PET fibres: pristine surface (a); after 40 cycles of ZnO@RT (b); after 40 cycles of ZnO@RT and 1 h UV irradiation (c); after 40 cycles of ZnO@RT, 1 h UV and another 40 cycles of ZnO@RT (d); after two sequential ZnO@RT (40 cycles) and 1 h UV steps (e).

Subsequent irradiation with UV light for 1 hour resulted in minor surface changes (Figure 5.35c), indicating limited photocatalytic activity at this early stage. To investigate whether the performance can be improved by sequential deposition, an additional ZnO layer was deposited after the first UV treatment. The resulting film can be seen in Figure 5.35d. After one more hour of UV illumination there is no visible degradation (Figure 5.35e). A longer exposure was not carried out as the ZnO film had completely dissolved in water. Although no clear degradation of the PET fibres was observed, the successful application of repeated deposition and irradiation steps demonstrates the potential of this method for controlled, stepwise photocatalytic degradation.

To ensure a fair comparison with the ZnO films deposited at 80 °C, longer UV exposure times and thicker ZnO coatings were also applied to the room-temperature samples. Based on previous GPC measurements on silicon substrates, it was estimated that 200 PEALD cycles deposited at

room temperature would yield a film thickness comparable to 360 cycles deposited at 80 °C. Figures 5.36a and 5.36b show the untreated PET fibre and the PET fibre coated with 200 cycles of ZnO, respectively. As previously mentioned, time variation experiments with UV irradiation were not conducted for the films deposited at 80 °C due to results observed with the room-temperature catalyst at similar thicknesses. For the room-temperature ZnO films, after 16 hours of UV exposure, only minor degradation of the fibre surface was observed, and the ZnO film remained partially intact, suggesting that the reaction was incomplete (Figure 5.36c). However,

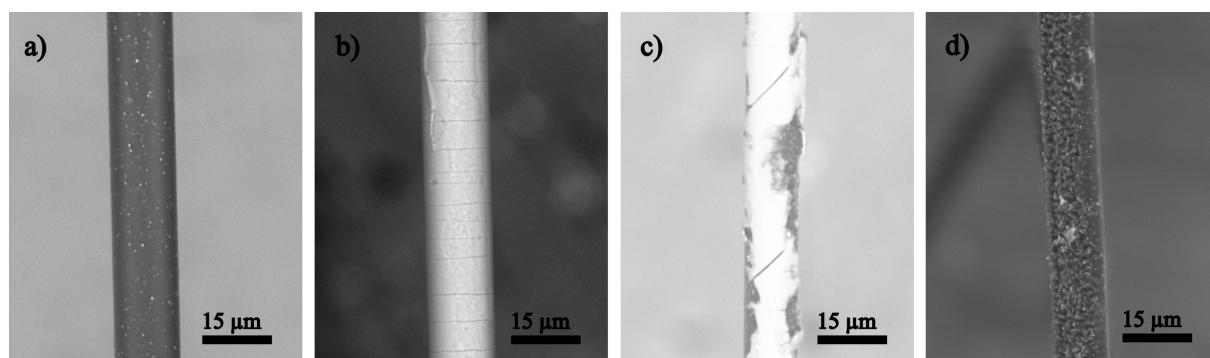


**Figure 5.36:** Photodegradation of PET microfibres: untreated PET (a); PET coated with 200 cycles of ZnO@RT (b); PET coated with 200 cycles of ZnO@RT after 16 hours of UV exposure (c); and after 48 hours of UV exposure (d).

after 48 hours of UV exposure, more pronounced surface roughening and fibre thinning occurred (Figure 5.36d), indicating that prolonged UV exposure enhances the photocatalytic degradation, even with room-temperature-deposited ZnO films. Based on these results, 48 hours of UV irradiation was chosen as the standard illumination condition for subsequent experiments.

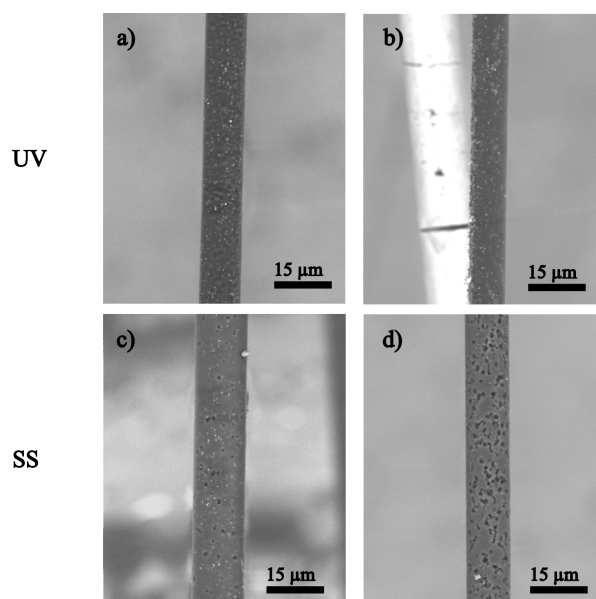


**Figure 5.37:** Photodegradation of PET microfibres in Milli-Q water with and without ZnO@RT after 48 hours of exposure to UV light without ZnO (a) and with ZnO (b); and after exposure to simulated sunlight without ZnO (c) and with ZnO (d).

The eSEM analysis of fibre degradation under UV and simulated sunlight in Milli-Q water is shown in Figure 5.37. A reduction in fibre thickness was observed in all treated samples compared to the respective controls, indicating degradation of the PET material. Under UV light, the ZnO-coated fibres exhibited a thickness of approximately  $\phi \sim 9.7 \mu\text{m}$  (Figure 5.37b), compared to for the untreated control  $\phi \sim 10.9 \mu\text{m}$  (Figure 5.37a). This reduction can be partially masked by residual ZnO material still present on the fibre surface. Under simulated sunlight, the thickness of the ZnO-coated fibres decreased to  $11.6 \mu\text{m}$  (Figure 5.37d), compared to in the control sample  $13.5 \mu\text{m}$  (Figure 5.37c).

Further structural insights into the degradation process are provided by cross-sectional analyses shown in Figure 5.38. The cross section of untreated PET fibres (Fig. 5.38a) is shown before and given here again for reference. After 48 hours of UV exposure with ZnO@RT in Milli-Q water (Fig. 5.38b), significant degradation is evident, including surface roughening and reduction in fibre diameter. Notably, the roughening is more pronounced on the upper side of the fibre, where the ZnO film was applied and directly exposed to UV light. However, the reduction in fibre diameter appears relatively uniform across the cross-section (the round geometry of the fibre was preserved). In contrast, fibre exposed to simulated sunlight with ZnO@RT in Milli-Q water (Figures 5.38c) shows only minor changes in diameter, with degradation appearing to occur



**Figure 5.38:** Cross-sectional analysis of PET fibres. Untreated PET (a, same as 5.31b); after 48 h UV exposure with ZnO@RT (b); after 48 h simulated sunlight exposure with ZnO@RT (c).

more locally. Notably, this localised degradation seems to initiate around particles embedded within the untreated PET fibre, suggesting that these inclusions may act as sites for enhanced photocatalytic or thermal activity under simulated solar conditions. Despite the surface changes, the overall fibre structure remains largely intact.

Photodegradation tests in saline environments (38 ‰ NaCl solution) are presented in Figure 5.39. UV exposure without catalyst results in moderate fibre thinning ( $\phi \sim 12.1 \mu\text{m}$ , Figure 5.39a). The presence of ZnO significantly enhances degradation ( $\phi \sim 7.9 \mu\text{m}$ , Figure 5.39b). Under simulated sunlight, the degradation is less pronounced, but the ZnO-coated sample (Fig. 5.39d) still show a minor reduction in thickness compared to control sample (Fig. 5.39c).

Overall, the results indicate that seawater in combination with UV light and ZnO films can serve as an effective and sustainable medium for the photocatalytic degradation of microplastics. Although sunlight alone may not be sufficient to achieve rapid degradation, the synergistic interaction between ZnO, sodium and chloride ions and UV irradiation represents a promising strategy for environmentally friendly plastic remediation.

Figure 5.40 illustrates the most effective photodegradation results obtained for PET under different experimental conditions: catalyst type, medium, light source and irradiation time. Under the conditions tested, ZnO deposited at 80 °C in tap water achieved the highest photodegradation rate.

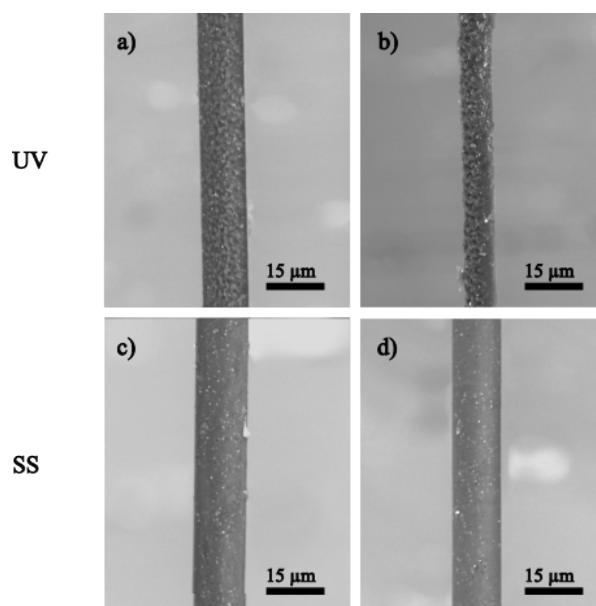


**Figure 5.39:** Photodegradation of PET microfibres in 38 ‰ NaCl solution after 48 hours of exposure to UV light without ZnO@RT (a) and with ZnO@RT (b); and after exposure to simulated sunlight without ZnO@RT (c) and with ZnO@RT (d).

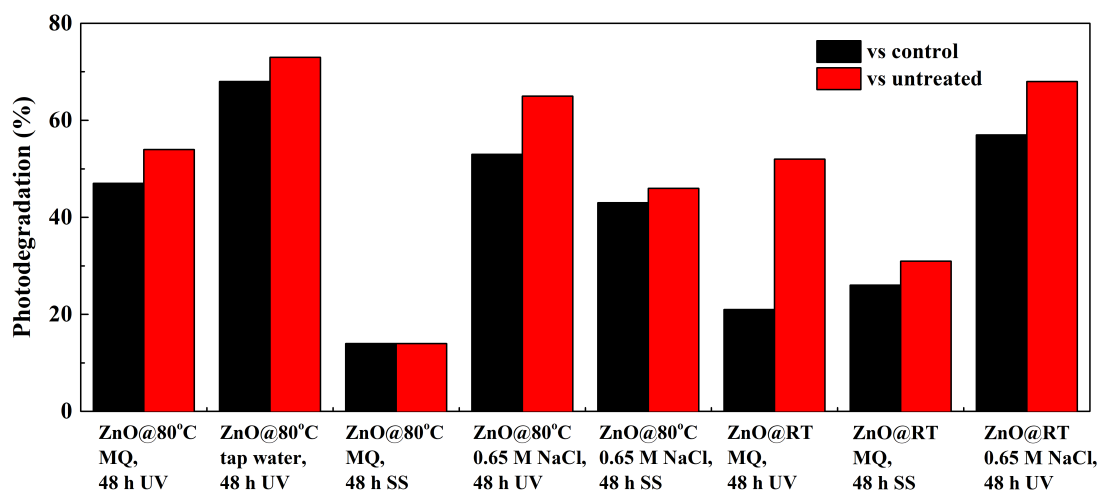


**Figure 5.40:** Histogram presenting the highest photodegradation efficiencies of PET under various experimental conditions. Each bar represents the photodegradation performance achieved for a specific set of parameters: catalyst type, medium, light source and irradiation time.

A detailed overview of all tested conditions, including the final film thicknesses and the calculated

degradation percentages, can be found in Table 5.3. The percentages of degradation were calculated in relation to untreated fibres using eq. 4.20 and with respect to control samples (ZnO-free) using eq. 4.21.

Catalyst Type	Medium	Illumination	Final Thickness	Figure	Thickness of Control <sup>1</sup>	Degradation vs Control (%)	Degradation vs Untreated (%)
80 °C, 80 cy	MQ	6 h UV	14.0	5.30a	13.9	-1%	0%
80 °C, 100 cy	MQ	6 h UV	13.6	5.30b	13.9	4%	6%
80 °C, 120 cy	MQ	6 h UV	13.8	5.30c	13.9	4%	3%
80 °C, 360 cy	MQ	48 h UV	9.5	5.33b	13.0	47%	54%
80 °C, 360 cy	tap water	48 h UV	7.3	5.33c	12.9	68%	73%
80 °C, 360 cy	MQ	48 h SUN	13.0	5.33e	14.0	14%	14%
80 °C, 360 cy	tap water	48 h SUN	13.2	5.33f	-	-	11%
80 °C, 360 cy	0.65 M NaCl	48 h UV	8.3	5.34b	12.1	53%	65%
80 °C, 360 cy	0.65 M NaCl	48 h SUN	10.3	5.34d	13.6	43%	46%
RT, 40cy	MQ	1 h UV	14.0	5.35c	14.0	0%	0%
RT, 200cy	MQ	16 h UV	12.6	5.36c	13.7	15%	19%
RT, 200cy	MQ	48 h UV	9.7	5.37b	10.9	21%	52%
RT, 200cy	MQ	48 h SUN	11.6	5.37d	13.5	26%	31%
RT, 200cy	0.65 M NaCl	48 h UV	7.9	5.39b	12.1	57%	68%
RT, 200cy	0.65 M NaCl	48 h SUN	12.9	5.39d	13.4	7%	15%

**Table 5.3:** Results of photodegradation for various catalysts in different media and under different lighting conditions.

<sup>1</sup>same conditions but without ZnO photocatalyst

## Chapter 6

# Conclusion and Future Directions

### 6.1 Summary of Findings

In this work, thin ZnO films deposited with PEALD were investigated, focusing on their photocatalytic properties in the degradation of organic pollutants, including dyes and microplastic fibres.

The comparative analysis showed that the ZnO films produced with PEALD outperformed those produced with thermal ALD. Among the different process parameters investigated, it was found that a deposition temperature of 60 °C gave the highest photocatalytic efficiency.

Importantly, research has shown that room temperature deposition is also feasible and effective, provided sufficient plasma power is used. Films deposited at room temperature with RF power above 200 W, especially 250 W, showed almost as good photocatalytic performance as films deposited at 60 °C and 50 W.

The study also confirmed the successful photocatalytic degradation of PET microfibrils with ZnO thin films. Two key parameters led to effective degradation: deposition at 80 °C with 50 W plasma power and deposition at room temperature with 250 W plasma power.

A range of experimental conditions were investigated, including different water media, film thicknesses, light sources and illumination durations. The best photocatalytic degradation was obtained in tap water and simulated seawater under 48 hours of UV irradiation with 200 cycles (room temperature) and 360 cycles (80 °C) of the coating, respectively.

Overall, this work shows that PEALD is a promising technique for the deposition of efficient photocatalytic ZnO films, especially at low and room temperatures.

## 6.2 Future directions

Based on these results, several future research directions are proposed.

Further improvements are planned with regard to the photocatalytic degradation performance of dyes and similar water-soluble substances. Firstly, the incorporation of dopants (such as N) or the formation of ZnO-based heterojunctions (e.g. ZnO/TiO) is a very interesting area of research. These strategies are used to improve charge separation, extend light absorption to the visible spectrum and increase photocatalytic activity under solar radiation.

In addition, the application of ZnO films on porous or large-surface- area substrates (e.g. anodised metal oxides) could significantly increase the available surface area for dye adsorption and reaction and thus increase the overall photocatalytic efficiency. If the porous substrate also has a suitable band gap, it could serve not only as a physical carrier but also as an active photocatalytic component. This would allow the formation of a heterojunction directly on the porous substrate.

The further development of ZnO films for the photocatalytic degradation of microplastics offers several promising research directions. The first step is to confirm the chemical degradation of the polymer fibres. Techniques such as micro-Raman spectroscopy, micro-FTIR and differential scanning calorimetry (DSC) should be used to verify structural and chemical changes within the degraded microfibrils. These methods provide complementary insights into the molecular degradation of polymers and are necessary to verify that the photocatalytic activity actually leads to chemical degradation and not just surface erosion or fragmentation.

An important strategy is to perform multiple degradation cycles on individual fibres using the most effective deposition parameters identified in this study (e.g. 80 °C and 50 W as well as room temperature and 250 W). Repeated exposure under optimised conditions could lead to more complete polymer degradation and provide valuable insights into the degradation processes.

Another promising approach is the use of porous substrates as functional photocatalytic filters. Such substrates can act both as a physical barrier that traps micro- and nanoplastic particles and as an active photocatalytic surface that facilitates their degradation. This dual functionality could prove extremely beneficial for real-world water purification applications, as physical filtration and chemical degradation can be integrated into a single system.

In addition to PET, future work should also investigate the photocatalytic degradation of other common polymeric pollutants, including polypropylene (PP), polyamide (PA) microfibrils and

plastic foils made from various polymers. Understanding the interaction of ZnO photocatalysts with a wider range of polymer types will be crucial for the development of a universal photocatalytic approach to reduce microplastics.

Finally, a crucial step in validating the environmental relevance of these results is to analyse the degradation products. It is important to assess whether the photocatalytic process leads to complete mineralisation or to the formation of potentially harmful by-products. Techniques such as ICP-MS (inductively coupled plasma mass spectrometry) could be helpful for detection and quantification degradation products.

The discovery that this method can be effectively applied to the degradation of microplastics opens up a completely new research topic.



## Bibliography

- [1] T. S. Galloway, M. Cole, C. Lewis, Interactions of microplastic debris throughout the marine ecosystem. *Nat. Ecol. Evol.* 1.5 (Apr. 2017), p. 0116. DOI: 10.1038/s41559-017-0116.
- [2] W. H. Organization, *Microplastics in drinking-water*. 2019.
- [3] W. H. Organization, *Dietary and inhalation exposure to nano- and microplastic particles and potential implications for human health*. 2022.
- [4] W. Gao, Y. Zhang, A. Mo, J. Jiang, Y. Liang, X. Cao, D. He, Removal of microplastics in water: Technology progress and green strategies. *Green Anal. Chem.* 3 (2022), p. 100042. DOI: <https://doi.org/10.1016/j.greeac.2022.100042>.
- [5] S. Kim, A. Sin, H. Nam, Y. Park, H. Lee, C. Han, Advanced oxidation processes for microplastics degradation: A recent trend. *Chem. Eng. J. Adv.* 9 (2022), p. 100213. DOI: <https://doi.org/10.1016/j.ceja.2021.100213>.
- [6] A. Sharma, P. Rao, R. Mathur, S. C. Ameta, Photocatalytic reactions of xyloidine ponceau on semiconducting zinc oxide powder. *J. Photochem. Photobiol. A: Chem* 86.1 (1995), pp. 197–200. DOI: 10.1016/1010-6030(94)03933-L.
- [7] R. Torkamani, B. Aslibeiki, Bulk ZnO, nanoparticles, nanorods and thin film: A comparative study of structural, optical and photocatalytic properties. *Journal of Crystal Growth* 618 (2023), p. 127317. DOI: <https://doi.org/10.1016/j.jcrysgr.2023.127317>.
- [8] S. F. Md Noor, S. H. Paiman, A. H. Nordin, N. Ngadi, N. A. N. Nik Malek, N. K. Abd Hamed, Solid- and aqueous-phase approaches on zinc oxide-based photocatalytic system for degradation of plastics and microplastics: A review. *Chemical Engineering Research and Design* 201 (2024), pp. 194–208. DOI: 10.1016/j.cherd.2023.11.039.

- [9] A. Haritha, M. Cruz, O. Sisman, A. Duran, D. Galusek, J. Velázquez, Y. Castro, Influence of annealing temperature on the photocatalytic efficiency of sol-gel dip-coated ZnO thin films in methyl orange degradation. *Open Ceramics* 21 (2025), p. 100727. DOI: 10.1016/j.oceram.2024.100727.
- [10] S. Mandal, R. Singha, A. Dhar, S. Ray, Optical and structural characteristics of ZnO thin films grown by rf magnetron sputtering. *Mater. Res. Bull.* 43.2 (2008), pp. 244–250. DOI: 10.1016/j.materresbull.2007.05.006.
- [11] D.-K. Kim, C.-B. Park, Deposition of ZnO thin films on Si by RF magnetron sputtering with various substrate temperatures. *J. Mater. Sci.: Mater. Electron.* 25.12 (2014), pp. 5416–5421. DOI: 10.1007/s10854-014-2322-3.
- [12] N. Pinna, M. Knez, *Atomic Layer Deposition of Nanostructured Materials*. John Wiley and Sons, Ltd, 2011, pp. I–XXXVI. DOI: 10.1002/9783527639915.fmatter.
- [13] S. M. George, Atomic Layer Deposition: An Overview. *Chem. Rev.* 110.1 (2010). PMID: 19947596, pp. 111–131. DOI: 10.1021/cr900056b.
- [14] R. W. Johnson, A. Hultqvist, S. F. Bent, A brief review of atomic layer deposition: from fundamentals to applications. *Materials Today* 17.5 (2014), pp. 236–246. DOI: 10.1016/j.mattod.2014.04.026.
- [15] Accessed: 2024-09-09.
- [16] J. A. Oke, T.-C. Jen, Atomic layer deposition and other thin film deposition techniques: from principles to film properties. *Journal of Materials Research and Technology* 21 (2022), pp. 2481–2514. DOI: 10.1016/j.jmrt.2022.10.064.
- [17] M. Leskelä, J. Niinistö, M. Ritala, 4.05 - Atomic Layer Deposition (2014). Ed. by S. Hashmi, G. F. Batalha, C. J. Van Tyne, B. Yilbas, pp. 101–123. DOI: 10.1016/B978-0-08-096532-1.00401-5.
- [18] M. Ritala, M. Leskelä, “Atomic Layer Deposition”. In: *Handbook of Thin Films Materials*. Ed. by H. Nalwa. Vol. Volume 1. United Kingdom: Academic Press, 2002, pp. 103–159.

- [19] R. L. Puurunen, W. Vandervorst, Island growth as a growth mode in atomic layer deposition: A phenomenological model. *Journal of Applied Physics* 96.12 (Dec. 2004), pp. 7686–7695. DOI: 10.1063/1.1810193.
- [20] T. Suntola, Surface chemistry of materials deposition at atomic layer level. *Appl. Surf. Sci.* 100-101 (1996), pp. 391–398. DOI: 10.1016/0169-4332(96)00306-6.
- [21] T. Justin Kunene, L. Kwanda Tartibu, K. Ukoba, T.-C. Jen, Review of atomic layer deposition process, application and modeling tools. *Mater. Today* 62 (2022). International Symposium on Nanostructured and Advanced Materials, S95–S109. DOI: 10.1016/j.matpr.2022.02.094.
- [22] L. Demelius, M. Blatnik, K. Unger, P. Parlanti, M. Gemmi, A. M. Coclite, Shedding light on the initial growth of ZnO during plasma-enhanced atomic layer deposition on vapor-deposited polymer thin films. *Applied Surface Science* 604 (2022), p. 154619. DOI: <https://doi.org/10.1016/j.apsusc.2022.154619>.
- [23] M. Tammenmaa, T. Koskinen, L. Hiltunen, L. Niinistö, M. Leskelä, Zinc chalcogenide thin films grown by the atomic layer epitaxy technique using zinc acetate as source material. *Thin Solid Films* 124.2 (1985), pp. 125–128. DOI: 10.1016/0040-6090(85)90254-8.
- [24] A. Wójcik, M. Godlewski, E. Guziewicz, R. Minikayev, W. Paszkowicz, Controlling of preferential growth mode of ZnO thin films grown by atomic layer deposition. *J. Cryst. Growth* 310.2 (2008), pp. 284–289. DOI: 10.1016/j.jcrysgro.2007.10.010.
- [25] E. Guziewicz, M. Godlewski, T. Krajewski, Wachnicki, A. Szczepanik, K. Kopalko, A. Wójcik-Głodowska, E. Przeździecka, W. Paszkowicz, E. Łusakowska, P. Kruszewski, N. Huby, G. Tallarida, S. Ferrari, ZnO grown by atomic layer deposition: A material for transparent electronics and organic heterojunctions. *J. Appl. Phys.* 105.12 (June 2009), p. 122413. DOI: 10.1063/1.3133803.
- [26] K. Kaiya, N. Yoshii, N. Takahashi, T. Nakamura, Atmospheric pressure atomic layer epitaxy of ZnO on a sapphire (0001) substrate by alternate reaction of ZnCl<sub>2</sub> and O<sub>2</sub>. *J. Mater. Sci. Lett.* 19.23 (Dec. 2000), pp. 2089–2090. DOI: 10.1023/A:1026745903387.

- [27] V. Lujala, J. Skarp, M. Tammenmaa, T. Suntola, Atomic layer epitaxy growth of doped zinc oxide thin films from organometals. *Appl. Surf. Sci.* 82-83 (1994), pp. 34–40. DOI: 10.1016/0169-4332(94)90192-9.
- [28] H. Makino, A. Miyake, T. Yamada, N. Yamamoto, T. Yamamoto, Influence of substrate temperature and Zn-precursors on atomic layer deposition of polycrystalline ZnO films on glass. *Thin Solid Films* 517.10 (2009). 7th International Conference on Coatings on Glass and Plastics (ICCG7), pp. 3138–3142. DOI: 10.1016/j.tsf.2008.11.088.
- [29] R. Peter, K. Salamon, A. Omerzu, J. Grenzer, I. J. Badovinac, I. Saric, M. Petracic, Role of Hydrogen-Related Defects in Photocatalytic Activity of ZnO Films Grown by Atomic Layer Deposition. *J. Phys. Chem. C* 124.16 (Apr. 2020), pp. 8861–8868. DOI: 10.1021/acs.jpcc.0c01519.
- [30] K. Butcher, Afifuddin, P. P.-T. Chen, M. Godlewski, A. Szczerbakow, E. Goldys, T. Tansley, J. Freitas, Recrystallization prospects for freestanding low-temperature GaN grown using ZnO buffer layers. *J. Cryst. Growth* 246.3 (2002). Proceedings of the International Workshop on Bulk Nitride Semiconductors, pp. 237–243. DOI: 10.1016/S0022-0248(02)01747-5.
- [31] *ALD database*. <https://www.atomiclimits.com/alddbatabase/>. Accessed: 2024-09-09.
- [32] J. Musschoot, “Advantages and challenges of plasma enhanced atomic layer deposition”. eng. PhD thesis. Ghent University, 2011, XX, 152 in multiple pagination + annexes.
- [33] D. Elam, E. Ortega, A. Nemashkalo, Y. Strzhemechny, A. Ayon, A. Ponce, A. A. Chabanov, Low-defect-density ZnO homoepitaxial films grown by low-temperature ALD. *Appl. Phys. Lett.* 119.14 (Oct. 2021), p. 142101. DOI: 10.1063/5.0062122.
- [34] T. Tynell, M. Karppinen, Atomic layer deposition of ZnO: a review. *Semicond. Sci. Technol.* 29.4 (Feb. 2014), p. 043001. DOI: 10.1088/0268-1242/29/4/043001.
- [35] D. D. Fong, J. A. Eastman, S. K. Kim, T. T. Fister, M. J. Highland, P. M. Baldo, P. H. Fuoss, In situ synchrotron x-ray characterization of ZnO atomic layer deposition. *Appl. Phys. Lett.* 97.19 (Nov. 2010), p. 191904. DOI: 10.1063/1.3514254.

- [36] X. Wang, S. M. Tabakman, H. Dai, Atomic Layer Deposition of Metal Oxides on Pristine and Functionalized Graphene. *Journal of the American Chemical Society* 130.26 (2008), pp. 8152–8153. DOI: 10.1021/ja8023059.
- [37] Y.-Q. Cao, J. Chen, H. Zhou, L. Zhu, X. Li, Z.-Y. Cao, D. Wu, A.-D. Li, Photocatalytic activity and photocorrosion of atomic layer deposited ZnO ultrathin films for the degradation of methylene blue. *Nanotechnology* 26.2 (Dec. 2014), p. 024002. DOI: 10.1088/0957-4484/26/2/024002.
- [38] T.-H. Jung, J.-S. Park, D.-H. Kim, Y. Jeong, S.-G. Park, J.-D. Kwon, Effect of in situ hydrogen plasma treatment on zinc oxide grown using low temperature atomic layer deposition. *J. Vac. Sci. Technol. A: Vac. Surf.* 31.1 (2013), 01A124. DOI: 10.1116/1.4767813.
- [39] S. Rehman, R. Ullah, A. Butt, N. Gohar, Strategies of making TiO<sub>2</sub> and ZnO visible light active. *J. Hazard. Mater.* 170.2 (2009), pp. 560–569. DOI: 10.1016/j.jhazmat.2009.05.064.
- [40] B. Macco, H. C. Knoop, M. A. Verheijen, W. Beyer, M. Creatore, W. M. Kessels, Atomic layer deposition of high-mobility hydrogen-doped zinc oxide. *Sol. Energy Mater. Sol. Cells* 173 (2017). Proceedings of the 7th international conference on Crystalline Silicon Photovoltaics, pp. 111–119. DOI: 10.1016/j.solmat.2017.05.040.
- [41] S. Doyle, L. Ryan, M. M. McCarthy, M. Modreanu, M. Schmidt, F. Laffir, I. M. Povey, M. E. Pemble, Combinatorial ALD for the growth of ZnO/TiO<sub>2</sub> nanolaminates and mixed ZnO/TiO<sub>2</sub> nanostructured films. *Mater. Adv.* 3 (6 2022), pp. 2896–2907. DOI: 10.1039/D1MA00726B.
- [42] E. Guziewicz, M. Godlewski, L. Wachnicki, T. A. Krajewski, G. Luka, S. Gieraltowska, R. Jakiela, A. Stonert, W. Lisowski, M. Krawczyk, J. W. Sobczak, A. Jablonski, ALD grown zinc oxide with controllable electrical properties. *Semicond. Sci. Technol.* 27.7 (June 2012), p. 074011. DOI: 10.1088/0268-1242/27/7/074011.
- [43] J. Elam, Z. Sechrist, S. George, ZnO/Al<sub>2</sub>O<sub>3</sub> nanolaminates fabricated by atomic layer deposition: growth and surface roughness measurements. *Thin Solid Films* 414.1 (2002), pp. 43–55. DOI: 10.1016/S0040-6090(02)00427-3.

- [44] R. Viter, A. A. Chaaya, I. Iatsunskyi, G. Nowaczyk, K. Kovalevskis, D. Erts, P. Miele, V. Smyntyna, M. Bechelany, Tuning of ZnO 1D nanostructures by atomic layer deposition and electrospinning for optical gas sensor applications. *Nanotechnology* 26.10 (2015), p. 105501. DOI: 10.1088/0957-4484/26/10/105501.
- [45] L. Mai, F. Mitschker, C. Bock, A. Niesen, E. Ciftiyurek, D. Rogalla, J. Mickler, M. Erig, Z. Li, P. Awakowicz, K. Schierbaum, A. Devi, From Precursor Chemistry to Gas Sensors: Plasma-Enhanced Atomic Layer Deposition Process Engineering for Zinc Oxide Layers from a Nonpyrophoric Zinc Precursor for Gas Barrier and Sensor Applications. *Small* 16.22 (2020), p. 1907506. DOI: 10.1002/sml.201907506.
- [46] X. Wang, J. Zhou, J. Song, J. Liu, N. Xu, Z. L. Wang, Piezoelectric Field Effect Transistor and Nanoforce Sensor Based on a Single ZnO Nanowire. *Nano Letters* 6.12 (2006), pp. 2768–2772. DOI: 10.1021/nl061802g.
- [47] D. M. King, X. Liang, C. S. Carney, L. F. Hakim, P. Li, A. W. Weimer, Atomic Layer Deposition of UV-Absorbing ZnO Films on SiO<sub>2</sub> and TiO<sub>2</sub> Nanoparticles Using a Fluidized Bed Reactor. *Adv. Funct. Mater.* 18.4 (2008), pp. 607–615. DOI: 10.1002/adfm.200700705.
- [48] E. Guziewicz, I. A. Kowalik, M. Godlewski, K. Kopalko, V. Osinniy, A. Wójcik, S. Yatsunencko, E. Łusakowska, W. Paszkowicz, M. Guziewicz, Extremely low temperature growth of ZnO by atomic layer deposition. *J. Appl. Phys.* 103.3 (2008), p. 033515. DOI: 10.1063/1.2836819.
- [49] B. Xia, J. Ganem, E. Briand, S. Steydli, H. Tancrez, I. Vickridge, The carbon and hydrogen contents in ALD-grown ZnO films define a narrow ALD temperature window. *Vacuum* 190 (2021), p. 110289. DOI: 10.1016/j.vacuum.2021.110289.
- [50] D. Kim, H. Kang, J.-M. Kim, H. Kim, The properties of plasma-enhanced atomic layer deposition (ALD) ZnO thin films and comparison with thermal ALD. *Appl. Surf. Sci.* 257.8 (2011), pp. 3776–3779. DOI: 10.1016/j.apsusc.2010.11.138.
- [51] A. Di Mauro, C. Farrugia, S. Abela, P. Refalo, M. Grech, L. Falqui, V. Privitera, G. Impellizzeri, Synthesis of ZnO/PMMA nanocomposite by low-temperature atomic layer

- deposition for possible photocatalysis applications. *Mater. Sci. Semicond. Process.* 118 (2020), p. 105214. DOI: <https://doi.org/10.1016/j.mssp.2020.105214>.
- [52] M. Napari, J. Malm, R. Lehto, J. Julin, K. Arstila, T. Sajavaara, M. Lahtinen, Nucleation and growth of ZnO on PMMA by low-temperature atomic layer deposition. *J. Vac. Sci. Technol. A: Vac. Surf.* 33.1 (2015), 01A128. DOI: 10.1116/1.4902326.
- [53] M. Napari, M. Lahtinen, A. Veselov, J. Julin, E. Østreng, T. Sajavaara, Room-temperature plasma-enhanced atomic layer deposition of ZnO: Film growth dependence on the PEALD reactor configuration. *Surf. Coat. Technol.* 326 (2017), pp. 281–290. DOI: 10.1016/j.surfcoat.2017.07.056.
- [54] J. Meyer, P. Görrn, S. Hamwi, H.-H. Johannes, T. Riedl, W. Kowalsky, Indium-free transparent organic light emitting diodes with Al doped ZnO electrodes grown by atomic layer and pulsed laser deposition. *Appl. Phys. Lett.* 93.7 (Aug. 2008), p. 073308. DOI: 10.1063/1.2975176.
- [55] D. R. Boris, V. D. Wheeler, N. Nepal, S. B. Qadri, S. G. Walton, C. C. R. Eddy, The role of plasma in plasma-enhanced atomic layer deposition of crystalline films. *J. Vac. Sci. Technol. A* 38.4 (2020), p. 040801. DOI: 10.1116/6.0000145.
- [56] F. F. Chen, *Capacitor tuning circuits for inductive loads*. URL: <https://www.seas.ucla.edu/~ffchen/Publs/Chen144.pdf>. (accessed: 3.3.2025.)
- [57] M. Napari, O. Tarvainen, S. Kinnunen, K. Arstila, J. Julin, Ø. S. Fjellvåg, K. Weibye, O. Nilsen, T. Sajavaara, The  $\alpha$  and  $\gamma$  plasma modes in plasma-enhanced atomic layer deposition with O<sub>2</sub>–N<sub>2</sub> capacitive discharges. *J. Phys. D: Appl. Phys.* 50.9 (2017), p. 095201. DOI: 10.1088/1361-6463/aa59b3.
- [58] P. C. Rowlette, C. G. Allen, O. B. Bromley, A. E. Dubetz, C. A. Wolden, Plasma-Enhanced Atomic Layer Deposition of Semiconductor Grade ZnO Using Dimethyl Zinc. *Chem. Vap. Depos.* 15.1-3 (2009), pp. 15–20. DOI: 10.1002/cvde.200806725.
- [59] M. Sowa, *Plasma-ALD.com: A Database for Plasma-Enhanced Atomic Layer Deposition*. Accessed: 2025-05-29.

- [60] S.-H. K. Park, C.-S. Hwang, H.-S. Kwack, J.-H. Lee, H. Y. Chu, Characteristics of ZnO Thin Films by Means of Plasma-Enhanced Atomic Layer Deposition. *J. Electrochem. Soc.* 9.10 (2006), G299. DOI: 10.1149/1.2221770.
- [61] S. J. Lim, J.-M. Kim, D. Kim, C. Lee, J.-S. Park, H. Kim, The Effects of UV Exposure on Plasma-Enhanced Atomic Layer Deposition ZnO Thin Film Transistor. *Electrochemical and Solid-State Letters* 13.5 (2010), H151. DOI: 10.1149/1.3322733.
- [62] M. A. Thomas, J. B. Cui, Highly Tunable Electrical Properties in Undoped ZnO Grown by Plasma Enhanced Thermal-Atomic Layer Deposition. *ACS Appl. Mater. Interfaces* 4.6 (2012). PMID: 22577800, pp. 3122–3128. DOI: 10.1021/am300458q.
- [63] J. Zhang, H. Yang, Q.-l. Zhang, S. Dong, J. K. Luo, Bipolar resistive switching characteristics of low temperature grown ZnO thin films by plasma-enhanced atomic layer deposition. *Appl. Phys. Lett.* 102.1 (2013), p. 012113. DOI: 10.1063/1.4774400.
- [64] J. Zhang, H. Yang, Q. long Zhang, S. Dong, J. Luo, Structural, optical, electrical and resistive switching properties of ZnO thin films deposited by thermal and plasma-enhanced atomic layer deposition. *Appl. Surf. Sci.* 282 (2013), pp. 390–395. DOI: 10.1016/j.apsusc.2013.05.141.
- [65] M.-j. Jin, J. Jo, G. P. Neupane, J. Kim, K.-S. An, J.-W. Yoo, Tuning of undoped ZnO thin film via plasma enhanced atomic layer deposition and its application for an inverted polymer solar cell. *AIP Adv.* 3.10 (2013), p. 102114. DOI: 10.1063/1.4825230.
- [66] M. Shen, T. P. Muneshwar, K. C. Cadien, Y. Y. Tsui, D. W. Barlage, ZnO Schottky Nanodiodes Processed From Plasma-Enhanced Atomic Layer Deposition at Near Room Temperature. *IEEE Transactions on Electron Devices* 65.10 (2018), pp. 4513–4519. DOI: 10.1109/TED.2018.2866598.
- [67] J. Pilz, A. Perrotta, P. Christian, M. Tazreiter, R. Resel, G. Leising, T. Griesser, A. M. Coclite, Tuning of material properties of ZnO thin films grown by plasma-enhanced atomic layer deposition at room temperature. *J. Vac. Sci. Technol. A: Vac. Surf.* 36.1 (2018), 01A109. DOI: 10.1116/1.5003334.
- [68] J. Pilz, A. Perrotta, G. Leising, A. M. Coclite, ZnO Thin Films Grown by Plasma-Enhanced Atomic Layer Deposition: Material Properties Within and Outside the “Atomic

- Layer Deposition Window”. *Phys. Status Solidi A* 217.8 (2020), p. 1900256. DOI: 10.1002/pssa.201900256.
- [69] J. R. Castillo-Saenz, N. Nedev, B. Valdez-Salas, M. A. Martinez-Puente, F. S. Aguirre-Tostado, M. I. Mendivil-Palma, D. Mateos, M. A. Curiel-Alvarez, O. Perez-Landeros, E. Martinez-Guerra, Growth of ZnO thin films at low temperature by plasma-enhanced atomic layer deposition using H<sub>2</sub>O and O<sub>2</sub> plasma oxidants. *J. Mater. Sci.: Mater. Electron.* 32.15 (Aug. 2021), pp. 20274–20283. DOI: 10.1007/s10854-021-06533-x.
- [70] S. R. Morrison, T. Freund, Chemical Role of Holes and Electrons in ZnO Photocatalysis. *The Journal of Chemical Physics* 47.4 (Aug. 1967), pp. 1543–1551. DOI: 10.1063/1.1712115.
- [71] J. Schneider, D. Bahnemann, J. Ye, G. Li Puma, D. D. Dionysiou, J. Schneider, D. Bahnemann, J. Ye, G. Li Puma, D. D. Dionysiou, *Photocatalysis: Fundamentals and Perspectives*. The Royal Society of Chemistry, Mar. 2016. DOI: 10.1039/9781782622338.
- [72] S. Chu, B. Zhang, X. Zhao, H. S. Soo, F. Wang, R. Xiao, H. Zhang, Photocatalytic Conversion of Plastic Waste: From Photodegradation to Photosynthesis. *Advanced Energy Materials* 12.22 (2022), p. 2200435. DOI: 10.1002/aenm.202200435.
- [73] S. Kahng, H. Yoo, J. H. Kim, Recent advances in earth-abundant photocatalyst materials for solar H<sub>2</sub> production. *Advanced Powder Technology* 31.1 (2020), pp. 11–28. DOI: <https://doi.org/10.1016/j.appt.2019.08.035>.
- [74] X. Yang, D. Wang, Photocatalysis: From Fundamental Principles to Materials and Applications. *ACS Appl. Energy Mater.* 1.12 (2018), pp. 6657–6693. DOI: 10.1021/acsaem.8b01345.
- [75] U. Özgür, Y. I. Alivov, C. Liu, A. Teke, M. A. Reshchikov, S. Doğan, V. Avrutin, S.-J. Cho, H. Morkoç, A comprehensive review of ZnO materials and devices. *J. Appl. Phys.* 98.4 (2005), p. 041301. DOI: 10.1063/1.1992666.
- [76] Y. Huang, S. S. H. Ho, Y. Lu, R. Niu, L. Xu, J. Cao, S. Lee, Removal of Indoor Volatile Organic Compounds via Photocatalytic Oxidation: A Short Review and Prospect. en. *Molecules* 21.1 (Jan. 2016), p. 56.

- [77] A. Fujishima, K. Honda, Electrochemical Photolysis of Water at a Semiconductor Electrode. *Nature* 238.5358 (1972), pp. 37–38. DOI: 10.1038/238037a0.
- [78] A. Di Mauro, M. E. Fragalà, V. Privitera, G. Impellizzeri, ZnO for application in photocatalysis: From thin films to nanostructures. *Mater. Sci. Semicond* 69 (2017). ZnO-based materials and applications, pp. 44–51. DOI: 10.1016/j.mssp.2017.03.029.
- [79] R. Radičić, A. Jurov, J. Zavašnik, J. Kovač, V. Brusar, S. Vdović, D. Novko, N. Krstulović, UV and solar-driven photocatalysis of organic dyes using ZnO-Ag hetero-junction nanoparticles synthesized by one-step laser synthesis in water. *Applied Surface Science* 669 (2024), p. 160498. DOI: <https://doi.org/10.1016/j.apsusc.2024.160498>.
- [80] P. Seleš, D. Vengust, T. Radošević, M. Kocijan, L. Einfalt, M. Kurtjak, V. Shvalya, T. Knaflič, S. Bernik, A. Omerzu, M. Podlogar, Altering defect population during the solvothermal growth of ZnO nanorods for photocatalytic applications. *Ceramics International* 50.15 (2024), pp. 26819–26828. DOI: 10.1016/j.ceramint.2024.04.410.
- [81] D. A. Karajz, I. M. Szilágyi, Review of photocatalytic ZnO nanomaterials made by atomic layer deposition. *Surf. Interfaces* 40 (2023), p. 103094. DOI: 10.1016/j.surfin.2023.103094.
- [82] S. Mežnarić, I. Jelovica Badovinac, I. Šarić, R. Peter, M. Kolymjadi Markovic, G. Ambrožič, I. Gobin, Superior UVA-photocatalytic antibacterial activity of a double-layer ZnO/Al<sub>2</sub>O<sub>3</sub> thin film grown on cellulose by atomic layer deposition (ALD). *Journal of Environmental Chemical Engineering* 10.3 (2022), p. 108095. DOI: 10.1016/j.jece.2022.108095.
- [83] R. Peter, A. Omerzu, I. Kavre Piltaver, R. Speranza, K. Salamon, M. Podlogar, K. Velican, M. Percic, M. Petrvacic, Large enhancement of visible light photocatalytic efficiency of ZnO films doped in-situ by copper during atomic layer deposition growth. *Ceramics International* 49.22, Part A (2023), pp. 35229–35238. DOI: <https://doi.org/10.1016/j.ceramint.2023.08.196>.
- [84] Y. He, A. U. Rehman, M. Xu, C. A. Not, A. M. Ng, A. B. Djurišić, Photocatalytic degradation of different types of microplastics by TiO<sub>x</sub>/ZnO tetrapod photocatalysts. *Heliyon* 9.11 (2023), e22562. DOI: 10.1016/j.heliyon.2023.e22562.

- [85] V. Miikkulainen, M. Leskelä, M. Ritala, R. L. Puurunen, Crystallinity of inorganic films grown by atomic layer deposition: Overview and general trends. *Journal of Applied Physics* 113.2 (Jan. 2013), p. 021301. DOI: 10.1063/1.4757907.
- [86] M. Polat Gonullu, M. Soyleyici Cergel, H. I. Efker, H. Ates, Investigations of some physical properties of ALD growth ZnO films: effect of crystal orientation on photocatalytic activity. *J. Mater. Sci.: Mater. Electron.* 32.9 (May 2021), pp. 12059–12074. DOI: 10.1007/s10854-021-05835-4.
- [87] A. L. Rudd, C. B. Breslin, Photo-induced dissolution of zinc in alkaline solutions. *Electrochimica Acta* 45.10 (2000), pp. 1571–1579. DOI: 10.1016/S0013-4686(99)00322-9.
- [88] C. Belver, J. Bedia, A. Gómez-Avilés, M. Peñas-Garzón, J. J. Rodriguez, “Chapter 22 - Semiconductor Photocatalysis for Water Purification”. In: *Nanoscale Materials in Water Purification*. Ed. by S. Thomas, D. Pasquini, S.-Y. Leu, D. A. Gopakumar. Micro and Nano Technologies. Elsevier, 2019, pp. 581–651. DOI: 10.1016/B978-0-12-813926-4.00028-8.
- [89] M. Sarma, M. K. Jaiswal, S. Podder, J. Bora, S. Karmakar, B. Choudhury, A. R. Pal, A study on the applicability of thin film over powder for visible light photocatalysis. *Physica B: Condensed Matter* 670 (2023), p. 415354. DOI: <https://doi.org/10.1016/j.physb.2023.415354>.
- [90] S. Sampath, M. Shestakova, P. Maydannik, T. Ivanova, T. Homola, A. Bryukvin, M. Sillanpää, R. Nagumothu, V. Alagan, Photoelectrocatalytic activity of ZnO coated nanoporous silicon by atomic layer deposition. *RSC Adv.* 6 (30 2016), pp. 25173–25178. DOI: 10.1039/C6RA01655C.
- [91] B. Chen, J. Zhang, J. Yu, R. wang, B. He, J. Jin, H. Wang, Y. Gong, Rational design of all-solid-state TiO<sub>2</sub>-x/Cu/ZnO Z-scheme heterojunction via ALD-assistance for enhanced photocatalytic activity. *Journal of Colloid and Interface Science* 607 (2022), pp. 760–768. DOI: <https://doi.org/10.1016/j.jcis.2021.09.023>.
- [92] A. Ghobadi, T. G. Ulusoy, R. Garifullin, M. O. Guler, A. K. Okyay, A Heterojunction Design of Single Layer Hole Tunneling ZnO Passivation Wrapping around TiO<sub>2</sub>Nanowires

- for Superior Photocatalytic Performance. *Scientific Reports* 6.1 (2016), p. 30587. DOI: 10.1038/srep30587.
- [93] E. Jang, D. W. Kim, S. H. Hong, Y. M. Park, T. J. Park, Visible light-driven g-C<sub>3</sub>N<sub>4</sub>@ZnO heterojunction photocatalyst synthesized via atomic layer deposition with a specially designed rotary reactor. *Applied Surface Science* 487 (2019), pp. 206–210. DOI: <https://doi.org/10.1016/j.apsusc.2019.05.035>.
- [94] R. Al-Tohamy, S. S. Ali, F. Li, K. M. Okasha, Y. A.-G. Mahmoud, T. Elsamahy, H. Jiao, Y. Fu, J. Sun, A critical review on the treatment of dye-containing wastewater: Ecotoxicological and health concerns of textile dyes and possible remediation approaches for environmental safety. *Ecotoxicol. Environ. Saf.* 231 (2022), p. 113160. DOI: 10.1016/j.ecoenv.2021.113160.
- [95] I. Khan, K. Saeed, I. Zekker, B. Zhang, A. H. Hendi, A. Ahmad, S. Ahmad, N. Zada, H. Ahmad, L. A. Shah, T. Shah, I. Khan, Review on Methylene Blue: Its Properties, Uses, Toxicity and Photodegradation. *Water* 14.2 (2022). DOI: 10.3390/w14020242.
- [96] A. Chithambararaj, N. S. Sanjini, A. C. Bose, S. Velmathi, Flower-like hierarchical h-MoO<sub>3</sub>: new findings of efficient visible light driven nano photocatalyst for methylene blue degradation. *Catal. Sci. Technol.* 3 (5 2013), pp. 1405–1414. DOI: 10.1039/C3CY20764A.
- [97] E. Rashid, S. M. Hussain, S. Ali, M. Munir, A. Ghafoor, E. Yilmaz, M. A. Alshehri, D. Riaz, A. Naeem, E. Naeem, Impacts of microplastic accumulation in aquatic environment: Physiological, eco-toxicological, immunological, and neurotoxic effects. *Aquatic Toxicology* 279 (2025), p. 107232. DOI: <https://doi.org/10.1016/j.aquatox.2024.107232>.
- [98] J. Chen, J. Wu, P. C. Sherrell, J. Chen, H. Wang, W.-x. Zhang, J. Yang, How to Build a Microplastics-Free Environment: Strategies for Microplastics Degradation and Plastics Recycling. *Advanced Science* 9.6 (2022), p. 2103764. DOI: <https://doi.org/10.1002/adv.202103764>.
- [99] M. Eriksen, L. C. M. Lebreton, H. S. Carson, M. Thiel, C. J. Moore, J. C. Borerro, F. Galgani, P. G. Ryan, J. Reisser, Plastic Pollution in the World's Oceans: More than 5

- Trillion Plastic Pieces Weighing over 250,000 Tons Afloat at Sea. *PLoS ONE* 9.12 (Dec. 2014), pp. 1–15. DOI: 10.1371/journal.pone.0111913.
- [100] C. M. Rochman, E. Hoh, T. Kurobe, S. J. Teh, Ingested plastic transfers hazardous chemicals to fish and induces hepatic stress. *Sci. Rep.* 3.1 (Nov. 2013), p. 3263. DOI: 10.1038/srep03263.
- [101] N. Chartres, C. B. Cooper, G. Bland, K. E. Pelch, S. A. Gandhi, A. BakenRa, T. J. Woodruff, Effects of Microplastic Exposure on Human Digestive, Reproductive, and Respiratory Health: A Rapid Systematic Review. *Environmental Science and Technology* 58.52 (2024). PMID: 39692326, pp. 22843–22864. DOI: 10.1021/acs.est.3c09524.
- [102] N. A. Razali, W. R. W. Abdullah, N. M. Zikir, Effect of Thermo-Photocatalytic Process Using Zinc Oxide on Degradation of Macro/Micro-Plastic in Aqueous Environment. *Journal of Sustainability Science and Management* 15.6 (2020). Submitted: 19 January 2020; Accepted: 20 February 2020, pp. 1–14. DOI: 10.46754/jssm.2020.08.001.
- [103] A. Kumar, S. Kumar, L. Singh, *Plastic Degradation and Conversion by Photocatalysis: A Sustainable Approach*. Vol. 1. ACS Symposium Series. American Chemical Society, 2024. DOI: 10.1021/bk-2024-1489.
- [104] Z. Cheng, B. Guan, J. Wang, Y. Zhang, N. Li, Y. Sun, B. Yan, G. Chen, *Application of photocatalytic technology in the treatment and disposal of waste plastics: a review*. 2025. DOI: 10.48130/prkm-0025-0002.
- [105] IMARC Group, *Polyethylene Terephthalate (PET) Fabric Market Report by Source, Fabric Type, Form, Application, and Region 2025-2033*. <https://www.imarcgroup.com/polyethylene-terephthalate-fabric-market>. Accessed: 2025-05-27. 2025.
- [106] F. B. Marcotte, D. Campbell, J. A. Cleaveland, D. T. Turner, Photolysis of poly(ethylene terephthalate). *Journal of Polymer Science Part A-1: Polymer Chemistry* 5.3 (1967), pp. 481–501. DOI: 10.1002/pol.1967.150050308.
- [107] T. Sang, C. J. Wallis, G. Hill, G. J. Britovsek, Polyethylene terephthalate degradation under natural and accelerated weathering conditions. *European Polymer Journal* 136 (2020), p. 109873. DOI: 10.1016/j.eurpolymj.2020.109873.

- [108] V. Dhaka, S. Singh, A. G. Anil, T. S. Sunil Kumar Naik, S. Garg, J. Samuel, M. Kumar, P. C. Ramamurthy, J. Singh, Occurrence, toxicity and remediation of polyethylene terephthalate plastics. A review. en. *Environ Chem Lett* 20.3 (Jan. 2022), pp. 1777–1800.
- [109] T. Muringayil Joseph, S. Azat, Z. Ahmadi, O. Moini Jazani, A. Esmaeili, E. Kianfar, J. Haponiuk, S. Thomas, Polyethylene terephthalate (PET) recycling: A review. *Case Studies in Chemical and Environmental Engineering* 9 (2024), p. 100673. DOI: <https://doi.org/10.1016/j.cscee.2024.100673>.
- [110] Y. Wan, H. Wang, J. Liu, X. Liu, X. Song, W. Zhou, J. Zhang, P. Huo, Enhanced degradation of polyethylene terephthalate plastics by CdS/CeO<sub>2</sub> heterojunction photocatalyst activated peroxymonosulfate. *Journal of Hazardous Materials* 452 (2023), p. 131375. DOI: <https://doi.org/10.1016/j.jhazmat.2023.131375>.
- [111] M. C. Ariza-Tarazona, C. Siligardi, H. A. Carreón-López, J. E. Valdéz-Cerda, P. Pozzi, G. Kaushik, J. F. Villarreal-Chiu, E. I. Cedillo-González, Low environmental impact remediation of microplastics: Visible-light photocatalytic degradation of PET microplastics using bio-inspired C,N-TiO<sub>2</sub>/SiO<sub>2</sub> photocatalysts. *Marine Pollution Bulletin* 193 (2023), p. 115206. DOI: <https://doi.org/10.1016/j.marpolbul.2023.115206>.
- [112] P.-Y. Lu, L. A. Ningsih, A. C. Heksa, C.-C. Hu, W.-C. Chen, Y.-C. Chiu, Solid Base-Assisted Photocatalytic Degradation of Polyethylene via the Norrish Mechanism through the Generation of Alternating Polyketones. *Polymer Journal* 57 (2025). Received: 26 July 2024; Revised: 20 November 2024; Accepted: 25 November 2024; Published online: 17 January 2025, pp. 575–586. DOI: 10.1038/s41428-024-01009-1.
- [113] D. Zhou, H. Luo, F. Zhang, J. Wu, J. Yang, H. Wang, Efficient Photocatalytic Degradation of the Persistent PET Fiber-Based Microplastics over Pt Nanoparticles Decorated N-Doped TiO<sub>2</sub> Nanoflowers. *Advanced Fiber Materials* 4.5 (2022), pp. 1094–1107. DOI: 10.1007/s42765-022-00149-4.
- [114] C. Kittel, *Introduction to Solid State Physics*. 8th ed. Wiley, 2004.
- [115] B. Gil, *Physics of Wurtzite Nitrides and Oxides: Passport to Devices*. 1st ed. Springer Series in Materials Science No. 197. Springer, 2014.

- [116] A. F. Abdulrahman, A. A. Barzinjy, S. M. Hamad, M. A. Almessiere, Impact of Radio Frequency Plasma Power on the Structure, Crystallinity, Dislocation Density, and the Energy Band Gap of ZnO Nanostructure. *ACS Omega* 6.47 (2021), pp. 31605–31614. doi: 10.1021/acsomega.1c04105.
- [117] R. W. G. Wyckoff, R. W. Wyckoff, *Crystal structures*. Vol. 1. Interscience publishers New York, 1963.
- [118] Increasing the international visibility of the Rijeka Laboratory for Scanning Electron Microscopy - POMERI, Project webpage, *Laboratory Equipment*. Accessed: 2025-04-23. 2025.
- [119] *Electron Spectroscopy of Surfaces*. <https://www.ph.tum.de/academics/org/labs/fopra/docs/userguide-35.en.pdf>. Accessed: 2021-11-24.
- [120] J. Moulder, J. Chastain, *Handbook of X-ray Photoelectron Spectroscopy: A Reference Book of Standard Spectra for Identification and Interpretation of XPS Data*. Physical Electronics Division, Perkin-Elmer Corporation, 1992.
- [121] C. D. Wagner, W. M. Riggs, L. E. Davis, G. F. Moulder, *Handbook of X-ray Photoelectron Spectroscopy*. Minnesota: Perkin-Elmer Corporation, 1979.
- [122] P. van der Heide, *Secondary Ion Mass Spectrometry: An Introduction to Principles and Practices*. Wiley, 2014.
- [123] LibreTexts, *10.6: Photoluminescence Spectroscopy*. [https://chem.libretexts.org/Courses/Northeastern\\_University/10%3A\\_Spectroscopic\\_Methods/10.6%3A\\_Photoluminescence\\_Spectroscopy](https://chem.libretexts.org/Courses/Northeastern_University/10%3A_Spectroscopic_Methods/10.6%3A_Photoluminescence_Spectroscopy). Accessed: 2021-12-01.
- [124] R. Wang, K. Hashimoto, A. Fujishima, M. Chikuni, E. Kojima, A. Kitamura, M. Shimohigoshi, T. Watanabe, Light-induced amphiphilic surfaces. *Nature* 388.6641 (July 1997), pp. 431–432. doi: 10.1038/41233.
- [125] M. A. Thomas, J. Cui, The Effects of an O<sub>2</sub> Plasma on the Optical Properties of Atomic Layer Deposited ZnO. *ECS Trans.* 45.7 (Apr. 2012), p. 87. doi: 10.1149/1.3701529.
- [126] V. Rogé, N. Bahlawane, G. Lamblin, I. Fechete, F. Garin, A. Dinia, D. Lenoble, Improvement of the photocatalytic degradation property of atomic layer deposited ZnO

- thin films: the interplay between film properties and functional performances. *J. Mater. Chem. A* 3 (21 2015), pp. 11453–11461. doi: 10.1039/C5TA01637A.
- [127] M. Krzywiecki, L. Grządziel, A. Sarfraz, D. Iqbal, A. Sz wajca, A. Erbe, Zinc oxide as a defect-dominated material in thin films for photovoltaic applications – experimental determination of defect levels, quantification of composition, and construction of band diagram. *Phys. Chem. Chem. Phys.* 17 (15 2015), pp. 10004–10013. doi: 10.1039/C5CP00112A.
- [128] A. Di Mauro, M. Cantarella, G. Nicotra, V. Privitera, G. Impellizzeri, Low temperature atomic layer deposition of ZnO: Applications in photocatalysis. *Appl. Catal. B* 196 (2016), pp. 68–76. doi: 10.1016/j.apcatb.2016.05.015.
- [129] T. Muneshwar, G. Shoute, D. Barlage, K. Cadien, Plasma enhanced atomic layer deposition of ZnO with diethyl zinc and oxygen plasma: Effect of precursor decomposition. *J. Vac. Sci. Technol. A: Vac. Surf.* 34.5 (2016), p. 050605. doi: 10.1116/1.4961885.
- [130] Joint Committee on Powder Diffraction Standards (JCPDS), *Powder Diffraction File, Card No. 01-089-1397*. Accessed through Powder Diffraction File database. International Centre for Diffraction Data, n.d.
- [131] D. Chen, D. He, J. Lu, L. Zhong, F. Liu, J. Liu, J. Yu, G. Wan, S. He, Y. Luo, Investigation of the role of surface lattice oxygen and bulk lattice oxygen migration of cerium-based oxygen carriers: XPS and designed H<sub>2</sub>-TPR characterization. *Appl. Catal., B* 218 (2017), pp. 249–259. doi: 10.1016/j.apcatb.2017.06.053.
- [132] J.-X. Yao, D. Bao, Q. Zhang, M.-M. Shi, Y. Wang, R. Gao, J.-M. Yan, Q. Jiang, Tailoring Oxygen Vacancies of BiVO<sub>4</sub> toward Highly Efficient Noble-Metal-Free Electrocatalyst for Artificial N<sub>2</sub> Fixation under Ambient Conditions. *Small Methods* 3.6 (2019), p. 1800333. doi: 10.1002/smt.201800333.
- [133] H. Idriss, On the wrong assignment of the XPS O1s signal at 531–532 eV attributed to oxygen vacancies in photo- and electro-catalysts for water splitting and other materials applications. *Surf. Sci.* 712 (2021), p. 121894. doi: 10.1016/j.susc.2021.121894.

- [134] T. J. Jacobsson, S. Viarbitskaya, E. Mukhtar, T. Edvinsson, A size dependent discontinuous decay rate for the exciton emission in ZnO quantum dots. *Phys. Chem. Chem. Phys.* 16 (27 2014), pp. 13849–13857. DOI: 10.1039/C4CP00254G.
- [135] T. Edvinsson, Optical quantum confinement and photocatalytic properties in two-, one- and zero-dimensional nanostructures. *R. Soc. Open Sci.* 5 (2018), p. 180387. DOI: 10.1098/rsos.180387.
- [136] N. Mott, E. Davis, *Electronic Processes in Non-Crystalline Materials*. Oxford Classic Texts in the Physical Sciences. OUP Oxford, 2012.
- [137] A. Dejneka, I. Aulika, M. V. Makarova, Z. Hubicka, A. Churpita, D. Chvostova, L. Jastrabik, V. A. Trepakov, Optical Spectra and Direct Optical Transitions in Amorphous and Crystalline ZnO Thin Films and Powders. *Journal of The Electrochemical Society* 157.2 (2009), G67. DOI: 10.1149/1.3267882.
- [138] J. Cho, M.-J. Lee, W.-S. Chae, Time-Resolved Photoluminescence Properties of ZnO Thin Films Evaporated by Atomic Layer Deposition. *J. Nanosci. Nanotechnol.* 15.11 (2015), pp. 8542–8546. DOI: 10.1166/jnn.2015.11463.
- [139] A. Falamas, I. Marica, A. Popa, D. Toloman, S. Pruneanu, F. Pogacean, F. Nekvapil, T. D. Silipas, M. Stefan, Size-dependent spectroscopic insight into the steady-state and time-resolved optical properties of ZnO photocatalysts. *Materials Science in Semiconductor Processing* 145 (2022), p. 106644. DOI: 10.1016/j.mssp.2022.106644.
- [140] A. Omerzu, R. Peter, D. Jardas, I. Turel, K. Salamon, M. Podlogar, D. Vengust, I. Jelovica Badovinac, I. Kavre Piltaver, M. Petravic, Large enhancement of photocatalytic activity in ZnO thin films grown by plasma-enhanced atomic layer deposition. *Surf. Interfaces* 23 (2021), p. 100984. DOI: 10.1016/j.surf.2021.100984.
- [141] L. S. Dake, D. R. Baer, J. M. Zachara, Auger parameter measurements of zinc compounds relevant to zinc transport in the environment. *Surf. Interface Anal.* 14.1-2 (1989), pp. 71–75. DOI: 10.1002/sia.740140115.

- [142] S. Afzal, L. Chen, L. Jin, K. Pan, Y. Wei, M. Ahmad, Q. U. Hassan, M. Zhang, G. A. Ashraf, L. Liu, LaCoO<sub>3</sub>/SBA-15 as a high surface area catalyst to activate peroxymono-sulfate for degrading atrazine in water. *Environmental Pollution* 349 (2024), p. 123885. DOI: <https://doi.org/10.1016/j.envpol.2024.123885>.
- [143] C. Zhou, C. Lai, D. Huang, G. Zeng, C. Zhang, M. Cheng, L. Hu, J. Wan, W. Xiong, M. Wen, X. Wen, L. Qin, Highly porous carbon nitride by supramolecular preassembly of monomers for photocatalytic removal of sulfamethazine under visible light driven. *Applied Catalysis B: Environmental* 220 (2018), pp. 202–210. DOI: <https://doi.org/10.1016/j.apcatb.2017.08.055>.
- [144] A. Trenczek-Zajac, M. Synowiec, K. Zakrzewska, K. Zazakowny, K. Kowalski, A. Dziedzic, M. Radecka, Scavenger-Supported Photocatalytic Evidence of an Extended Type I Electronic Structure of the TiO<sub>2</sub>@Fe<sub>2</sub>O<sub>3</sub> Interface. *ACS Applied Materials & Interfaces* 14.33 (2022), pp. 38255–38269. DOI: 10.1021/acsami.2c06404.
- [145] Z. Garazhian, A. Farrokhi, A. Rezaeifard, M. Jafarpour, R. Khani, The enhanced visible-light-induced photocatalytic activities of bimetallic Mn–Fe MOFs for the highly efficient reductive removal of Cr(vi). *RSC Adv.* 11 (34 2021), pp. 21127–21136. DOI: 10.1039/D1RA01986D.
- [146] M. Kocijan, L. Ćurković, I. Bdikin, G. Otero-Irurueta, M. J. Hortigüela, G. Gonçalves, T. Radošević, D. Vengust, M. Podlogar, Immobilised rGO/TiO<sub>2</sub> Nanocomposite for Multi-Cycle Removal of Methylene Blue Dye from an Aqueous Medium. *Applied Sciences* 12.1 (2022). DOI: 10.3390/app12010385.
- [147] T. H. Jeon, D. Monllor-Satoca, G.-h. Moon, W. Kim, H.-i. Kim, D. W. Bahnemann, H. Park, W. Choi, Ag(I) ions working as a hole-transfer mediator in photoelectrocatalytic water oxidation on WO<sub>3</sub> film. *Nature Communications* 11.1 (2020), p. 967. DOI: 10.1038/s41467-020-14775-2.